Scalable strategies for tumour targeting of magnetic carriers and seeds

Matin Mohseni

Submitted for the degree of
Doctor of Philosophy in Biomedical Engineering
October 2019

Centre for Advanced Biomedical Imaging (CABI), Division of Medicine
University College London

Declaration

I, Matin Mohseni, confirm that the work presented in this thesis is my own work, except where stated otherwise in the text. This work is based on research which has been conducted by me, during the time period from October 2015 to August 2019 at the University College London.

Abstract

With the evolving landscape of medical oncology, focus has shifted away from nonspecific cytotoxic treatment strategies toward therapeutic paradigms more characteristic of targeted therapies. These therapies rely on delivery vehicles such as nano-carriers or micro robotic devices to boosts the concentration of therapeutics in a specific targeted site inside the body. The use of externally applied magnetic field is suggested to be a predominant approach for remote localisation of magnetically responsive carriers and devices to the target region that could not be otherwise reached. However, the fast decline of the magnetic fields and gradients with increasing distances from the source is posing a major challenge for its clinical application.

The aim of this thesis was to investigate potential magnetic delivery strategies which can circumvent some of the typical limitations of this technique. Two different approaches were explored to this end. The first approach was to characterise the ability of a conventional permanent magnet on targeting individual nano-carriers and develop novel magnetic designs which improve the targeting efficiency. The second approach was evaluating the feasibility of a magnetic resonance imaging system to move a millimetre-sized magnetic particle within the body.

Phantom and *in vivo* magnetic targeting experiments illustrated the significant increase in effective targeting depth when our novel magnetic design was used for targeting nano-carriers compared with conventional magnets. In the later part of the thesis, the proof of concept and characterisation experiments showed that a 3 mm magnetic particle can be moved in *ex vivo* brain tissue using a magnetic resonance imaging system using clinically relevant gradient strengths. The magnetic systems introduced in this thesis provide the potential to target nano-carriers and millimetre-sized thermoseeds to tumours located at deep regions of human body through vasculature and soft tissue respectively.

Impact statement

Modern medicine aspires to target therapies directly to disease or injury while minimising damaging effects to normal tissue. Delivering a therapy with precision, while at the same time reducing the off target burden, is key for improving patient outcome and reducing the economic impact of these unwanted effects. In the US alone, the cost of off target drug effects exceeded $177 billion in 2000. Targeted therapies and focal ablation techniques, aim to address this need, and often take a personalised approach. Yet conventional cancer therapies still suffer from a lack of precision and implanted devices such as brachytherapy seed or untethered deceives lack control in situ.

The work proposed in this thesis has the potential to enable magnetic targeting therapies to address this need and move towards widespread clinical application. This technology has important application in brain cancer therapy and addresses several of the current barriers to clinical translation in minimally invasive magnetic therapies. The ability to accurately target, control and disrupt cells at the site of injury or disease in a non-invasive fashion will limit off target effects, which is key to the success of any novel therapeutic intervention. By solving this problem using the properties of magnetic nanoparticles and their responses to applied fields will provide important tools needed to realize the full potential of magnetic targeting therapy.

Furthermore, the novel technologies outlined in this proposal allow a magnetic particle to be navigated through the brain or liver and treat localised regions of cells using a magnetic resonance imaging system. The successful clinical translation of the novel devices and MR sequences would form a valuable tool for academic centres focused on therapy and imaging biomarker development, such as the new McMillian Cancer Hospital at UCL.

Minimally invasive therapies have the potential to treat a myriad of conditions that affect our wellbeing including diseases such as cancer, as well as diseases and tissue degeneration associated with an aging population, such as neurodegenerative diseases, heart and respiratory ailments. Our commercial partners bring product development expertise to the current study, as well as the skills required to take magnetic targeting into hospitals and clinics in the future. Existing collaborations include *Chemicell* and *Micromod*, magnetic particle manufacturers, which specialise in biofunctionalisation for diagnostics. *Bayer-Schering Pharma* is a major pharma corporation and the manufacturer of *Resovist,* whose contrast media division sees magnetic targeting as opening up new product streams. *Philips and Tesla Engineering* are international medical imaging/devices companies and a potential manufacturing and/or distribution partner.

Reaching out we will use our public partners which include patient advocacy, engagement forums and support groups. These include the *Cheltenham Science Festival, Cancer Research UK, The British Lung Foundation,* and engaged end-user groups within our hospitals. Industry-academic partnerships (Philips, Tesla Engineering) in minimally invasive work will increase in the coming years, and public understanding and support will be needed to maximise chances of success. Therefore, we will prioritise approaches to improve the public perception of the value of novel technologies such as magnetic nanoparticles in drug discovery and development.

Acknowledgements

I am indebted to my primary supervisor Professor Mark Lythgoe for his extensive help, support and supervision throughout this project, and my secondary supervisor Professor Quentin Pankhurst for the insightful conversations.

This thesis would not have been possible without the help of Dr John Connell who showed me the essentials of magnetic targeting as well as instructing me on acquiring images using magnetic resonance imaging and Dr Stephen Patrick who showed me the essentials of cell culture and wet lab skills.

I would also like to thank Dr May Thin for her assistance for intravenous injections, Henrik Høyer from Giamag technologies who helped me with the design of scalable magnets and Steve Bates and Craig Woods from Tesla engineering and Dr Bernard Siow for their help on setting up the magnetic targeting gradient coil.

A huge thank you must go towards my colleagues in magnetic targeting group Chris Payne and Rebecca Baker for their contribution and companionship. I would also like to thank my other colleagues; Yichao Yu, Tammy Kalber, and all other CABI members specifically Dr Jack Wells for his support on MRI.

A special thank you goes to Payam Nahavandi for his unconditional companionship and the Nahavandi family for their support throughout writing this thesis.

Finally, my eternal love and gratitude goes to my wonderful parents Alireza Mohseni and Marzyeh Mohammadi for their truly selfless and unconditional support. Without them, my achievements would amount to nothing.

Conference abstracts arising from this thesis

Mohseni M et al. In-vivo targeting and imaging of super-paramagnetic iron-oxide particles to subcutaneous tumour models**.** 11th International Conference on the Scientific and Clinical Applications of Magnetic Carriers. June 2016. Vancouver, Canada

Mohseni M et al. Magnetic targeting and imaging of magnetic nanoparticles to subcutaneous tumours. The post-graduate *British Chapter of the ISMRM. March 2017. King College London, UK*

Mohseni M et al. In-vivo targeting and imaging of super-paramagnetic iron-oxide particles to subcutaneous tumour models. The ISMRM 25th Annual Meeting & Exhibition Hawai'i Convention Center. April 2017. Honolulu, USA

Mohseni M et al. Magnetic targeting and imaging of magnetic nanoparticles to subcutaneous tumours. 23rd Annual Scientific Meeting of the *British Chapter* of the *ISMRM. September 2017. Liverpool, UK*

Mohseni M et al. Magnetic targeting and imaging of super-paramagnetic iron-oxide nanoparticles to subcutaneous tumour models. The ISMRM 26th Annual Meeting & Exhibition Paris. June 2018. Paris, France

Mohseni M et al. Magnetic targeting and imaging of super-paramagnetic iron-oxide nanoparticles to subcutaneous tumour models. MagSoc conference MRI and Magnetic Particles for MRI Diagnostics. February 2019. Oxford University. UK

Mohseni M et al. Magnetic targeting and imaging of super-paramagnetic iron-oxide nanoparticles to subcutaneous tumour models. BioMedEng 2019 Conference. September 2019. Imperial College London. UK

Mohseni M et al. Rethinking Surgery with MINIMA: A minimally invasive, image-guided ablation technique using MRI. Cancer Research UK-AACR conference on engineering and physical sciences in oncology. October 2019. London, UK

Papers under review:

Matin. J. Mohseni [a] , John. J. Connell [a], Christopher. Payne [a], P. Stephen. Patrick [a], Rebecca. Baker [a], Yichao Yu [a], Bernard. Siow [a], Tammy. L. Kalber [a], Quentin. A. Pankhurst [b], Mark. F. Lythgoe[a#] . ''Scalable magnet geometries enhance tumour targeting of magnetic nano-carriers''

Table of contents

List of figures

List of tables

1. Introduction to magnetically targeted therapies

The goal of novel targeted interventions is to deliver sufficient therapy to specific pathological tissue while leaving healthy cells unaffected. This interventional strategy would be of most relevance in cancer, where common treatment methods suffer from adverse off-target effects. To effectively treat a tumour, most cancer interventions involve a combination of treatments, such as surgery with chemotherapy and/or radiation therapy. The choice of therapy depends upon the location and grade of the tumour and the stage of the disease, as well as the general state of the patient. While the seemingly endless advancement in technologies in recent years has allowed increasingly more precise and less invasive procedures, complete removal of the cancer without damage to the rest of the body remains one of the main challenges in cancer therapy. Using magnetic particles ranging from nm-mm, magnetically targeted strategies aim to deliver a therapeutic moiety to tumour cells[1] or to induce hyperthermia, and as such, selective cell death within tissue[2]. Although such interventions have shown promising results in cancer treatments, their applications are limited to superficial regions of the human body mainly due to the fast decline of magnetic force with increasing distance from their source. Additionally, imaging the delivery and retention of therapeutic particles at the site of interest, is crucial in the development of safe and effective therapies. As such, imaging is an important factor to consider when designing and using novel experimental techniques. This thesis looks to improve on currently available magnetically targeted therapies in cancer by developing novel magnetic designs (chapters 3 and 4) and image guided targeting strategies (chapters 5 and 6).

This introduction chapter broadly covers two areas: Firstly, relevant applications of magnetic particles including magnetic actuation, Magnetic Resonance Imaging (MRI) contrast enhancement, and magnetic hyperthermia are presented. Secondly, as the main aim of this thesis is to develop novel techniques for magnetic actuation of particles, the next part of this chapter will focus on magnetic systems used to deliver therapies. The magnetic devices used in the literature will be introduced and the clinical impact of each system will be discussed.

1.1 Applications of magnetic particles

Owing to their magnetic properties, magnetic particles can be utilised in a wide range of medical applications. This section will provide an overview of some of the most widely used applications, which can broadly be divided into three main categories. (i) Magnetic drug/cell targeting which refers to labelling drugs or therapeutic cells with magnetic particles and focusing them in the pathological tissue using external magnetic fields. (ii) Imaging of magnetic particles which refers to the ability to detect superparamagnetic iron oxide particles using MRI due to their T_2 and T_2^* contrast enhancement. Finally, (iii) magnetic hyperthermia, which refers to the use of magnetic particles and radio-frequency waves to induce cell death through elevated local temperature.

1.1.1 Magnetic targeting

1.1.1.1 Magnetic drug targeting

Drug development has been one of the most successful areas of research in the 20th century due to the increased understanding of human diseases. Unfortunately, most drugs cause unwanted side effects by acting on non-disease healthy cells. In particular, anti-cancer drugs which were developed to kill fast growing cancer cells also affect other fast-growing cells such as epithelia and hair follicle cells. To address this issue, various targeting strategies have been proposed to increase the concentration of the anti-cancer drug in the tumour, and consequently reduce the concentration delivered to the rest of the body. The simplest strategy is passive targeting, which is the auto accumulation of a drug carrier agent in the tumour area by the enhanced permeability and retention effect (EPR)[3] - a process by which nano-sized drugs leak preferentially into tumour tissue through permeable tumour vessels and are then retained in the tumour bed due to reduced lymphatic drainage. However, to enhance the effectiveness of passive accumulation, active targeting protocols such as biochemical targeting have been developed. In biochemical active targeting, a versatile target agent such as small molecules, peptides or antibodies are used against specific surface markers in the targeted tumour cells[4]. Nevertheless, such targeting method is limited only to certain types of cancer cells that express specific receptors on their surface, and hence not applicable to all cancer cells[4].

Another active targeting strategy is Magnetic Drug Targeting (MDT), which refers to the use of a magnetic field to direct or capture magnetic drug carriers at the tumour area through intravenous, intra-arterial or direct injection. Such targeting strategy has shown to be a promising method to increase the delivery of drugs to specific regions of anatomy whilst reducing systemic dosing and off-target side effects[5]. The first applications of magnetically targeted drugs were investigated in the 1970s with the suggestion of using magnetic particle-loaded erythrocytes[6] or magnetic microspheres[7,8]. These studies demonstrated that a significantly lower (up to 100-fold) systemic dose of the magnetically targeted drug was needed to achieve the same concentration as a non-targeted drug in the targeted tissue.

One of the most important parameters of magnetic drug targeting is the magnetic carrier. Since the first applications in the 1970s, a variety of magnetic nanoparticle and microparticle carriers have been developed to deliver drugs to specific target regions within the body. Magnetic carries are typically made in two types of structures- single magnetic carrier (SMC) and capsule magnetic carrier (CMC)[9]. SMCs contain one magnetic nanoparticle (usually magnetite Fe_3O_4 or maghemite $\gamma - Fe_2O_3$, see section 1.1.1.2) in each individual carrier, which is typically coated with a biocompatible polymer to improve the *in vivo* stability and support conjugation of the anti-tumour drug. In CMCs on the other hand, multiple magnetic nanoparticles and anti-tumour drugs are encapsulated by hydrophilic or amphiphilic polymers. Typically, SMCs have a smaller hydrodynamic size of 10-100 nm, whereas CMCs have larger sizes around 150-400 nm.

All magnetic carriers are inorganic compounds which are easily scavenged from the body circulation either by the renal system or Reticuloendothelial System (RES) depending on their size. Particles smaller than 10 nm will be excreted through the kidneys and bigger ones (>100 nm) will be detected from the blood and transferred to the liver and spleen by the RES system[10]. In addition to size, clearance of magnetic carriers is also dependent on the surface composition and charge of the polymeric coating[10]. Even for carefully engineered nanoparticles, about half of the particle dosage (50% of the Chemicell particles used in the clinical trial[11]) is caught and cleared to the liver, spleen, and kidneys within minutes[12]. The remaining particles are taken out of circulation more slowly, over several hours (about 4 h for 30% more) to days, depending on their size and properties. In recent years, surface modified SMC[12] and CMC formulations[5] have been developed which improve the circulation half-life of carriers from a minute to hour time scale.

The core function of the magnetic carrier is delivery of the therapeutic agent to the target tissue. Thus, conjugation and release mechanism of the drug from the carrier is a topic of considerable importance. There are two main methods for conjugation - covalent and non-covalent conjugation. Covalent conjugation uses a chemical bond to attach the agent to the carrier. The most common covalent conjugations include amide linkage[13], thermo-degradable bond[14], pH-degradable bond[15] and enzymatic and redox cleavage bonds[16,17]. On the contrary, non-covalent conjugation does not need any chemical bonds and is typically achieved via processes such as hydrophobic interaction[18], electrostatic interaction[19], coordination chemistry[20] and encapsulation[21]. Although covalent conjugation involves a more sophisticated process than the non-covalent protocols, it has the advantage of having the control over the release of the drug in a specific target region by choosing an appropriate chemical bond between the drug and carrier[9]. In a vast majority of CMC investigations, a non-covalent conjugation such as encapsulation has been used whereas both non-covalent and covalent conjugations have been exploited in the SMC studies.

The effectiveness of magnetic drug targeting is dependent on two major driving factors: (i) physical parameters such as the magnetic field strength and gradient as well as the size and magnetic properties of the particle and (ii) hydrodynamic parameters such as blood flow, administration route, circulation time, carrier concentration and reversibility of the drug/carrier conjugation. While the success of magnetic drug targeting considerably relies on the interplay between the physical and hydrodynamic components, pathophysiological alteration of solid tumours can further enhance the effectiveness of such therapy. For example, the physiological differences in blood flow velocity[22] and vascular permeability[10] between the tumour and normal tissue provides a selective mechanism for magnetic capture of drug-loaded carriers at the tumour site. Among carrier types, nano-scaled colloidal carriers offer an extra advantage, which is attributed to the EPR effect[10,23,3], where particles even as large as 200-300 nm, are able to extravasate into tumour interstitial region through the hyperpermeable vasculature of most solid tumours.

Since the first investigation of magnetic targeting of cytotoxic drugs to a sarcoma tumour implanted in a rat tail[24], successful drug delivery, tumour remission and reduced systemic toxicity have been reported in different animal models including rabbits[25], rats[26,27], mice[28,5] and larger animals such as pigs[29,30]. One potential risk of such techniques is embolisation of the blood vessels as the particles accumulate within the bloodstream, blocking blood flow[31]. However, with recent advancement of particle development, particles with small hydrodynamic size (<200 nm), super-paramagnetic cores (see section 2.2.1) and appropriate coatings (or encapsulation) have been designed to minimize such risks[31,5].

To date, there have only been two clinical trials of magnetic drug targeting. The first of the two clinical assessments, involved 14 patients on which a single permanent magnet was used to concentrate various intravenous doses of 100 nm magnetic particles bound to epirubicin (a chemotherapy drug) to inoperable but shallow (within 5 mm below skin) head, neck, and breast tumours. A magnetic field of 0.5-0.8 T was applied to tumours for 60-120 min[11] (Figure 1.1). In all but five of the patients the presence of the particles was detected with MRI and in four patients a decreased tumour size was observed. All patients tolerated the therapy well with reduced systemic toxicity and plasma concentration of the drug compared to epirubicin dosing of the control group. While these investigations showed the safety and effectiveness of this method in humans, a highly variable degree of particle accumulation was observed in tumours between different patients. Thus, the authors concluded that magnetic drug targeting must be improved in terms of the hydrodynamic properties of magnetic particles as well as the strength and depth penetration of the magnetic force; tumours where only located up to a 5 mm distance below the skin[11].

Figure 1.1 - The first human trials in magnetic drug targeting. The patient shown had an advanced and inoperable face tumour. A ferrofluid of magnetic nanoparticles coated with a chemotherapeutic agent was focused to the tumour by a single externally held 0.8 T rectangular permanent magnet.

In the more recent investigation, 0.5-5 µm particles bound to doxorubicin were directly injected into the hepatic artery of four patients with hepatocellular carcinoma (a type of liver cancer) with application of an external magnetic field directly on the liver. Angiographic techniques and MRI were used to monitor the delivery of the magnetic particles to tumour locations during an intraoperative procedure. Such experimental design allowed the investigators to achieve a total targeting coverage of up to 91% percent of the tumour volume by repositioning the catheter. Although the results of the second clinical investigation showed more effectiveness in magnetic drug delivery and tumour response compared with the first trial, the direct injection method used in this study would not be a feasible solution for every tumour type.

Despite these promising preclinical and clinical investigations, as mentioned previously, there are several problems associated with magnetic drug targeting in terms of the hydrodynamic and physical parameters. Among these there are two main issues - (i) short plasma half-life and toxic responses of some magnetic carriers[32] which was reported to be a limitation in the first clinical trial[11] and (ii) difficulty in increasing the distance between the magnetic source and the target site due to the rapid reduction in the magnetic field strength and gradient of magnetic sources. Although the hydrodynamic aspect of magnetic carriers is an active area of research, it is outside the scope of this thesis. The physical limitation however, will be extensively investigated in chapters 3 and 4 by applying a variety of magnetic force topologies on an SMC model of magnetic nanoparticles. The next section provides an introduction to magnetic cell targeting, which aims to deliver magnetically labelled therapeutic cells to tumours or regions of vascular injury.

1.1.1.2 Magnetic cell targeting

During the past few decades, a number of different cell types have been shown to have therapeutic effects for a wide range of pathologies[33]. Additionally, research efforts are increasingly directed towards the development of targeted therapeutics[34]. One potential possibility is the use of magnetically targeted strategies to spatially localise such therapeutic cells, as magnetic fields can penetrate the human body without causing any damage to healthy tissue.

The aim of magnetic cell delivery is to guide therapeutic cells to a specific region of the human body. In order to be able to guide cells with a magnetic field, it is necessary to label cells with a magnetically responsive entity. For example, Riegler et al have shown promising results in magnetic tagging of cells for a vascular injury model[35] (see section 1.2.1). The interaction of the magnetically labelled cells and the magnetic field gradient can then be used to deliver these cells to the region of interest. In addition to magnetic responsiveness, non-invasive imaging can also be used to track the cells and confirm their delivery and integration into pathological target tissues.

Iron-oxide nanoparticle have been favoured in a vast majority of research applications[35,36] due to their biodegradability[37,38], cell tolerability and ability of the human body to degrade and integrate them into the body iron pool[37,38,37]. Additionally, Superparamagnetic Iron-Oxide Nanoparticles (SPIONs) can act as a magnetic resonance imaging (MRI) contrast agent[34,40,41] (see section 1.1.2), making them a suitable theranostic agent for both targeting and tracking of cells. Clinical studies with SPION labelled cells show that these cells are well tolerated without unwanted side effects[42,43].

In addition to the magnetic properties of the magnetic entity, efficient cell delivery also depends on the hydrodynamic size of the magnetic particle. To achieve appropriate cell labelling, small hydrodynamic diameters are favourable as they allow a higher iron concentration within the cells[44,45]. Particles smaller than 200 nm diameter will be internalised into the cells by a process called pinocytosis[46] whereas bigger particles have to be actively internalised via another process called endocytosis[46]. As indicated previously, the main aim of magnetic cell delivery is to deliver cells that are biologically active. It is hence important that the labelling process does not affect the therapeutic potential of cells as well as their growth, differentiation and migration. To address such requirement, Riegler et al have gathered experimental evidence on cell viability after internalisation of magnetic nanoparticles[35].

Non-invasive imaging allows researchers to identify the location of the cells, investigate whether they are migrating to other places and determine the best delivery route for them. There has been a wealth of literature on non-invasive *in vivo* tracking of therapeutic cells. Potential imaging modalities suitable for this purpose include, MRI[47,48,42,43,49,50], SPECT[51,52,53,54], and bioluminescence[55,56,57]. MRI is a popular modality for cell tracking not only due to presence of iron-oxide particles in cells but also for the high soft tissue contrast that it generates. Section 1.1.2.1 provides a more detailed explanation of the negative contrast created by iron-oxide particles in the MR images. On the other hand, one limitation of MRI is the fact that it cannot distinguish between live and dead cells or between differentiated or undifferentiated states. To overcome these limitations, other imaging modalities such as SPECT and PET are under investigations[54,58,59], which can be combined with MRI to gain more information about the *in vivo* viability of the cells.

Magnetic cell delivery strategies have demonstrated their potential in preclinical[36,60–62] and clinical[42,43,62] investigations. However, the safety profile has to be addressed for each individual cell type and cell line separately. In addition, as stated in the introduction, one of the biggest problems with magnetic drug/cell targeting is the fast decline of magnetic force with increasing distance from their source, which has hampered clinical translation of these techniques. As stated previously, this problem will be addressed in detail in chapters 3 and 4 of this thesis. In chapter 3, I present my investigations on magnetic targeting of SMC nanoparticles using a single disk magnet and in chapter 4 I introduce novel magnet designs, which aim to improve the distance limitation of permanent magnets. The next section will focus on the ability of magnetic nanoparticles to produce contrast in MRI.

1.1.2 Imaging

Monitoring the delivery and retention of therapeutic moieties at the target region is of primary importance for magnetic targeting. Longitudinal assessment of the retention of delivered therapeutics can influence treatment decisions regarding repeated administration. In addition, remote manipulation of particles using image guided methods can provide feedback control on particle location during delivery. The ability to image the target region non-invasively is therefore an important factor to consider when designing and using magnetic targeting strategies. The most widely available technique for imaging magnetic particles is MRI due to the contrast produced by these particles in MR images. This section will provide a brief overview on synthesis and physical properties of magnetic nanoparticles and how these particles can be used as contrast agents for MRI.

1.1.2.1 Magnetic nanoparticles as MRI contrast agents

T_2 contrast agents (or negative contrast agents) decrease the MR signal intensity of the regions they are delivered to. Consequently, they produce hypointense signals in T_2 - and T_2 *-weighted images[63] and thus the affected regions appear darker. This phenomenon is the result of induced dephasing of the proton magnetic moments when water molecules diffuse through the large heterogeneous magnetic field surrounding the nanoparticle, resulting in T_2 shortening. T_2 contrast agents are also called susceptibility agents because of their effect on the magnetic field. T_2 shortening is a remote effect, whereas the T_1 shortening process requires a close physical interaction between the water molecules and T_1 contrast agents.

Iron oxide nanoparticles have been used as T_2 contrast agents for more than 25 years[64]. These iron oxides can be ferromagnetic or superparamagnetic, depending on their size. Magnetite (Fe_3O_4) and maghemite (γ-Fe_2O_3) are the two types of iron-oxide particles which can be synthesized through the co-precipitation of Fe^{2+} and Fe^{3+} aqueous salt solutions by addition of a base[65]. The critical upper size limit for the observation of superparamagnetism is approximately 25 nm for magnetite and 30 nm for maghemite[66]. The two compounds fulfil the prerequisites for contrast agents, which include 1) chemical stability under physiological conditions, 2) low toxicity, and 3) sufficiently high magnetic moments[64].

Most magnetic nanoparticles are comprised of an iron-oxide core and a chemically synthesized surface coating, which are dispersed into suitable solvents, forming homogenous suspensions called ferrofluids[67,68]. The size of the magnetic nanoparticles is one of the most important properties that can be utilised to optimise major properties such as magnetism and surface area. Many researchers have explored different techniques to create controlled-sized synthesis of nanoparticles[69,70]. The influential parameters to control size, shape and composition were shown to be the type of salts used (e.g. chlorides, sulphates, nitrates, perchlorates, etc.), Fe^{2+} and Fe^{3+} ratio, pH and ionic strength of the media for iron-oxide based nanoparticles[71,72] . As the in vivo distribution of magnetic nanoparticles is influenced by their size, these particles can be classified as follows: 1) Ultra-small Superparamagnetic Iron Oxide Nanoparticles (USPIONs) with diameter (d) less than 50 nm, 2) Superparamagnetic iron oxide nanoparticles (SPIONs) hundreds of nanometers in size, and 3) Micron-sized Particles of Iron Oxide (MPIO) with a diameter higher than 1 µm[64] . The small overall size of the USPIONs and SPIONs allows intravenous injected of these particles, however, the larger MPIO particles are administrated orally which, limits their utilisation on exploration of the gastrointestinal tract.

In addition to size, the surface composition and charge play an important role in maintaining the colloidal stability of nanoparticles[73]. Iron oxide cores have hydrophobic surfaces with a large surface area to volume ratio. Due to these hydrophobic interactions, particles agglomerate and form large clusters, which leads to an increased aggregate size. Once a large cluster is formed, it exhibits a strong magnetic dipole-dipole attraction, resulting in a ferromagnetic behaviour[74]. When two large particle clusters come into close proximity with one another, both cluster get further magnetised and attract each other creating a larger aggregate size[75]. In the presence of surface coating, hydrophobic interactions are reduced and as a result stability, biocompatibility and target-specificity of iron-oxide nanoparticles are improved[76]. This creates significantly less particle clusters, although aggregation is not completely avoidable especially at high magnetic field strengths. Considering the surface chemistry, several materials and functionalisation have been used in the literature. These include polymeric coating, liposomes, micelles utilisation, and core-shell structures[74].

Previously, synthesis of magnetic nanoparticles was an important step in all studies dedicated to improving their properties and testing their practical applicability [74]. However, a lot of development is required to ensure the safety, effectiveness and therapeutic efficacy of magnetic nanoparticles[33]. EMEA and FDA have approved several SPION particles for clinical use as MRI contrast agents using oral or intravenous administration. However, at present, most of the SPION formulations that were approved for intravenous administration have been removed from the market[64]. Only Gastromark® (AMAG Pharmaceuticals, Waltham, MA, USA; ferumoxsil, silicone-coated SPIONs), which is the SPION for oral administration, is currently available on the market for gastrointestinal bowel marking. Dextran and carboxydextran formulations are among most widely applied coatings for the SPIONs that were approved by the FDA[64].

Utilisation of iron-oxide nanoparticles as MRI contrast agents has been a considerably active area of research in the past decades[64]. This technique has led to various exciting investigations in cancer theranostics[77,78], and cell tracking in regenerative medicine[79]. In addition to providing contrast in MRI, iron-oxide nanoparticle have also been used as multi-modal imaging probes due to their intrinsic material properties that allow for tunable pharmacokinetics and surface modification[78] . Previous investigations have developed iron-oxide based imaging probes for dual imaging modalities such as MRI/OPT[80], MRI/CT[81], MRI/PET[82] and MRI/SPECT[83]. The use of iron-oxide nanoparticles as the base platform for multimodal imaging is a recent technology that provides an attractive solution to limitations of a single imaging modality and hence contributes to the advancement of cancer theranostics.

The ferrofluid used in the studies reported in this thesis is a commercially available solution (FluidMAG produced by Chemcell Germany), which was previously used in the phase 1 clinical magnetic drug targeting trial (see section 1.1.1.1). As the core of these particles is made of SPIONs, they can be observed in T_2 and T_2^* weighted MRI images, which facilitates monitoring of *in vivo* delivery of these particles in regions of interest within the body. In addition to drug delivery and imaging, these particles have also previously been used for multimodal cell tracking[84], magnetic cell delivery[36] and hyperthermia[85] studies. As such, these properties makes these particles an excellent option for investigation of magnetic tumour targeting (see section 2.2.1). For these reasons we chose to investigate magnetic targeting of these particles in order to test the efficacy of our magnetic designs discussed in chapters 3 and 4 of this thesis. The next section will focus on magnetic hyperthermia which provides the basis for chapters 5 and 6.

1.1.3 Magnetic hyperthermia

In addition to drug delivery and imaging, magnetic particles have also been combined with alternating external magnetic fields to deliver mild elevation of temperature to produce selective cell death[86] or high temperature rise to ablate a selected region within tissue[2]. In chapter 5 of this thesis we introduce an image-guided interstitial navigation method using millimetre-sized magnetic particles (thermoseeds) and MRI. To provide insight to magnetic hyperthermia, an introduction of this method is provided in this section, which is divided into two main parts: (i) magnetic hyperthermia which uses magnetic nano/microparticles and an alternating magnetic field to produce selective cell death and (ii) magnetic ablation using thermoseeds which uses millimetre-sized particles and alternating magnetic fields to ablate tumours.

1.1.3.1 Magnetic hyperthermia using nanoparticles

Magnetic hyperthermia refers to the use of magnetic particles in combination with alternating magnetic fields to produce localised heat formation. The low heat resistance of tumour cells compared to healthy tissue[34] provides the basis for selective killing when the magnetic particles are heated in a cancerous region. Magnetic hyperthermia aims to achieve temperatures of >42°C to selectively damage cancer cells and induce apoptosis. In addition to hyperthermia, an alternating magnetic field can also be used to induce the controlled release of a drug from the magnetic carrier in magnetic drug targeting applications[87].

Heat generation in magnetic hyperthermia is produced by means of three main mechanisms. (i) hysteresis loss, (ii) Neel relaxation and (iii) Brownian relaxation (Fig. 1.2)[32,88]. Other magnetically induced mechanisms such as eddy current heating and ferromagnetic resonance effects are negligible due to the small size of the particles and frequency ranges used for magnetic hyperthermia. When a magnetic moment is exposed to a magnetic field, which it is not aligned with, it will reduce its magnetostatic energy by rotating to align with the field. This loss of magnetostatic energy (the magnetic potential energy generated due to the presence of a magnetic field) produces heat in a process called hysteresis loss. Heat generation in hysteresis loss is dependent on the particle size and magnetic properties, as well as the frequency and amplitude of the alternating magnetic field. When the magnetic field is removed, the magnetisation relaxes back to zero due to ambient thermal energy of the environment. This relaxation can correspond either to the physical rotation of the particles within the suspension media, or the rotation of the atomic magnetic moment within each particle (Fig. 1.2). Rotation of the particles is referred to as Brownian relaxation, while rotation of the moment within each particle is known as Neel relaxation[32]. Each of these processes is characterized by a relaxation time. The Brownian relaxation time depends on the hydrodynamic properties such as the viscosity of the media; while Neel relaxation is determined by the magnetic anisotropy energy of the particles relative to the thermal energy.

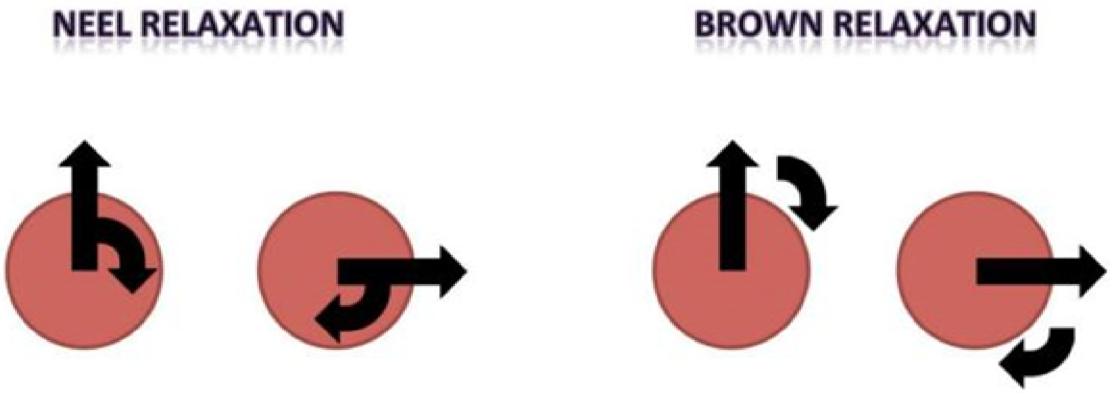

Figure 1.2 – Magnetic relaxation of nanoparticles. Neel (left) and Brownian relaxation (right) (adapted from[89])

The first clinical demonstration of hyperthermia was carried out in the 1950s in gastrointestinal tract lymph node metastases[89], in which magnetic particles were injected into the lymphatic system and heated using a radiofrequency field. Over the past few decades, the field of magnetic particle hyperthermia has been revolutionised by the use of SPIONs suspended in water or a hydrocarbon fluid (ferrofluid)[90,91,85]. Since the first demonstration, there have been a number of recent clinical studies (glioblastoma[92] and prostate tumours[93]) that utilised SPIONs with alternating current magnetic fields to induce cell death. These clinical trials have relied on direct injection of particles into the tumour in order to achieve sufficient concentration of particles and consequently higher temperature within the tumour; which limits this technique to easy-to-reach tumours where direct injection of particles is possible.

To provide an alternative solution, mesenchymal stem cells (MSCs) have been used as potential cell carriers to deliver SPIONS to difficult-to-reach tumours in a preclinical investigation[85]. However, the treatment results of this study were not as promising as the studies in which SPIONs[94,95] were directly injected. Additionally, some preclinical studies[96] have suggested the combination of magnetic targeting with hyperthermia as an alternative to direct injection. However, similar to the use of MSCs, the results of these studies have not been as convincing as the results of direct injection studies.

In conclusion, magnetic hyperthermia using SPIONs has shown to be an effective treatment that can enhance the outcomes of radiotherapy and chemotherapy[86]. One limitation is the inability to deliver a high enough concentration of nanoparticles to the tumour to produce the required effect[86]. There is currently an active area of research to increase delivery of SPIONs to tumours using active targeting strategies mentioned in the previous section, which involves functionalisation of SPIONs with antibodies[86,95] or using externally applied magnetic fields (chapter 3). The next section will introduce magnetic ablation techniques, which use millimetre-sized magnetic particles.

1.1.3.2 Magnetic ablation using thermoseeds

The previous section provided an overview on magnetic hyperthermia using nanoparticles and the limited heating effects due to low concentration of particles reaching the tumour. This section of the thesis will introduce an alternative method to produce temperature mediated-cell death. Rather than using SPION solutions, millimetre-sized untethered magnetic seeds could be implanted into the affected tissue. Following implantation, an alternating magnetic field (AMF) can be applied to heat the seed remotely to either cause localised cell death or induce local hyperthermia around the seed[97]. Unlike hyperthermia with nanoparticles, for which eddy currents have a negligible contribution to heating, the eddy currents generated on the themoseed surface produce a considerable enhancement in particle heating. The heating properties of the thermoseeds are affected by their size, shape, material and orientation with respect to the AMF. Any non-spherical seed needs to be aligned parallel to the AMF for optimal heating [98].

To date only very few clinical studies have used magnetic thermoseeds to treat brain[99,100] or prostate[101] tumours in combination with radiotherapy. The world's first clinical trial of magnetic ablation by thermoseeds was carried out in Japan. Kida et al[99,100]., reported the first clinical experience of interstitial hyperthermia of malignant brain tumours by ferromagnetic thermoseeds in 1990. Though the applicability of the results is still tentative, the overall response rate was an encouraging 34.8%. Two years later Stea et al. completed a phase I study of interstitial thermoradiotherapy for high-grade supratentorial gliomas[102]. Among the 28 patients, 22 were treated at the time of their initial diagnosis with a course of external beam radiotherapy followed by an interstitial implant with Ir-192. A 60-minute hyperthermia treatment was given just before and immediately after completion of brachytherapy via the same catheter. Hyperthermia was generally well tolerated. Results showed that for around 50% of the 25 patients with primary tumours, therapy was efficacious, and magnetic ablation was one of the factors closely correlated with the patient survival period.

With the inspiring results from the clinical trials for malignant brain cancer, Deger et al[101]. carried out ablation of prostate cancer by cobalt-palladium thermoseeds of 1 mm diameter and 14 mm length[103] with a median number of 30 seeds uniformly placed throughout the whole prostate. Intraprostatic temperature reached between 42 and 46 °C and no major side effects were observed. The PSA (prostate specific antigen) levels of the patients were monitored for an average period of 36 months (range 3-72 months) and the median PSA value decreased from 11.6ng/ml to 2.4 ng/ml 3 months after treatment, 1.3 ng/ml 12 months after treatment and to 0.55 ng/ml 2 years after therapy. The authors concluded that interstitial hyperthermia is feasible, well tolerated and could lead to a steep decrease of PSA values.

While interstitial implantation of thermoseeds has shown to be a safe and effective method, the need to insert multiple seeds into the tissue to ensure ablation of the whole tumour region increases the chance of ablating healthy parts of the affected tissue. In order to increase specificity of the ablation to the tumour area, the surgeon needs to have the ability to manipulate and manoeuver the seed after implantation. To provide a proof of principle for this method, biplane fluoroscopy was combined with a magnetic stereotaxic guidance to steer a millimetre-sized thermoseed through the canine brain[2] – This method was named video tumour fighter (VTF). In this technique, the seed was administrated into the brain through a burr hole into the occipital lobe and moved on a pre-determined path towards a target area in the brain using externally applied magnetic fields. Once the seed reached the target site, radiofrequency waves were applied to ablate the tissue. After tissue ablation, the seed was moved back to the insertion location, where it was removed from the brain. Although this was achieved using a several millimetre-sized NdFeB cylinder, histological analysis showed no sign of haemorrhage along the seed path, indicating the safety of magnetic manipulation of an untethered thermoseed in brain tissue.

While promising results were obtained in combination of movement, seed detection and heating experiments, such remote surgical navigation tool was never taken further in the brain, presumably due to the lack of sufficient tissue contrast from fluoroscopic or CT images, which is crucial for safe propulsion of the seed within the brain. Although the VTF project utilised pre-acquired MRI images and used fiducial markers to register these images with fluoroscopic images, the inherent registration errors between the two imaging modalities reduced the overall accuracy of the method. Instead this work has led to the formation of the company known as Stereotaxis, which uses magnetic control to guide catheters, endoscopes, and other surgical tools with magnetic tips for precision treatment of cardiac arrhythmias and other cardiovascular procedures[104].

The idea of remote magnetic propulsion of thermoseeds through tissue forms the basis of chapters 5 and 6 of this thesis. Rather than using cooled electromagnets or permanent magnets, in chapter 5 I introduce the possibility of using the MRI system to image and propel millimetre-sized seeds towards a target location in the tissue. In chapter 6 of this thesis I explore this concept further by using a modified set of MR imaging gradient coil, which provides improved propulsion parameters leading to more efficient movement. The next section of this chapter will focus on introducing magnetic systems which are used to deliver magnetic particles to the tumour either for drug delivery or hyperthermia treatment.

1.2 Magnetic systems used for drug/cell targeting

The previous section introduced magnetically targeted therapies in terms of magnetic particles, mechanisms of action within the body and current preclinical and clinical literature. The focus of this section is the generation of magnetic field gradients for actuation of magnetic particles. Magnets play an important role in the therapies introduced in the previous section. Developing or choosing the ideal magnetic system for specific targeting purposes is thus very important. The appropriate selection of magnetic targeting devices depends on the anatomical target region, properties of the magnetic particle, as well as the type of steering and imaging that is required for the application. Magnetic targeting devices are classified into two broad groups: permanent magnets (e.g. bar magnets) and electromagnets (e.g. MRI systems). These devices, along with their properties, benefits, limitations, and applications are discussed in the following section.

1.2.1 Magnetic targeting using permanent magnets

A permanent magnet is a material which produces a magnetic field without electricity. Coercivity is the property of a ferromagnetic material to resist demagnetisation. Permanent magnets are made from materials with a high coercivity which, retain their inherent magnetic field after removal of external magnetic fields. Another property of interest for permanent magnets is known as remanence, which is the amount of magnetisation retained in the material at zero magnetic fields. Figure 1.3A and 1.3B provide a representation of the magnetic field lines produced by a permanent magnet and the hysteresis behaviour including the coercivity and remanence. In addition to coercivity and remanence, a quality factor for permanent magnets is the maximum energy product $(BB_0/\mu_0)_{max}$, which is the maximally attainable product of the induced flux density B in a material and the applied magnetic field strength B_0/μ_0. Graphically, this quantity can be described by the area of the largest rectangle that can be inscribed under the second quadrant (demagnetisation) of a magnet’s hysteresis (BH curve). A material with higher maximum energy product can produce a magnetic flux with a smaller volume of the material, making it lighter and more compact. Table 1 provides some of the materials used for permanent magnets and their respective coercivity, remanence and quality factor values.

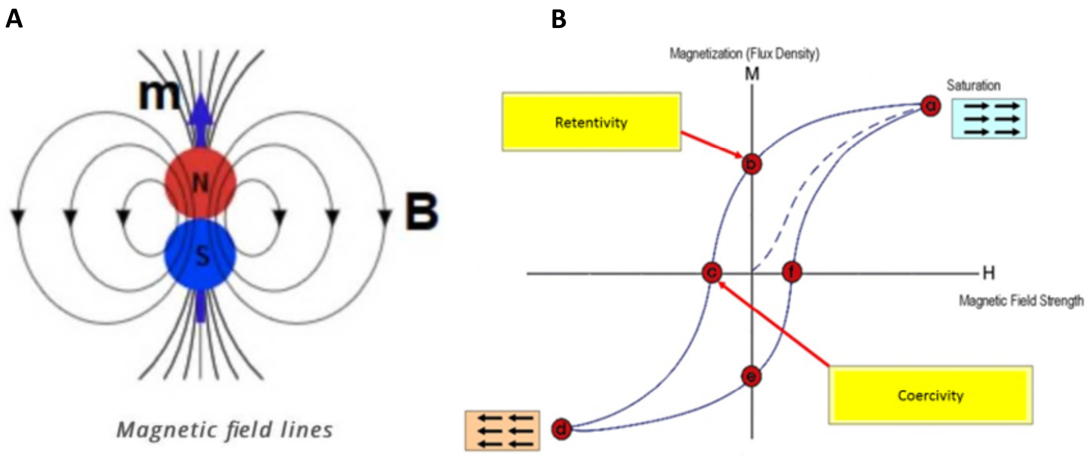

Figure 1.3- Properties of permanent magnets. (a) Magnetic field lines produced by a permanent magnet and configuration of north and south ends. (b) Hysteresis behaviour of a ferromagnetic material. (figures adopted from [105]). The red dots on the x-axis show the negative and positive coercivity and the red dot on the y-axis show the negative and positive retentivity (remaining magnetisation) values. The other remaining dots show saturation magnetisation point. The MH curve will be constant after the saturation magnetisation point, however, the induced magnetic flux density B will continue to increase in response to increase in the applied field strength B_0/μ_0.

Material	Coercivity (T)	Remanence (T)	$(BB_0/\mu_0)_{max}$ (Kj/m^3)
$BaFe_{12}O_{19}$	0.36	0.36	25
Alnico IV	0.07	0.6	10.3
Alnico IV	0.07	1.35	55
Alcomax I	0.05	1.2	27.8
MnBi	0.37	0.48	44
$Ce(CuCo)_5$	0.45	0.7	92
$SmCo_5$	1.0	0.83	160
Sm_2Co_{17}	0.6	1.15	215
$Nd_2Fe_{14}B$	1.2	1.2	260

Table 1- Permanent magnet materials and their properties (Data from [105])

Permanent magnets are the most prevalent magnetic source used in magnetic targeting studies as they are readily available and produce high magnetic forces over a relatively small area, without the need for control hardware or the cooling required for electromagnets. Among these, Neodymium Iron Boron ($Nd_2Fe_{14}B$) is the material with highest use because of its high coercivity, remanence and maximum energy product (table 1). Permanent magnets used in previous preclinical and clinical studies can be classified into two main categories: single permanent magnet and permanent magnet assembly.

Single permanent magnet is the simplest magnet for magnetic drug targeting. The magnet can be placed anywhere on the surface of the body near the lesion site (see Fig.1.1). Due to the attractive force caused by the permanent magnet, magnetically labelled therapeutics will be captured to the region near to the magnet. Various preclinical[36,5,35,106,107] and clinical[11,108] studies have utilised single permanent magnets for magnetic targeting. However, as discussed in section 1.1.1, in almost all of these investigations, the restricted spatial extent of the magnetic field and gradient (usually few millimetres) has ruled out the possibility of targeting deeper body regions. Additionally, the attraction force is always pulling the particles towards the surface of the magnet on the skin and therefore a non-optimal, uneven particle distribution is expected within the target region. One solution to these problems is to change the location of the magnet during the targeting procedure as previously demonstrated for liver targeting[109]. However, this method is highly dependent on the shape and location of the target region and is not always feasible.

Permanent magnet assembly is another solution to increase the particle targeting distance within the target region by superimposing one or more magnetic fields in an array of permanent magnets. Among many designs of magnetic assemblies, one of the best ways of increasing magnetic field gradient is the Halbach array, which was introduced by Klaus Halbach in 1979[110]. Halbach arrays are designed to increase the magnetic field by squeezing the magnetic field in one direction using a cylindrically symmetric pattern of magnetization[111]. In this way, the magnetic field on one side of the array increases and the magnetic field on the other side weakens, which can be optimised for specific applications. For example, Riegler et al.[60] conducted a comprehensive study of Halbach array designs used for cell delivery to peripheral arteries. They compared the magnetic forces caused by four kinds of magnets (annular Halbach array, linear Halbach array, triangular rod and magnetic bar). The effects of different magnetisation arrays, magnet radii, magnet thickness were also compared. The results showed that the best magnet design for the peripheral artery experiment was an annular Halbach array of 12 permanent magnets. Such magnet configuration was then developed and used to deliver magnetically labelled MSCs to regions of vascular injury in a rabbit model (Fig.1.4)[35]. Using this custom made scalable magnetic array, they were able to produce a 6-fold increase in cell retention following balloon angioplasty in the vascular injury model.

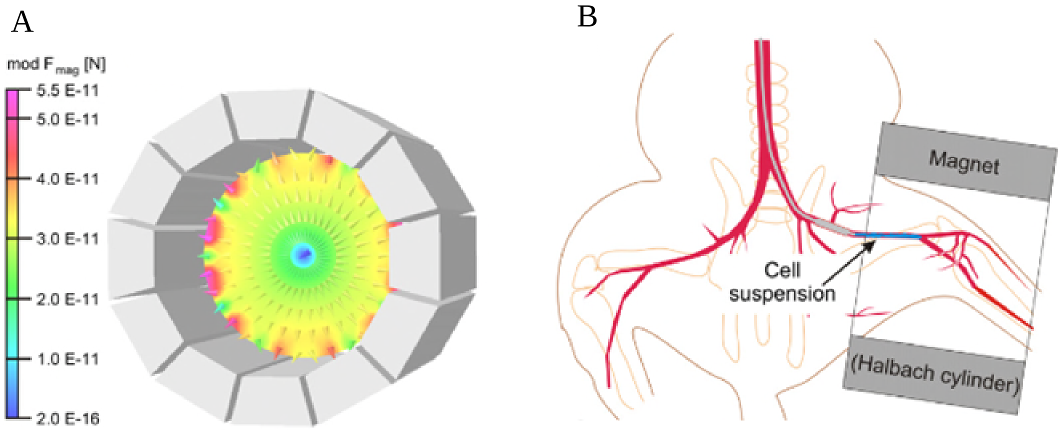

Figure 1.4- Schematic of the surgical procedure for initial balloon injury to the femoral artery in Riegler et al. study [35] (a) Simulated map for magnetic forces and cell movement in the cylindrical Halbach magnet. (b) Cell delivery after the blood flow has been stopped and the cylindrical magnet is put around the leg.

In addition to Halbach array designs, certain configurations of magnets can produce complex magnetic field and gradient shapes that even produce a pushing force away from the magnet surface. An example of this method was developed by Shapiro et al.[112] to magnetically ''inject'' nanomedicine into the inner ear, which was validated over distances relevant for use in the human ear[113]. This was achieved by a pair of bar magnets arranged in a way to produce a field overlap point which creates pushing forces away from the magnet (Fig 1.5). *In vitro* experimental results indicated that this system can be effective for treating disease of the inner ear, which intravenously injected or orally administrated treatments cannot reach due to the blood-brain barrier. Several other investigations have proposed custom designs of magnet arrays to deliver nanoparticles to a target region[114115]. Although these magnets were shown to produce large magnetic forces to push or capture nanoparticles, such investigations were only performed in theoretical simulations[114,116,115] or in small animal models[117].

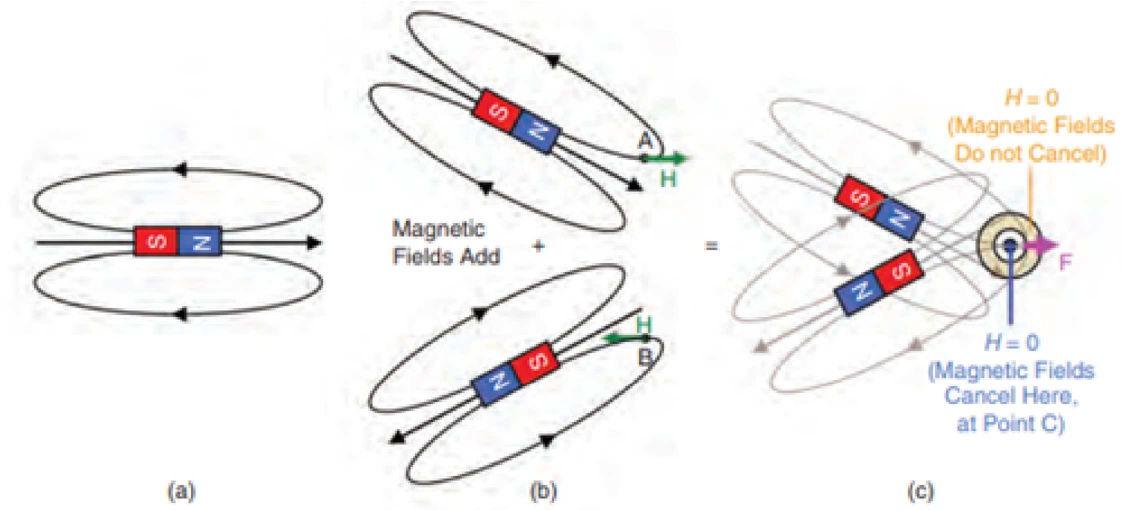

Figure 1.5 – Schematic of two magnets that can create a pushing force. As demonstrated by Shapiro et al. [112]. Particles are pushed out from the node. (a) Schematic field lines around a single permanent magnet magnetized along its length. (b) Two magnets. Tilting the top magnet down till the magnetic field Hv is along the positive x axis at the desired node location (green dot). Reversal and upward tilting of the other magnet. (c) When these two magnets are correctly overlaid, their magnetic fields combined exactly cancel at the node point C (big dot), but they do not cancel around that point (orange annulus). The resultant force is a force pushing the particles away from the magnets (The pink arrow). (In (c), the light gray lines are only guides for the eye and are not magnetic field lines.)

While magnet assemblies offer a promising solution to increase the magnitude and shape of the magnetic force produced by single magnets, each assembly design requires optimisations for a specific application. Additionally, even with all the improvements, they still remain extremely limited in the range of depths over which they can apply useful magnetic forces[118]. To address this limitation Barnsely et al. [118] designed and optimised an array of permanent magnets which was shown to be capable of capturing magnetic microparticles (0.5 μm) up to a distance of 5 cm away from the magnet surface during *in vitro* flow experiments. Although this magnet assembly is the most optimised design to increase the targeting depth for nano/micro sized particles, to date there is no *in vivo* demonstration of such a magnetic setup.

Implantation of ferromagnetic materials into patients, such as within blood vessel walls, has been suggested as a way of targeting deeper tissues[119,120,121]. The implanted materials are designed to locally increase magnetic field gradients when an external magnetic field is applied. Such treatment could be an appropriate solution for treating tumours that cannot be surgically removed, provided the magnetisable implants can be inserted into or near the tumour. However, this method requires invasive procedures and is only useful for areas that are accessible for this purpose.

In summary, the review of the permanent magnet designs in the literature indicates that although permanent magnets are the simplest strategy for magnetic targeting experiments, the sharp spatial decline in their magnetic force limits them to small animal models or superficial regions of the human body. Permanent magnet assembly designs aim to increase the targeting depths but only a few successful investigations have proposed effective solutions for highly specific applications (body regions) located < 5 cm within the body. As stated previously, in chapter 4 of this thesis I introduce and investigate novel magnetic designs, which aim to improve the distance limitation of permanent magnets used for nanoparticle targeting. The next section will aim to introduce the literature on the use of electromagnets in magnetically targeted therapies.

1.2.2 Magnetic targeting using electromagnets

An electromagnet is a type of magnet in which the magnetic field is produced by an electric current. Electromagnets usually consist of wire wound into a coil and a current through the wire creates a magnetic field which is concentrated in the centre of the coil. The magnetic field disappears when the current is turned off. To concentrate the magnetic flux and increase the magnetic flux produced by the magnet, the wire turns are often wound around a magnetic core made from a ferromagnetic or ferrimagnetic material such as iron. Modern computer-interfaced electromagnet-based systems offer the ability for dynamic control of magnetic field strength and gradients which can be used for active guidance of magnetic particles in a three-dimensional scale. The design of the electromagnet depends on the anatomy of the target region within the body as well as factors such as shape, size, current or voltages needed to produce the require magnetic fields. The electromagnet systems used for magnetic targeting studies can broadly be classified into three main groups, which include conventional electromagnetic coils, superconducting magnets and the gradient coils inherent to MRI scanners.

The main advantage of an electromagnet over a permanent magnet is that the magnetic field can be quickly changed by controlling the amount of electric current in the winding, which provides both spatial and temporal control on the targeting process. The simplest form of an electromagnet design is built by using ordinary coils. The magnet system can simply be an electromagnet with a single coil, or a mixture of two or more electromagnetic configurations. There is a wealth of literature on theoretical design and optimisation of electromagnetic setups for magnetic drug targeting[122-115]. However, only few studies have successfully tested the efficiency of their systems using *in vivo* experiments[123-124]. Among these *in vivo* studies, a tip-top electromagnet design (Fig.1.6) is most popular as it produces a higher magnetic field gradient compared to a simple coil design[111]. Although the tip-top electromagnet designs used in these studies produced promising magnetic targeting results, similar to permanent magnets, the distance over which they could apply sufficient magnetic forces was extremely limited and only useful for small animal models.

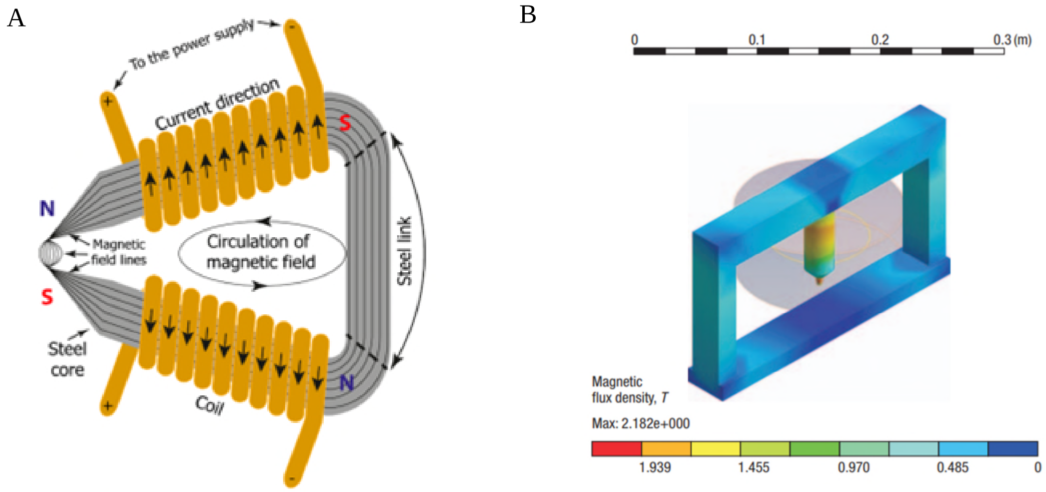

Figure 1.6- Schematic of previously developed tip-top electromagnetic designs. (a) The tip-top electromagnet design developed by Voronin et al., [125] that was employed for an *in vivo* trapping of the microcapsules in rat mesenteric vessels. (b) The tip-top electromagnet design developed by Dames et al., [124]. The windings of the coil are shown as a transparent cylinder-the windings cover the cylindrical surface of an iron-cobalt core (coloured region) but not the sharp end of the core. The magnetic flux density is shown as a multicolour plot.

To improve this limitation, a special class of electromagnets called superconductors are introduced. Superconductors produce very large field strength values (up to 21T in high field preclinical MRI scanners) however like permanent magnets; they do not provide the dynamic control on their field strength. Takeda et al.[126,127] developed a superconductive navigation system (Fig. 1.7 A) to direct magnetic carriers in drug delivery investigations using *in vitro* phantom experiments. They showed that their bespoke system produces larger magnetic field gradients at the same distances away from the magnet when compared with the traditional electro or permanent magnets (Fig. 1.7 B)[126]. However, to my knowledge, there has been no *in vivo* studies to investigate the efficacy of this system further.

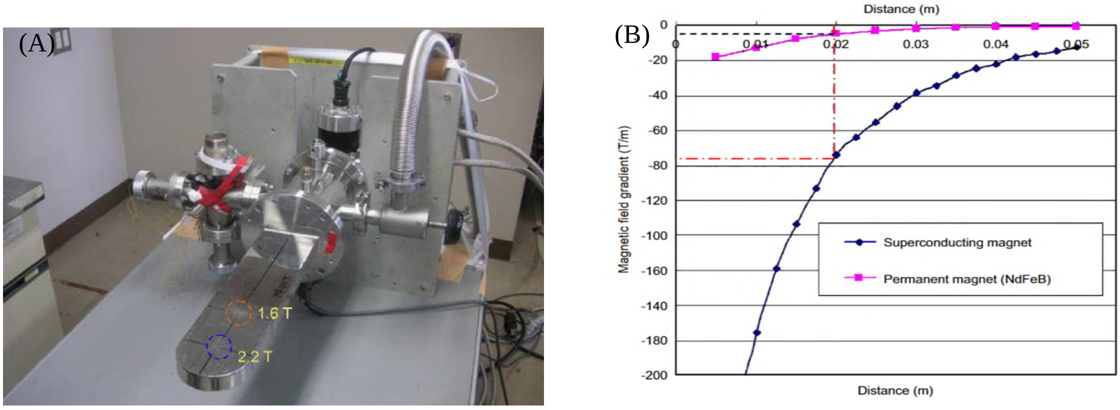

Figure 1.7 - The superconducting magnet developed by Takeda et al for magnetic drug targeting[127]. (A) Photograph of the magnet. (B) Comparison of the magnetic field gradients generated by permanent and superconducting magnet as a function of distance from the magnet surface. Magnetic gradient produced by the superconducting magnet is notably larger than the corresponding value produced by a permanent magnet at the same distance.

In addition to the discussed investigations, the video tumour fighter and magnetic stereotaxic projects developed two electromagnets, which included a water cooled[2] and a superconducting electromagnetic system[128] to guide a thermoseed along some arbitrary trajectory through brain tissue. In order to image and track the movement of the thermoseed in the brain they utilised fluoroscopic imaging and used fiducial markers to register these images with pre-acquired MR images. However, as discussed previously in section 1.1.3.2, the inherent registration errors between the two imaging modalities reduced the overall accuracy of the method. In addition to the imaging limitation, the electromagnets used in these studies were shown to have limitations in terms of providing orientation and moving force to the thermoseed. The authors concluded that the movement of an untethered thermoseed had proved to be quite difficult and could not be reliably achieved, because certain locations within the magnets exhibited misalignment of the magnetic field (orientation) and magnetic gradient (moving force). As a result, the magnetic thermoseed had a tendency either to move off axis or not to move at all[129].

An exciting, alternative approach is Magnetic Resonance Targeting (MRT)[63] that uses the magnetic field gradient coils inherent to all MRI systems, to steer magnetic particles (or cells containing them) to a target site within the body. While the gradients can provide controllable spatial magnetic force with the same magnitude throughout the imaging volume, the imaging capability can provide feedback control on particle location during delivery. As such, this system has three main advantageous for targeting magnetic particles when compared to permanent magnets or other electromagnet systems. These include the spatial controllability, depth penetration, and the ability to perform near real time imaging, which makes MRT an exciting method for magnetically targeted therapies.

Although this strategy offers significant advantage over other methods, unless the conventional MRI scanners are modified[130,131,132], the force they apply on nano/micro-sized particles is extremely limited due to the small field gradients generated by clinical imaging gradient coils, which are typically < 80 mT/m. One way to increase this force is to use larger magnetic particles, which leads to much higher control over particle targeting to regions of interest within the body. To investigate this method, precise magnetic control of a single millimetre-sized magnetic object has been demonstrated using the MRI scanner for navigation and tracking of micro-robots in the vascular network[133-134]. This method (known as magnetic resonance navigation) provides an exciting way to propel magnetic objects using clinical gradient strengths, however, the need for navigation of the magnetic particle through the vascular system limits the targeting ability to regions of the body with large vessel networks.

Another way to increase the magnetic force is to use preclinical MRI systems which are capable of producing larger magnetic field gradients. To demonstrate this method, a gradient strength of 500 mT/m has been used in proof-of-concept MRT experiments to steer human cells loaded with magnetic nanoparticles in vascular flow models *in vitro*[135,63]. Further investigations expanded upon this to target oncolytic iron-oxide loaded microphages to prostate tumours *in vivo*, which resulted in enhanced tumour necrosis[31]. In addition to the use of preclinical scanners, in order to be able to magnetically control smaller sized particles, the use of additional gradients to conventional clinical MRI scanners has also been investigated (see section 2.3.3). Magnetic drug-encapsulating microparticles have been directed in this way to the right or left lobe of the rabbit liver as a potential drug-delivery and chemoembolization method for tumour metastases[133]. Additionally, steering of nano-scaled manetotactic bacteria around a maze was demonstrated by introduction of a custom-made gradient coil into a clinical MRI scanner[136,137].

The success of delivering ferromagnetic objects[138], drugs[133] and cells[63] using the MRI scanner at any depth within the body, provides an attractive solution to the depth penetration limitation of conventional permanent and electromagnets. In addition to depth penetration, magnetic targeting with MRI systems has its specific advantages. First, the MRI system can provide anatomical images, so the position of the particles and the distribution of the blood vessels in the body can be observed by imaging. Secondly, the MRI system can calculate and correct the motion and adjust the generation of the magnetic gradient through feedback control algorithms, so as to navigate the magnetic particles in the pre-planned path.

2. Physical principles of magnetic targeting

Chapter 1 of this thesis provided an introduction on previous investigations of magnet targeted therapies using magnetic particles and systems used to deliver them. This chapter will focus on introducing the physical principles of magnetic targeting of nanoparticles, which are delivered through intravascular route as well as the principles of magnetic resonance targeting of seeds delivered through tissue. I will first present the basic principles of magnetism and magnetic properties of different materials. Following that, physical forces involved in magnetic targeting of nanoparticles and seeds are discussed in their respective sections. In the last section of this chapter, I will provide a brief overview on basic principles of magnetic resonance imaging and the essential hardware components used in this system.

2.1 Basic principles of magnetism

This section will focus on physical principles of magnetism and magnetic properties of matter. These principles will provide the basic understanding on how magnetic field produced by permanent magnets and MRI scanners can be used to target magnetic nanoparticles and seeds to tumours respectively; which will be further discussed in the following sections.

2.1.1 Magnetic fields

A magnetic field is an area of space with increased energy density and an energy gradient to its surrounding. This energy density can be caused by the spatial movement of a charged particle such as an electron[139] (Fig. 2.1), or the spin of a particle around its axis (as it happens in the case of the hydrogen protons that give the MRI signal, section 2.3.1). Most materials have orbitals which contain paired-up electrons pointing in opposite directions and therefore a zero net magnetic field is produced by movement of electrons. However in ferromagnetic materials (e.g. neodymium, iron and nickel), there are orbitals which contain unpaired electrons which can be aligned to make a net magnetisation (Fig. 2.2, right). Another way of producing magnetic fields takes place in electromagnets by the flow of the electrons through a coil of wire (Fig. 2.2, left). Magnetic field generated by a charged particle circulating through a current carrying loop is calculated using the Biot-Savart law[139].

$$B = \int \frac{\mu_0}{4\pi} \frac{Id\mathbf{l}\times\mathbf{r}}{r^2} \tag{2.1}$$

Where μ_0 the magnetic permeability of free space, I is the current in the loop, $\mathbf{l}$ is the vector of the current carrying element and r the distance between the conductor and the field point with unit vector $\mathbf{r}$.

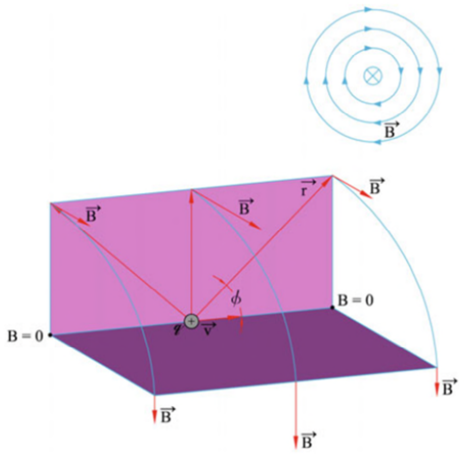

Figure 2.1- Magnetic field produced by a moving charge (adapted from [140])

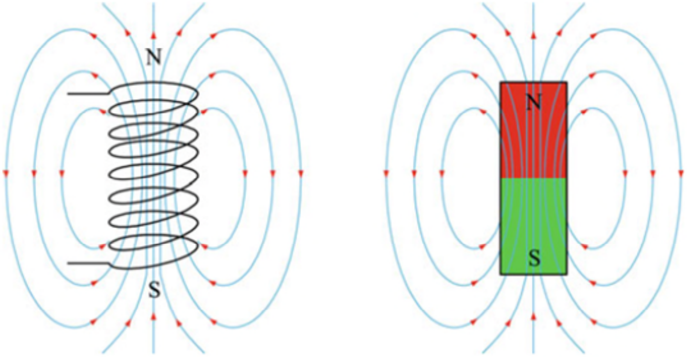

Figure 2.2- Magnetic field in a solenoid electromagnet (left) and permanent magnet (right) (adapted from [140])

Two notations are used to describe the magnetic field, first being the magnetic field strength ***H*** (measured in A/m) and second being the magnetic flux density ***B*** (measured in Tesla). ***H*** is defined as the field produced in the centre of a 1 metre diameter current loop carrying 1 A of current. ***B*** can be described as the density of the magnetic field induced in (or felt by) a material when exposed to a field ***H***. ***B*** and ***H*** are connected by the equation 2.2.

$$\boldsymbol{B} = \mu_0(\boldsymbol{H} + \boldsymbol{M}) \qquad 2.2$$

With $\boldsymbol{M}$ the magnetisation of the material in A/m.

2.1.2 Magnetic properties of matter

Different materials show different response when exposed to external magnetic fields. This is characterised by a property known as magnetic susceptibility (χ) which is defined as equation 2.3.

$$\chi = \frac{M}{H} \tag{2.3}$$

$$M = \frac{\boldsymbol{m}}{V} \tag{2.4}$$

where $\boldsymbol{m}$ is the magnetic moment on a volume V of the material.

Depending on their behaviour when exposed to the magnetic field, materials are classified by different magnetic characteristics [34]. A summary of such behaviour types is shown in figure 2.3, which includes the induced magnetization of a magnetic material on the y-axis and the value for applied magnetic field strength on the x-axis (known as B-H characteristics).

(i) Diamagnetism: Materials with a negative susceptibility value are classified as diamagnetic. When diamagnetic materials are exposed to magnetic field, the orbital momentum of their electrons change in a way to create a weak magnetisation which opposes the external magnetic field (Fig. 2.3 a). This property is possessed in all atoms however it can only be observed in materials which show no other form of magnetic behaviour.

(ii) Paramagnetism: Materials with small positive susceptibility values $(10^{-5} - 10^{-2})$ are classified as paramagnetic. Due to the spin of the unpaired electrons and contribution from orbital angular momentum, magnetic moments are created, which are randomly oriented. When a magnetic field is applied, magnetic moments change their orientation and align themselves reversibly with the direction of the applied field (Fig. 2.3 b).

(iii) Ferromagnetism: Materials with high susceptibility values $(10^{2} - 10^{5})$ are classified as ferromagnetic. Due to the interaction of magnetic moments created by the unpaired electron spins, these materials are composed of a group of aligned moments which are oriented in a random direction in a region called domains (Fig. 2.3 l, m). Depending on the size of the material, they may form a multi domain state (in the order of micron size or more) with multiple random orientations or a single domain state (in the order of sub-micron size) that are all aligned in the same direction. The size at which the multi-domain converts to single-domain structure depends on the material type. When exposed to magnetic field, domain boundaries start to move and increase the net alignment of all domains parallel to the applied field. Once the magnetic field is removed, these materials can retain their magnetisation leading to a residual flux density (B_r). If a large enough magnetic field (coercive field H_c) is applied, the residual magnetisation can be reversed. Ferromagnetic materials undergo a transition to a paramagnetic state above a certain temperature called the Curie temperature. Additionally, there is a maximum magnetisation which can be induced in such materials known as the saturation magnetisation (M_s). B-H curves are frequently used to illustrate the induced magnetisation as a function of applied magnetic field, also known as hysteresis behaviour of ferromagnetic materials.

(iv) Antiferromagnetism: This is found in materials with special crystal structures. Magnetic moments are parallel to one another inside individual sub-lattices but antiparallel to neighbouring sub-lattices. Therefore, in the absence of magnetic field, no net magnetisation exists in antiferromagnets. However, in a special class of antiferromagnetic materials, known as ferrimagnetism, magnetic moment of sublattices are unequal leading to a net magnetisation.

(v) Superparamagnetism: This behaviour is found in ferromagnetic and ferrimagnetic materials with sufficiently small size (of the order of tens of nanometres or less). Examples of such material are nanoparticles with a core consisting of a single magnetic domain. In such nanoparticles, magnetisation can randomly flip direction under the influence of temperature. The time delay between two flips is called the Néel relaxation time (see section 1.1.3.1). In the absence of magnetic field, the time used to measure magnetisation of such particles is much longer than the Néel relaxation time leading to a measured net magnetisation of zero. These materials exhibit magnetisation similar to ferromagnetic materials in a magnetic field. However, the amount of induced magnetisation for a given applied field is much higher than observed for paramagnets and they show saturation magnetisation similar to other ferromagnetic and ferrimagnetic materials (Fig. 2.3 d). Additionally, superparamagnetic materials retain no magnetisation after removal of the magnetic field.

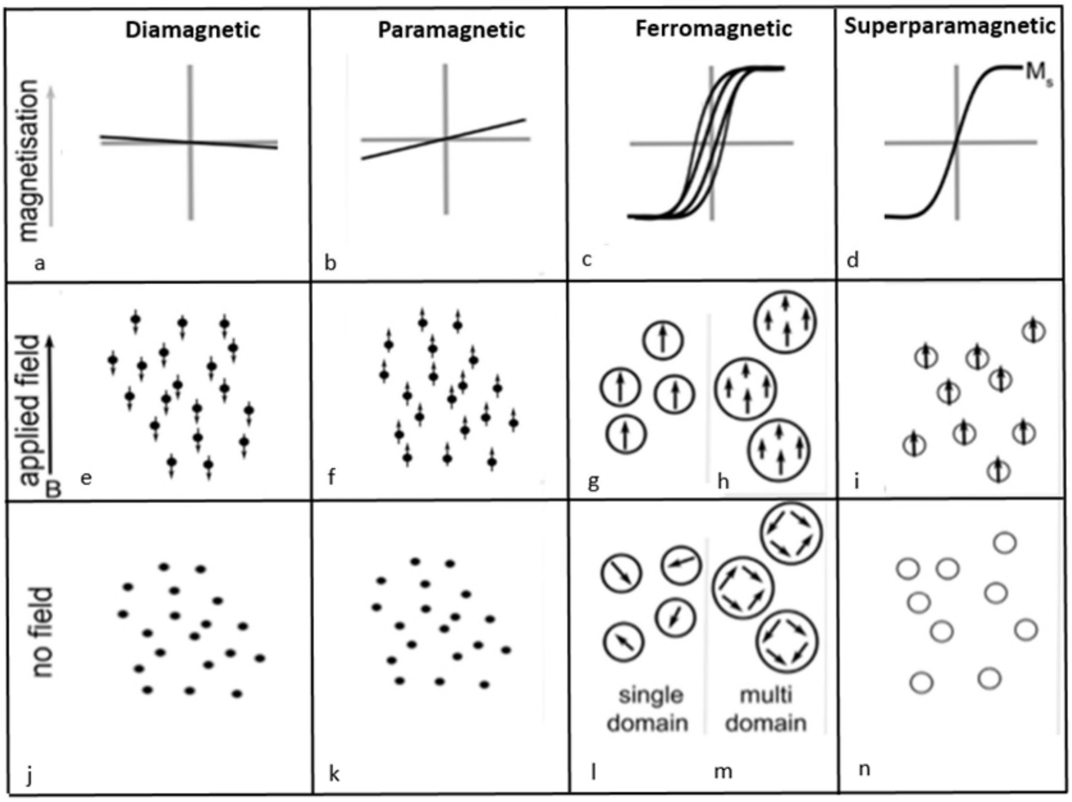

Figure 2.3- Magnetic behaviours induced by external magnetic field in materials (adapted from Patrick et al[34])

2.2 Magnetic targeting of nanoparticles from vasculature

In this section of this chapter, I will provide an introduction on properties of magnetic nanoparticles and the physics behind the use of external magnetic fields to capture these particles whilst flowing in blood vessels. Magnetic capturing and hydrodynamic drag forces are discussed in separate sections. These principles provide the basis for chapters 3 and 4 of this thesis.

2.2.1 Properties of magnetic nanoparticles

As indicated in section 1.1.2.1, magnetic nanoparticles are comprised of a magnetic core and a chemically synthesized surface coating. The size and material of the core affect the type and potential strength of magnetism that particles display, which in turn influences particle's behaviour in magnetic targeting applications. For example, in the lower nanometre range (2-30 nm depending on the material), most iron, nickel and cobalt-based materials are superparamagnetic[66]. This means these particles are only magnetic in the presence of an external magnetic field, and their magnetism increases with external magnetic field strength up to their saturation magnetisation (see section 2.1.2).

When a particle is in the single-domain state, its internal magnetisation is aligned in the same direction. In the application of magnetic field, multiple neighbouring particles that are initially magnetised in varying directions (along their easy axis of magnetisation) will align with the direction of the magnetic field, or against their easy axis if they are not free to rotate. This phenomenon increases the net magnetisation of the group and therefore, the amount of directional magnetic force that can be applied on particles by a field gradient. However, in the absence of external magnetic field individual particles have domains with varying directions, which leads to a zero net magnetisation. Such zero net magnetisation allows superparamagnetic nanoparticles to significantly avoid magnetic aggregation (a common problem with magnetic particles, see section 1.1.2.1). This property provides these particles with an advantageous characteristic in biomedical applications.

One of the most important parameters of nanoparticles for magnetic targeting applications is magnetic susceptibility, as it is proportional to the amount of magnetic force that can be applied below magnetic saturation field strength. As such, to compare the suitability of different nanoparticles for specific targeting applications, their magnetic susceptibility properties can considered. This is particularly important when it comes to utilise particles which were not designed for effective force production such as the ones synthesised as MRI contrast agents. While some MRI contrast agents are not suitable for magnetic targeting, some SPIONs which were originally designed for imaging applications do have suitable magnetic susceptibility for effective force production[34]. For example, SPIO particles which were approved for human use by the FDA, such as Endorem (Feridex), and Ferucarbotran (Resovist) have previously been used successfully for a number of preclinical magnetic targeting studies[61].

Magnetic nanoparticles used in this study (50 and 100 nm FluidMAG, Chemicell) are made of a magnetite (Fe_3O_4) core, which is a ferrimagnetic material by nature and is the most magnetic of all the naturally-occurring minerals on earth[141]. In addition to their large magnetic susceptibility, magnetite cores exhibit superparamagnetic behaviour due to their small size; making them suitable both for magnetic targeting and MR imaging applications. As discussed in section 1.1.2.1, we chose to investigate magnetic targeting of these particles in order to test the efficacy of our magnet designs discussed in chapters 3 and 4 of this thesis. Next section will focus on the physics behind the magnetic force applied on these particles when exposed to external magnetic fields.

2.2.2 Forces applied by permanent magnets on nanoparticles

A magnetic moment experiences two types of forces when placed in a magnetic field. One is the torque, which forces the dipole to align its moment with the field and the other is a translational force, which pulls the dipole towards a region of higher magnetic flux density if a field gradient is present. The applied torque is defined by the equation 2.5 and the translational force is demonstrated by equation 2.6[32] .

$$\boldsymbol{\tau} = \boldsymbol{m} \times \boldsymbol{B} \qquad 2.5$$

$$\boldsymbol{F_m} = (\boldsymbol{m}.\nabla)\boldsymbol{B} \qquad 2.6$$

$\nabla = (\frac{\partial}{\partial x}, \frac{\partial}{\partial y}, \frac{\partial}{\partial z})$ is the vector gradient operator.

Induced magnetisation in a material ($\boldsymbol{m}$) in a magnetic field ($\boldsymbol{B}$) can be approximated by the equation 2.7.

$$\boldsymbol{m} = \frac{\Delta\chi V_m}{\mu_o}(\boldsymbol{B}) \qquad 2.7$$

Where $\Delta\chi$ is the relative magnetic susceptibility and V_m is the volume of the magnetic particle.

The combination of equations 2.6 and 2.7 will lead to the general translational force equation 2.8.

$$\boldsymbol{F_m} = \frac{\Delta\chi V_m}{\mu_o}(\boldsymbol{B}.\nabla)\boldsymbol{B} \qquad 2.8$$

For paramagnetic materials, susceptibility is directly proportional to the applied magnetic field. However, the most common material used for magnetic particles are iron oxides which show ferrimagnetic behaviour. In such situations, $\Delta\chi$ will be replaced by the Langevin function, which provides an approximation to the B-H characteristics of the particles as described in equation 2.9.

$$\frac{M}{M_S} = \coth(\varepsilon) - \frac{1}{\varepsilon} \qquad 2.9$$

$$\varepsilon = \frac{\pi D^3 \mu_0 M_S \left|\frac{\boldsymbol{B}}{\mu_o}\right|}{6K_b T} \qquad 2.10$$

M_S is the saturation magnetisation of the particle, D the particle diameter, T temperature, $\left|\frac{\boldsymbol{B}}{\mu_o}\right|$ magnitude of the applied field strength and K_b Boltzmann's constant.

When the particles have not reached saturation magnetisation ($M < M_S$), it can be seen from the equation 2.8 that the magnetic force applied on them is proportional to $(\boldsymbol{B}.\nabla)\boldsymbol{B}$ (referred to as B.gradB throughout this thesis) quantity which is equivalent to the gradient of the magnetostatic field energy density $(\nabla(\frac{\boldsymbol{B}^2}{2}))$[32] that is a vector quantity, meaning that the magnitude of the applied force is both dependent on the magnitude of the applied magnetic field strength and the spatial gradient of the field strength and its direction is towards the steepest ascent of the energy density scalar field. As such, in chapters 3 and 4 of this thesis, B.gradB is used to describe the magnetic force produced by permanent magnets.

At the saturation point, the particle magnetization will not increase any further in response to increase in the magnetic field strength and the magnetic force applied on the particle will be explained by the equation 2.11[63].

$$\boldsymbol{F}_m = V(M_s.\nabla)\boldsymbol{B} \qquad 2.11$$

In this case, the force exerted on the particles will only be proportional to the $\nabla\boldsymbol{B}$ term, which is the spatial gradient of the magnetic field strength. This equation will form the basis of the magnetic propulsion force generated by the MRI system. Section 2.3.4 will provide a more detailed explanation on this method.

2.2.3 Fluid dynamics of intravascular delivery

Fluid dynamics is the study of flowing liquids and gases. For the purpose of this thesis, a brief introduction into some properties of liquids is necessary to appreciate the physical principles of the forces counteracting the magnetic force on the particle whilst in a flow. Below is a summary of some insightful properties of liquids in flow[142].

Newtonian and non-newtonian fluids: When it comes to modelling and characterisation of applications involving fluid flow, viscosity is one of the most important factors. Viscosity is defined as a fluid’s resistance to flow in simple terms. For Newtonian fluids, viscosity is only dependent on temperature, no matter how fast they are pushed to flow through a channel or pipe. In contrast to Newtonian fluids, non-Newtonian fluid’s viscosity is also dependent on the shear rate, which is the rate at which fluid layers move past each other. All gases and most common fluids, such as water, are Newtonian fluids.

Incompressible and compressible fluids: Incompressible flow refers to the fluid flow in which the fluid’s density is constant. In the context of this thesis all the flows will be considered incompressible, which is a valid approximation for all liquids.

Laminar vs turbulent flow: In order to be able to determine whether a flow is laminar or turbulent, a dimensionless parameter called the Reynolds number needs to be calculated. Reynolds number is equal to the ratio of the inertial and viscous forces in a fluid, as indicated by the equation 2.12 in a simplified way.

$$Re = \frac{\rho U L}{\mu} \tag{2.12}$$

Where ρ is the fluid density (kg/m^3), U is flow velocity (m/s), L is the characteristic length scale (m) and μ is the fluid viscosity (kg/ms).

At low Re number values, each particle of the fluid follows a smooth path without interference with one another, leading to the laminar flow. In laminar flow, the viscous forces are dominant which will result in parallel layers of flow that do not disturb one another. On the other hand, at higher Re number values where inertial forces are dominant, particles have chaotic changes in pressure and flow velocity, which causes another form of flow known as Turbulent flow. The transition Re, above which flow starts to become turbulent depends on whether the flow under consideration is internal (e.g. flow in a pipe) or external (e.g. flow on a water fall). Figure 2.4 indicates laminar and turbulent flows in a simplified demonstration. Internal flows with Re < 2300 are normally considered as laminar.

When considering internal flow, there is no relative motion between the fluid and solid particles at boundaries between the fluid and the solid material. This causes a boundary layer with zero velocity known as ''no-slip'' condition. If the flow is laminar and the solid material is a semi-circular cylindrical pipe, the velocity increases linearly, so that the flow reaches a maximum velocity at the top (open end of the pipe) of the flow field. In the case of a fully closed cylindrical pipe, the velocity follows a parabolic flow profile, as indicated by the laminar flow in figure 2.4. Parabolic laminar flow profile is considered as the model of choice in a vast majority of magnetic targeting applications.

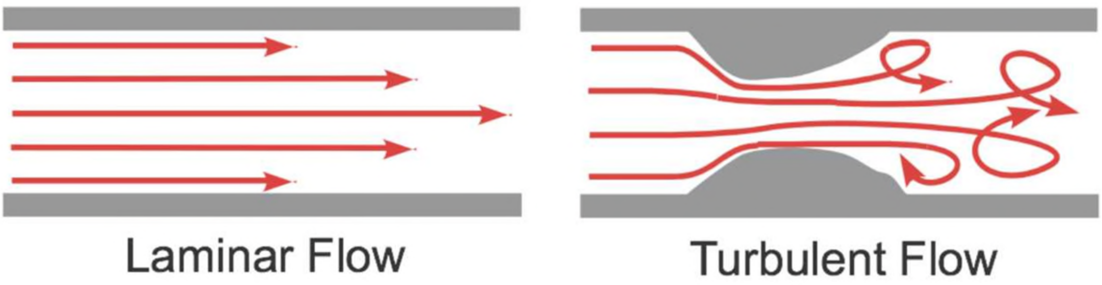

Figure 2.4- Laminar parabolic flow (left) and Turbulent flow (right) (adopted from[142])

2.2.4 Hydrodynamic drag force

Hydrodynamic drag is the force applied on an immersed body whilst moving in a fluid. If we assume that the immersed body is a sphere and the Re number is very low (Re < 1) then the hydrodynamic drag force can be modelled by the Stokes drag force, which is explained by the equation 2.13.

$$\boldsymbol{F_d} = 6\pi\mu\boldsymbol{u}R_s \tag{2.13}$$

Where $\boldsymbol{u}$ is the difference between the fluid and sphere velocity and R_s is the radius of the sphere.

Stokes drag force is dependent on the shear stress and surface area of the particle, however, since the shear stress is by approximation equal to $\mu\frac{\boldsymbol{u}}{R}$, rearrangement of the equation leads to the proportionality of the drag force to the radius of the particle.

In a vast majority of magnet targeted therapy applications, Stokes drag force is used to model the hydrodynamic drag force applied on spherical magnetic particles whilst flowing in body vasculature. In addition to the stokes drag force, a number of other forces are applied on a flowing particle in a blood vessel such as the dipole-dipole interactions, gravitational, buoyancy forces and Brownian motion. However, since the magnitudes of such forces are negligible, they are disregarded in almost all magnetic targeting simulations. Figure 2.5 provides a free-force diagram of a particle flowing in a blood vessel under the influence of an applied external magnetic field.

As indicated by equation 2.8, the magnitude of the applied magnetic force is dependent on the volume of the particle. Nonetheless, the hydrodynamic drag force is proportional to the radius of the particle. This implies that if the volume of the magnetic particle is increased, the resultant attractive force in the vicinity of the applied magnetic field is increased, which leads to a higher chance of successful magnetic targeting within the target region. However, on the other hand, increasing the particle size will result in an increased rate of particle clearance by the macrophage system within the body and consequently less passive particle delivery to the target region. In conclusion, choosing the appropriate particle size is an important step to achieve efficient magnetic targeting in any part of human body.

This section of this chapter outlined the main physical principles governing magnetic targeting of nanoparticles post intravenous injection. The next section will focus on the physics behind magnetic resonance imaging and the hardware used to image and actuate magnetic particles using the MRI system.

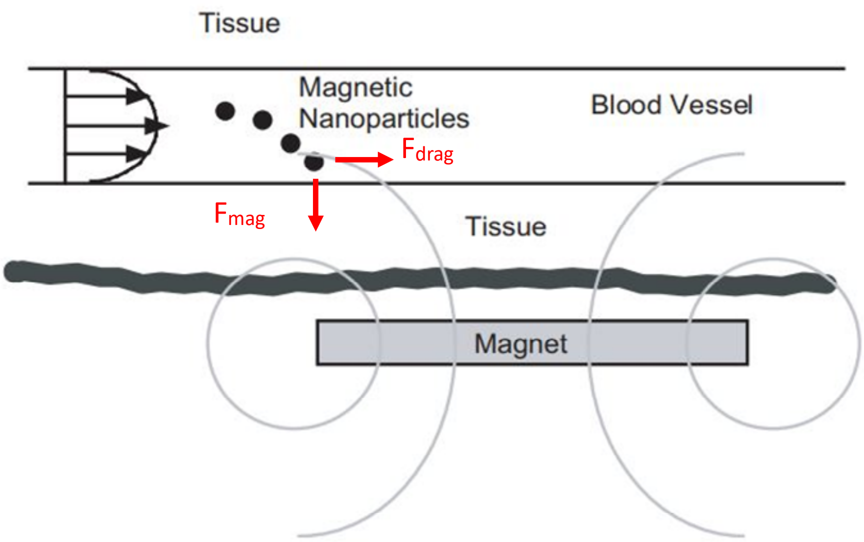

Figure 2.5- Application of the magnetic and hydrodynamic drag force on a magnetic nanoparticle in a hypothetical model of magnetic targeting system. (adopted from [32]).

2.3 Magnetic Resonance Targeting of seeds in tissue

The main goal of this section is to provide a brief introduction on magnetic resonance targeting of magnetic particles. Today, magnetic resonance imaging is a widely used imaging technology. Besides its non-invasiveness, its ability to generate different contrasts in soft tissues gives rise to the increasing importance in diagnosis of distinct diseases. In addition to its ability to provide high-resolution anatomical images, it has also shown to be effective in delivering therapy due to the magnetic force it applies on magnetisable agents (see section 1.2.2). To understand the physics behind magnetic targeting using the MRI system, it is important to provide a basic overview over principles of magnetic resonance imaging. This overview is followed by a description of main hardware components used for imaging and an introduction on gradient coils, which are the main MR hardware equipment that are used to produce translational force on magnetic particles.

2.3.1 Magnetic Resonance Imaging

Because of its abundance in the human body, hydrogen is used as the main source of signal for MRI. When a nucleus contains either unpaired protons, neutrons, or both, it has a magnetic moment with angular momentum, which provides the basis for MRI. In the presence of a strong, constant external magnetic field, such as that produced inside an imaging magnet, a small excess fraction of hydrogen nuclei, on average, align themselves with the magnetic field, producing a macroscopic, measurable magnetic moment (Fig. 2.6 A). The interaction between the magnetic moment of the nucleus and the external field causes the precession of each magnetic moment (i.e. change the orientation of the rotation axis of the spinning nucleus). The precession takes place at a characteristic (resonant) frequency that is proportional to the strength of the external field. This is known as the larmor frequency and is given by the equation 2.14.

$$\omega_0 = \gamma B_0 \qquad 2.14$$

Where ω_0 is the angular frequency of the magnetic moment, γ is the gyromagnetic ratio which is a property of the specific nucleus and B_0 is the main field of the MRI.

The MR signal is generated by subjecting the precessing moments to radiofrequency (RF) pulsations which rotate their magnetisation vector into the X-Y plane (Fig. 2.6 B). In MRI systems the Z axis is aligned with B0. The precession of the magnetisation in the X-Y plane can be detected via the induced current in a coil tuned to the Larmor frequency, the receiver coil (Fig. 2.6 C). Once the RF pulse is turned off, the magnetisation gradually returns to the equilibrium (along the Z axis) via the spin-lattice relaxation. The spin-lattice relaxation is the recovery of the Z component of the magnetisation vector as the system returns to reach its original magnetisation given by the equation 2.15. This recovery of magnetisation can be illustrated by the M_z (z component of the magnetisation) vs time graph shown in figure 2.6 D.

$$M_z\,(t) = M_0(1 - \exp\left(\frac{-t}{T_1}\right)) \qquad 2.15$$

Where M_z is the magnetisation in the z direction, M_0 is the equilibrium magnetisation and T_1 is the spin-lattice relaxation time.

As the magnetisation returns to equilibrium, an independent relaxation process takes place as the transverse magnetisation decays from its maximum (for a perfect 90° RF excitation) to zero, known as the spin-spin relaxation. The transverse relaxation time T_2 specifies the mono-exponential decay rate of transverse magnetisation, which is caused by the magnetic interaction between spins and leads to loss of phase coherence (equation 2.16). *In vivo* relaxation due to spin-spin interactions takes place faster than relaxation due to spin-lattice interaction. Thus T_2 is shorter than T_1. Similar to longitudinal magnetisation, the decay of transverse magnetisation can be illustrated in M_{xy} vs time graph (Fig. 2.6 E).

$$M_{x,y}\,(t) = M_0\,\exp\left(\frac{-t}{T_2}\right) \qquad 2.16$$

Where $M_{x,y}$ is the magnetisation in the xy plane and T_2 is the spin-spin relaxation time.

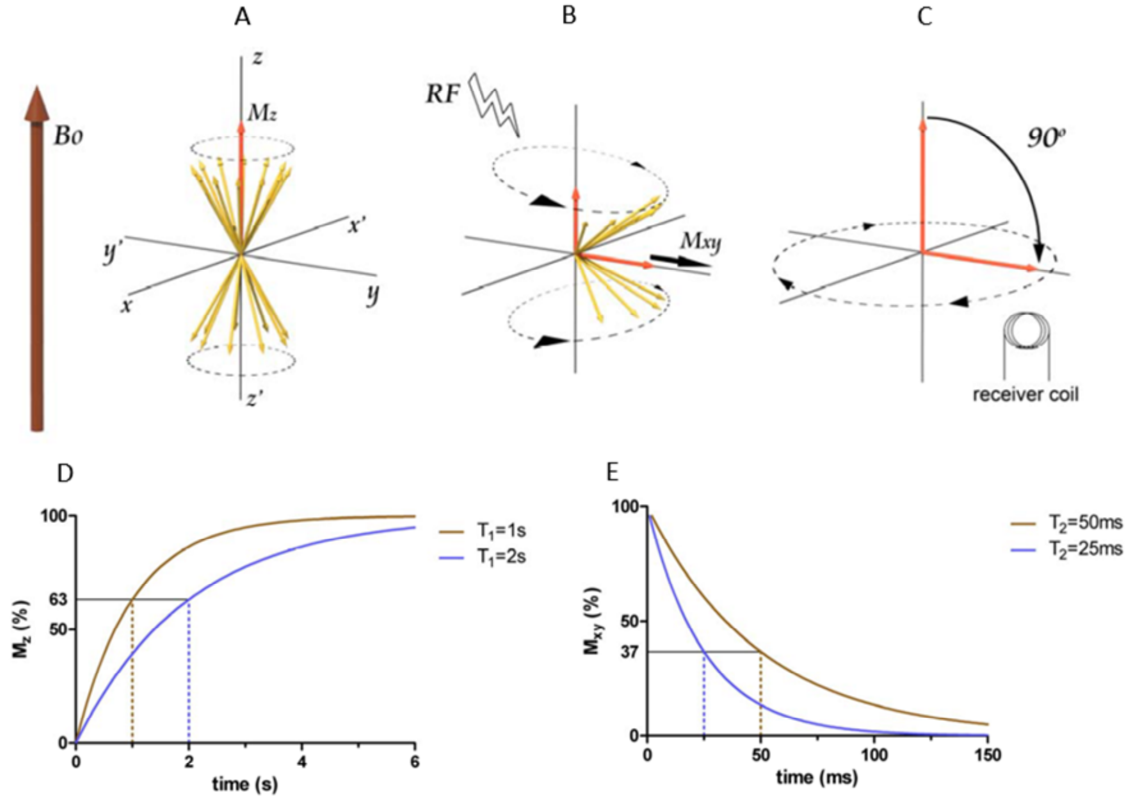

Figure 2.6 - Simplified graphical representation of the RF excitation process in MR. (A) Application of B_0 results in alignment and precession of the magnetic moments with the axis of B_0, creating a net tissue magnetisation M_z. (B) Application of an RF pulse leads to precession phase coherence and tilting of the precession axis, causing a drop in M_z and an increase in M_{xy} .(C) This is represented as tilting of the magnetisation from the z axis to the xy plane. (D) T_1 relaxation. (E) T_2 relaxation. Figure adopted from[143].

In addition to natural magnetic interaction of spins, a second mechanism causes decay of transverse magnetisation. Once the RF is switched off, each magnetic moment is free to rotate at its own Larmor frequency, which is affected by the magnetic field it is experiencing. Due to local, time–invariant, field inhomogeneities (such as those introduced by boundaries of tissue of different magnetic susceptibility), the magnetic moments start to lose their phase coherence, eventually bringing M_{xy} to zero. T_2^* relaxation takes the decay of M_{xy} both in terms of natural interaction of spins and loss of coherence due to time-invariant spatial field inhomogeneities.

$$\frac{1}{T_2^*} = \frac{1}{T_2} + \frac{1}{T_{2i}} \tag{2.17}$$

Where T_{2i} is the local field inhomogeneity.

Spatial localisation of MR signals is necessary to generate an image. This is achieved via slice selection, frequency encoding and phase encoding. A combination of a particular shaped RF pulse (e.g. sinc or gaussian) with a linear magnetic field gradient can be used to excite spins in a specific slice. To localise single voxels in this slice, frequency and phase encoding gradients are then applied at the time of the signal acquisition (during readout) along one axis and before the readout starts in varying gradient steps along the other axis respectively. This will produce a linear frequency dependence in the excited spins along the readout axis (conventionally the x-direction) and a phase difference in rotating spins in the phase encoding axis (conventionally along the y-direction). The frequency and phase difference of the spins will then be dependent on their respective positions along the two axis. The process is repeated with varying gradient strengths (or moments) in order to fill up a raw data matrix (in the frequency-domain), known as k-space. Once the matrix has been filled, a Fourier Transformation (FT) can be performed to generate an image (spatial domain data).

Standard structural MRI makes the use of differences in proton densities as well as the inherent relaxation time differences (T_1, T_2, T_2^*) to generate image contrast. This is achieved by the use of different pulse sequences, which are the protocols that adjust the appropriate timing for application of magnetic field gradients, RF pulses and signal recording. The two simplest imaging sequences for MRI are the gradient echo and the spin echo sequence.

A pulse sequence diagram for a spin echo sequence is displayed on figure 2.7 A. Different lines in the pulse sequence corresponds to an axial slice where slice, phase and readout selections are Z, X and Y directions respectively. At the same time as the slice selection (SS) gradient the 90° RF pulse is applied to excite (select) an imaging slice, which rotates the magnetisation vector into the XY plane. Following slice selection, a phase encoding gradient is applied in a stepped fashion which increases from minus PE to plus max PE with one step for each line of k-space along the phase encode direction (PE). At the same time, an additional gradient is applied along the frequency encode direction (FE) to de-phase the spins and align the start of the echo with edge of k-space. Once de-phasing due to T_2 decay has occurred for half of the echo time (TE/2), a slice selection gradient is applied with a slice selective 180° RF pulse to refocus the spins (e.g.

flip the magnetisation along the X axis). This causes the spins to re-phase and to produce the spin echo signal. A frequency encode gradient is applied during the acquisition of the readout. The time needed for performing all of these executions before the next excitation is the repetition time TR. A spin echo sequence will lead to signal intensity(s) for one voxel as demonstrated by equation 2.18.

$$s = k\rho_p \left(1 - e^{-\frac{TR}{T_1}}\right) e^{-\frac{TE}{T_2}} \tag{2.18}$$

Where k is the field strength, surface coil sensitivity and nuclei specific constant, ρ_p is the proton density and TR and TE are the repetition and echo times respectively.

A gradient echo sequence diagram is shown on the figure 2.7 B. To flip the magnetisation vector into the XY plane, a slice selective RF pulse is applied together with a slice selection gradient. The angle between Z and M is called the flip angle which is typically smaller than 90°. Phase encoding is performed along the y-direction via the application of a phase encode gradient. As mentioned above phase encode gradients are increased in a stepwise fashion at each TR to fill in each line of k-space. A negative step of the FE gradient is used to re-phase spins which were de-phased during slice section. A gradient echo is generated after the application of a positive gradient along the x-direction which causes re-phasing of spins. The signal equation for gradient echo sequences (equation 2.19) is similar to the spin echo equation with two differences: T2* replaces T2 as de-phasing due to field inhomogeneities are not re-phased and normally a less than 90° flip angle will be used.

$$S = k\rho_p(\sin\alpha e^{\frac{-TE}{T_2^*}}) \frac{\left(1-e^{-\frac{TR}{T_1}}\right)}{(1-\cos\alpha e^{-\frac{TR}{T_1}})} \tag{2.19}$$

Where $\boldsymbol{\alpha}$ is the flip angle

Appropriate selection of TR and TE influences the signal contrast on spin echo images while for gradient echo images suitable TR, TE, flip angles need to be selected. In order to increase the intrinsic contrast of tissues, contrast agents can be used which are classified as T_1 or T_2/T_2* contrast agents depending on the relaxation mechanism they primarily influence. Gadolinium and manganese are the most frequently used T_1 contrast agents as they reduce spin-lattice relaxation times via chemical exchange between water molecules surrounding the ion and water molecules in the tissue. SPIONs are the main T_2/T_2* contrast agents, which reduce the spin-spin relaxation time due to the marked magnetic field inhomogeneities produced by them. The next section of this chapter will focus on the hardware required to produce images using MRI.

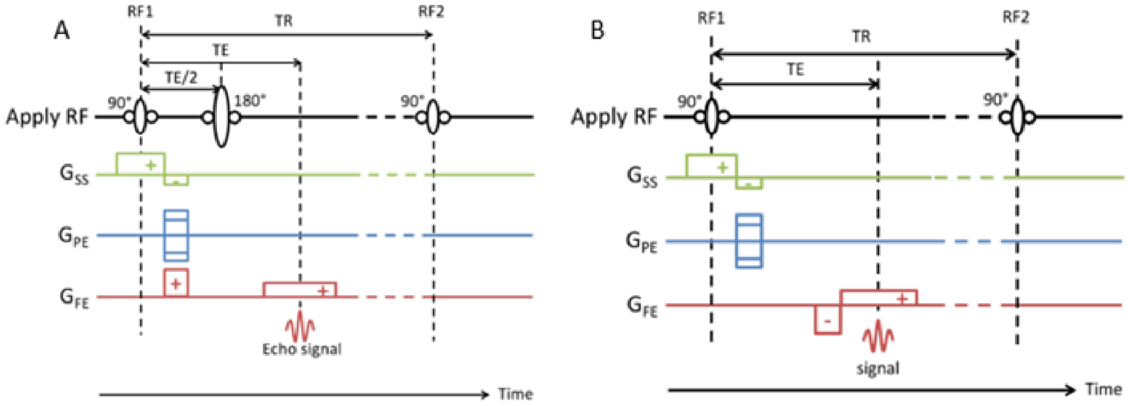

Figure 2.7 – Simplified graphical representation of standard MRI pulse sequences. (A) The spin-echo pulse sequence. (B) The gradient echo pulse sequence. Figure adopted from[144]

2.3.2 MRI hardware

The images in MRI scanner are produced based on the combination of a static magnetic field, switchable magnetic gradient fields, an RF transmitter, and an RF detector (which can be the same equipment), a computer system for image reconstruction and signal digitisation hardware, post-processing, and data storage. The static magnetic field is in general very strong (0.2–9.4 T, for humans [usually 1.5-3T clinically]) and produces the macroscopic spin polarisation. The polarisation of the spins can be manipulated with RF pulses and encoded using gradient magnetic fields.The main components are demonstrated in figure 2.8 and described in more detail below.

1. Super conducting magnet:

High static magnetic fields (0.2–9.4 T, usually 1.5–3 T in clinical applications) with sufficient homogeneity can be achieved with the use of large electric currents in a coil. To be able to use large electric currents without prohibitive losses due to heating, the resistance of the coil has to be minimised. This can be achieved using superconducting materials such as niobium–titanium. If niobium–titanium is placed in liquid helium at 4.2 K ≈ −269 °C the material becomes superconducting (i.e. zero resistance). For some superconducting magnets used in MRI there is resultant boil-off and the need for periodic helium refilling, which contributes to the relatively high operational costs of MRI. Modern MR magnets are equipped with so-called cold-head systems. As the boiled helium gas rises, it re-condenses on the surface of a cold finger and goes back to the system as liquid. This reduces the net boil-off of the helium gas and the costs associated with helium refills.

2. Gradient Coils

Gradient coils are constructed to deliver a linear variation of magnetic field along three dimensions inside the MRI bore. To deliver precise spatial resolution, MR imaging requires precise control of the currents in the gradient coils. One of the most prevalent sources of acoustic noise in MRI is the fast switching of current in the gradient coils. Gradient amplifiers are an important component to reach the required current amplitudes and gradient specs. Section 2.3.3 of this chapter will provide more detailed explanation of gradient coil components and design.

3. RF coil

RF coils can be classified in three main categories: transmit coils; receive coils; and transmit/receive coils. Excitation of the spins is performed using transmit coils and the generated signal is acquired using the receive coils. Some RF coils can deliver both tasks, by transmitting the RF pulse first and then receiving the signal from the subject. To produce more sensitivity and more signal to noise ratio (SNR), sometimes local surface coils are used directly proximal to the organ being imaged which comes with the cost of reduced volume coverage. However, modern phased array coils are designed to produce both good sensitivity and adequate volume coverage. Post processing of reconstructed images will then be employed to combine high SNR images that were acquired from local regions into an image with the desired volume coverage. The use of powerful RF amplifiers is needed to produce the signal in the transmit chain and very sensitive pre-amplifiers are required thereafter to amplify the weak MR signal from the receiver coils in the receive chain. In addition, RF coils have to be tuned to the appropriate Larmor frequency of protons.

4. Magnetic shielding and shimming

In order to produce highly homogenous main magnetic field and detect the weak and sensitive RF signals, a completely magnetic and RF shielded room is required. The RF-shielding is achieved with a so-called Faraday cage. All walls, the ceiling and the floor are made from sheet metal. The magnet itself is shielded in order to facilitate a sharper spatial drop off of the external, fringe magnetic field. Traditional high-field scanners (e.g. 9.4 T) magnet room has an inner chamber that is constructed using soft iron (passive shielding). Modern clinical magnets however are made from two counter-wound coils, which produce the desired magnetic field inside the magnet. However, outside the magnet these coils work against each other and therefore the fringe field decreases over a short distance (active shielding). Actively shielded magnets have the considerable advantage of easier housing requirements in turn saving installation costs.

In addition to external interference, the homogeneous magnetic field inside the magnets bore is disturbed by the patient. To compensate for interference produced by the patient, it is possible to use a separate set of gradient coils which are integrated inside the scanner. These coils have the ability to create an opposing magnetic field which compensates for the inhomogeneities caused by the patient. This process is called “shimming”. Modern MRI systems automatically perform shimming before every measurement.

To control an MRI scanner additional electronic equipment are needed. The selection of a specific imaging pulse sequence and manipulating the imaging parameters is performed using a host computer. The shim controller is used to set currents needed for the active shim coils at the start of an imaging session. An RF amplifier amplifies the waves produced by the RF waveform generator (RF frequency unit) and sends it to the RF coil via a transmit/receive switch. Gradient commands from the communications processor will be translated into particular gradient waveform, amplified and applied to the gradient coils. The induced current in the RF coil is amplified by the RF pre-amplifier and converted into a digitised signal in the receiver unit at a certain time after the RF excitation is applied. All of the procedures stated above need to be executed at precise time points that are controlled by the timing processor. In order to produce an image, the digitised time domain data is sent to the image processor unit which carries out a Fourier transformation. These components are shown in figure 2.7.

In chapters 5 and 6 of this thesis, magnetic resonance targeting of magnetic seeds is investigated using a MRI scanner. The main component of the MRI system which is used in magnetic resonance targeting is the imaging gradient coil which produces the actuation force on the seeds. As such, the next section will introduce the basic concepts relevant to the design of gradient coils for imaging systems.

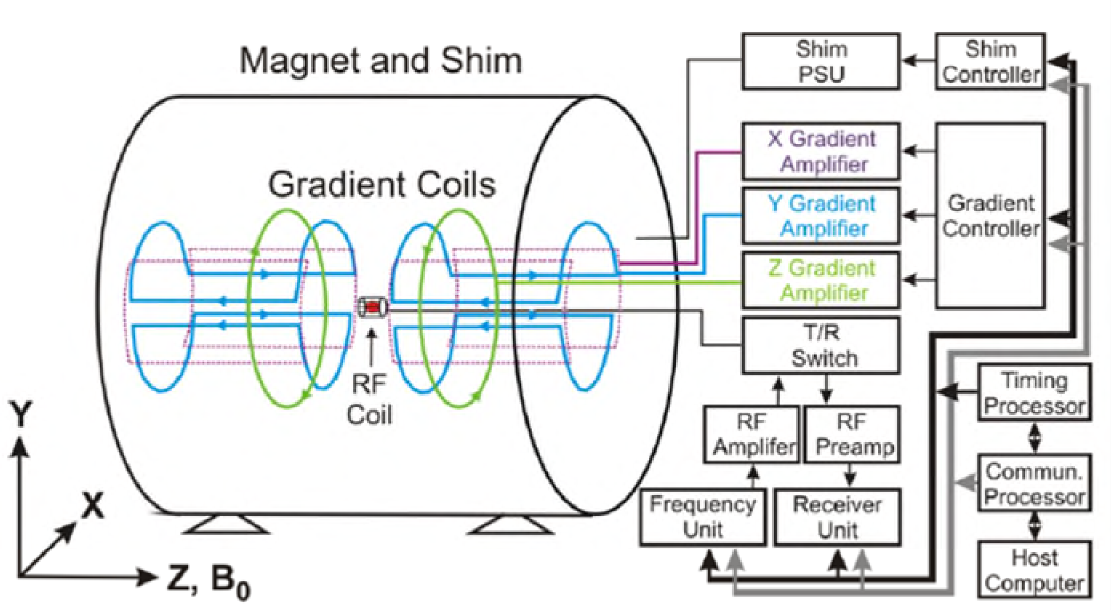

Figure 2.8- Schematic of an MRI scanner. The superconducting magnet and permanent shims are indicated by the outer cylinder. Gradient coils consist of two Golay coils for X and Y gradients and a Maxwell pair for Z gradients. Resistive shim coils are not drawn on the picture although their shim power supply unit (PSU) and control is indicated. A host computer provides an interface to prepare imaging sequences. Commands are sent via the communications processor to subunits. The gradient controller produces a gradient waveform which is amplified by gradient amplifiers. The frequency unit produces radio frequency waveforms which are amplified by the RF amplifier. An RF coil picks up induced currents from exited spins in the specimen (red sphere) which are amplified by the Preamps and digitised in the Receiver unit. The timing processer ensures accurate timing and synchronisation of all sub systems. Following the standard convention the positive Z axis points to the front of the scanner (right side of the image) with B_0 parallel to Z. T/R: transmit/receive, communication. Figure adopted from[145].

2.3.3 Gradient coil design overview

Three orthogonal gradient coils are required to generate a linear variation of the z-component of the magnetic field along the Cartesian axes x, y, and z, where Gx and Gy are referred to as transverse gradients, and Gz is the longitudinal gradient (Fig. 2.9 A). Gradients are produced by passing current, I, through wire coils arranged on a cylindrical surface and gradient strength is measured in Tm^{-1} or $G\ cm^{-1}$. In order to be able to switch the magnetic field rapidly in a gradient coil system, the amount of stored magnetic energy needs to be minimised. This is achieved by minimising the inductance, L of the coil. To minimise power dissipation it is also crucial to keep the resistance of the coil, R as small as possible. In addition, to produce minimal eddy currents it is important to reduce the interaction of the gradient coils with the other conducting materials. Achievement of these requirements generally needs some compromise. For example, increasing the volume over which the gradient is homogenous increases the stored magnetic energy and consequently the inductance.

The strength of the magnetic field gradient produced by a gradient coil is directly proportional to the current which it carries (equation 2.20).

$$G = \eta I \qquad 2.20$$

Where η is known as the gradient coil efficiency and is usually defined as the field gradient strength at the origin per unit current ($T\ m^{-1}\ A^{-1}$) and G and I are the gradient strength and current respectively. A gradient coil with a high efficiency will produce a large gradient per unit current. The coil efficiency is in general affected mostly by its geometry: the smaller the radius, the more efficient the coil is. In addition, the inductance of a cylindrical gradient coil at fixed efficiency is proportional to the fifth power of the coil radius. For this reason, it is important to keep coils as small as possible.

To date, much research has focused on improving the performance of gradient coils. The reported design methods can be divided into two types: discrete wire techniques and current density techniques[146]. Discrete wire techniques are based on the optimization of the geometry (size/position) of independent current loops to produce a required magnetic field. The most basic examples of the discrete wire techniques are the Maxwell and the Golay coil designs.

In all MR scanners the z-gradient is produced using two coils carrying current in opposite directions; which is known as a Maxwell coil configuration (Fig 2.9 B). These coils are separated from each other by a distance of $\sqrt{3}$ of the hoop radius, R, (d= $\sqrt{3}$R). This distance prevents the undesirable spherical harmonic terms that produce fields varying fields. Maxwell coils produce a field that is zero at the isocenter but increases incrementally in both the +z and -z directions. When this is added to the constant (B_0) field, the result is a linearly increasing gradient along the z-axis. The design for transverse gradients used in cylindrical MR magnets is based on a "double-saddle" coil configuration which is known as ‘’Golay coil design’’ (Fig 2.9 C). The simplest form of Golay coil is made of 4 inner and 4 outer arcs on the surface of a cylinder connected by 8 straight wires which are parallel to the z-axis. The current that runs through the inner arcs are primarily responsible for generating the required gradient, while the straight wires parallel to the z-axis perform as return pathways for current and do not contribute to the gradient field. The Golay coil, which includes two pairs of arcs with radius R and geometry parameter $\varphi = 120°$, a = 0.78R, and b = 5.13a, generates a Y-gradient magnetic field with a deviation less than 5%, in a sphere of radius 0.4R. The position of the arcs and the angle they subtend are selected in a way to avoid undesirable spherical harmonics in the field expansion. The gradient linearity can be improved using various optimisation techniques[147,148].

The current density techniques calculate a continuous current distribution which needs to be approximated by discrete wires or current paths. In order to determine the current density distribution a number of optimisation methods have been developed. These include the target field method[149,150] and the stream function method[151,152]. Figures 2.9 D and E show the gradient coils designed by a stream function method for longitudinal gradient coils and transverse gradient coils, respectively[150]. The differences in winding shape between the discrete and continuous wire techniques can easily be noticed. While the current density technique is successful in designing the MRI gradient coils, it also has some limitations. Firstly, the current distribution derived by these methods is approximated by discrete current paths or wires. If the number of wires is small, the approximation to the current distribution is poor, which results in deviation of the calculated magnetic fields. Secondly, return paths must be produced to assure that equal amounts of current flow in all paths. The return currents in these wires generate a longer path for the current-carrying surface and consequently a higher inductance. Thirdly, the complexity of the configuration increases the difficulty in making gradient coils for microscale MRI.

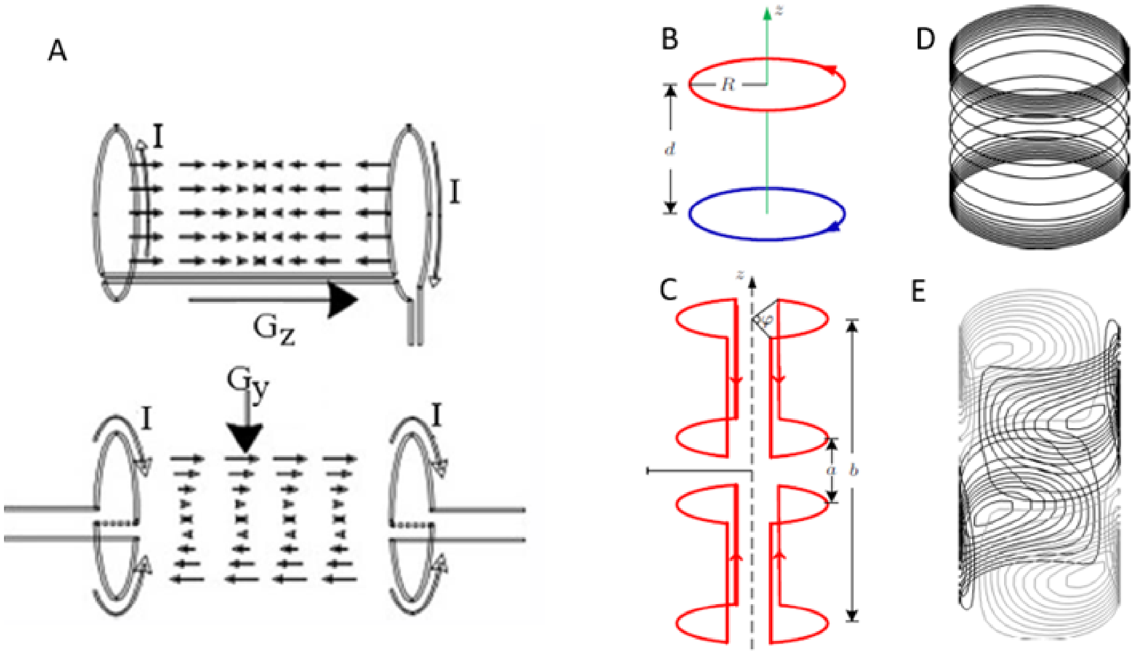

Figure 2.9- Gradient coil designs for MRI. (A) Gz produces a variation of z-component of the magnetic field along the z axis (Upper panel). Gy produces a variation of z-component of the magnetic field along the y axis (Lowe panel). (B) The Maxwell coil design (discrete wire coil). Currents running on opposite directions in the two coils. (C) The Golay coil design (discrete wire coil) which consists of 8 arcs on the surface of a cylinder. (D) A current density Z-gradient coil designed by stream function method. (E) A current density Y-gradient coil designed by stream function method. Figures adopted from[146] and [150] .

In order to be able to produce high amplitude gradients, temperature characterisation and management of the coil is of primary importance. The heat produced by the coil is mostly caused by eddy currents and resistive heating as current is passed through the imaging gradients. For intense imaging applications, large driving voltages and currents are delivered from the gradient amplifier to the gradient coil. As a result of high power amplitudes, intense gradient heat is created reaching temperature of 55-60 °C. All modern MRI scanners are equipped with fluid cooling which is accomplished by circulating de-ionised water or an ethylene glycol solution from a heat exchange pump located in the equipment room. The water flows through tubes or channels in close proximity of gradient coils to minimise heating.

When ferromagnetic objects (such as magnetic seeds) are placed inside the bore of the MRI scanner, the homogenous field of the MRI scanner (>1.5T) is large enough to maximise the magnetisation of the objects to the saturation point (M_{sat})[153]. Magnetic resonance targeting (MRT) relies on the ability of the imaging gradients to induce a steering force on the magnetised bodies allowing them to be navigated at any depth within the MRI bore. As the magnetic steering force is dependent on the gradient strength (see section 2.3.4), high amplitude gradients are desirable in MRT. Conventional clinical imaging gradient coils can produce gradient amplitudes of tens of mT/m (<80 mT/m). However, recent advancements has led to bespoke gradient systems which are capable of producing gradient amplitudes up to 300 mT/m[154]. Previous investigations of MRT have used Imaging Gradient Coils (IGCs)[155] or developed a dedicated Magnetic Targeting Coil (MTC)[130,156] inserts that can be inserted and removed from the scanner bore.

The IGC inserts are powered by their own set of amplifiers such that no hardware modification on the clinical scanner are required for producing magnetic gradients at least ten times those generated by conventional IGCs of clinical scanners[157]. Increasing the gradient magnitude leads to significant decrease of the duty cycle (i.e. ON/OFF operation) to maintain the internal temperature within operational limits[157]. However, reduction in duty cycle causes substantial reduction of the effective steering force (section 2.3.4). To overcome the duty cycle issue, MTC systems have been developed in the past that can maintain a 100% duty cycle (continuous gradients) at high gradient magnitudes (hundreds of militesla per metre) at the cost of a much lower slew rate (i.e. gradient ramp per unit time); which hampers the possibility to perform imaging with these coils. As a results, the MTC has to be combined with an IGC to produce closed loop magnetic targeting where the information from imaging is used as feedback to the steering system. Nonetheless, the combination of MTC and IGC inserts will restrict the maximum diameter of the scanner and may limit the regions of the body that could be treated.

Martel et al., have investigated both MTC[130] and IGC[153] systems for magnetic navigation of magnetic particles inside vascular network. The results of their investigations showed that implementing a whole-body clinical IGC or MTC capable of achieving sufficiently high gradients at 100% duty cycle is not a trivial task, due to technological limits[157]. Additionally, the slew rate at such higher gradients can be dangerous for the patient given the fact that the mean threshold levels are 60 T/s for Peripheral Nerve Stimulation (PNS), 90 T/s for peripheral nerve pain, 900 T/s for respiratory system stimulation, and 3600 T/s for cardiac stimulation[158]. At present, the FDA guidelines suggest 0-20 T/s for clinical practices, which limits gradient switching rates to a factor of 3 below the mean PNS level[157]. As a result of these limits, in order to produce high magnetic field gradients (> 400 mT/m) for magnetic targeting applications, the minimum acceptable rise time will be in tens of milliseconds range.

In addition to technological and safety limits, using a system for a prolonged amount of time at maximum power requires careful temperature monitoring and management[159]. Martel et al.[160], have studied the effect of gradient strength and duty cycle on temperature of an IGC system used for magnetic navigation. The results of their study demonstrated a linear relationship between duty cycle and the heating rate constant of the coil (increase in temperature per unit time) while the corresponding relationship was quadratic for gradient strength. These data suggested that it is best to decrease the gradient strength rather than duty cycle if the operator wants to use the coil for a prolonged period.

In chapter 5 of this thesis I introduce magnetic navigation of chrome steel beads (refered to as thermoseeds) in tissue using a preclinical IGC system capable of producing 500 mT/m magnetic gradient strength at 22% duty cycle. In chapter 6, I report production of a preclinical IGC system that can produce the same strength at 100% duty cycle. The effect of duty cycle on movement of thermoseeds is then investigated using the new IGC system and discussed in chapter 6. The next section will introduce the physics behind the magnetic force that is applied on magnetic particles by the MRI system.

2.3.4 Forces applied by MR system on seeds

The thermoseed used in this study is AISI 52100 steel alloy containing carbon and chromium; which exhibit ferromagnetic behaviour. Owing to their high magnetic susceptibility and saturation, these particles have been used in previous investigations of magnetic resonance navigation[153] and tissue penetrating Guass gun[161]. In addition to their effectiveness on force production, the efficacy of steel thermoseeds in magnetic heating has been demonstrated in previous hyperthermia studies[162]. These properties made chrome steel seeds a suitable option to investigate interstitial navigation using the MR system (chapters 5 and 6).

As demonstrated in section 2.2.2, the magnetic steering force acting on a particle is influenced by its magnetic susceptibility, the field strength and the gradients of the field, which can be expressed as shown in equation 2.8. This equation can be simplified for the case of magnetic resonance targeting of seeds since these particles will be fully magnetised due to the strong field of the scanner (equation 2.11). Therefore, for spherical magnetic seeds we can simplify these equations to equation 2.21[63].

$$\boldsymbol{F_m} = NV(M_s.\nabla)\boldsymbol{B} \tag{2.21}$$

Where N is the number of magnetic seeds and M_s is the saturation magnetisation for a magnetic seed. In our proof of principle seed actuation studies, only a single seed was used leading to N=1. Additionally, as the net magnetisation of the seed inside the MRI scanner is mainly along the z-axis, the x and y magnetisation components can be neglected which simplifies equation 2.21 to equation 2.22.

$$[\boldsymbol{F_{m,x}}\ \ \boldsymbol{F_{m,y}}\ \ \boldsymbol{F_{m,z}}]^T = VM_z[\frac{\partial \boldsymbol{B}_x}{\partial z}\ \ \frac{\partial B_y}{\partial z}\ \ \frac{\partial B_z}{\partial z}]^T \tag{2.22}$$

In order to account for the fact that imaging gradients can only be switched on for short times at high amplitudes and are therefore operated in an ON/OFF fashion, an additional scalar is added which is called duty cycle (D_c). This parameter will be discussed more in detail in chapter 6 of this thesis. In my investigations, I have used gradients across all three axis in different experiments which leads to the following equations (2.23-2.25) for x,y and z directions respectively.

$$\boldsymbol{F}_{m,x} = VD_cM_s\frac{\partial B_z}{\partial x} \tag{2.23}$$

$$\boldsymbol{F}_{m,y} = VD_cM_s\frac{\partial B_z}{\partial y} \tag{2.24}$$

$$\boldsymbol{F}_{m,z} = VD_cM_s\frac{\partial B_z}{\partial z} \tag{2.25}$$

Where D_c is the duty cycle of the applied gradients. ($D_c \leq 1$).

As indicated in equations 2.23-2.25, the magnetic force applied on seeds by the MRI gradients is a function of the duty cycle, gradient amplitude, saturation magnetisation and volume of the magnetic seeds. As indicated previously, in chapters 5 and 6 of this thesis these parameters will be individually investigated in order to optimise the applied magnetic force on seeds for tissue penetration. The next section will provide an overview on mechanical properties of tissue and the literature on force magnitudes needed to propel millimetre-sized implants in brain tissue.

2.3.5 Dynamics of interstitial delivery

In order to produce actuation of the magnetic seed in tissue, the magnetic force applied by the MRI system has to overcome the tissue resistance forces applied on the seed. Knowledge of the mechanical resistance of the tissue can thus play a role in determining the minimum dynamic range needed by the magnetic actuation system to produce well controlled, accurate and efficient movements. As such, this section will aim to explore some basic concepts on mechanical properties of human tissues and in particular brain tissue and brain tumours.

In order to gain insight on dynamics of a penetrating seed, it is necessary to separate force data into components from different sources. We define these forces such that the penetration force occurs before puncture of the tissue ($F_{penetration}$) and the friction ($F_{friction}$) occurs after this main puncture when the seed propels through. The penetration force is due to the stiffness of the organ, which is linearly elastic for small deformations in biological tissue[163]. Likewise, friction force is also a function of the internal stiffness of the tissue[164]. Relative stiffness of different materials can be quantified by Young's, or elastic, modulus (E), which describes the amount of force required to deform a substance, with units of force/area (N/m^2) or Pascals. All tissues have distinct intrinsic physical properties, which are important in their structure and function. Figure 2.10 indicates the elastic modulus of different tissue structures in the body. Such distinct mechanical properties[165] are the result of the difference in structural and functional composition and architecture of the extracellular matrix (ECM), the cytoskeleton and tension of the cellular constitutes and fluid dynamics of the overall organisation of the tissue. The stiffest tissues of the body are tooth and bone ($E \geq 10^9$ Pa), muscle tissue is intermediate ($E \geq 10^4$ Pa), and among the softest are lung and brain ($E \leq 4 \times 10^2$ Pa). Brain tumours exhibit a highly variable elastic moduli which could be in the range of 1-100 $\times 10^2$ Pa.

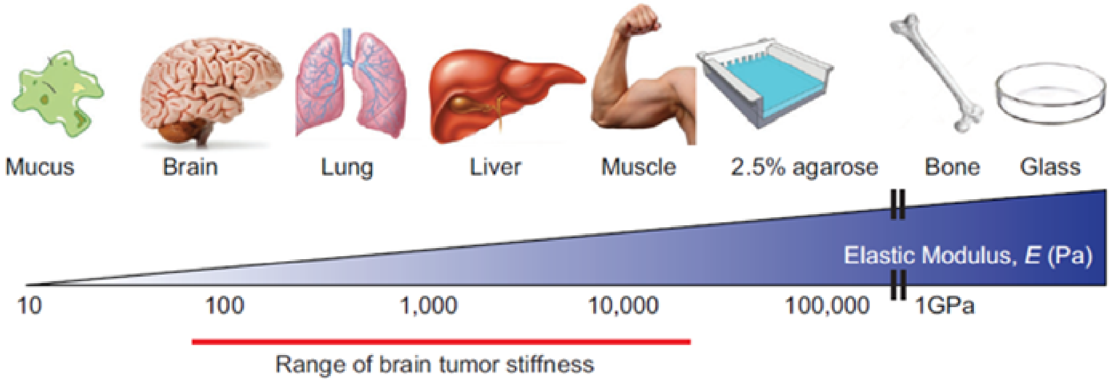

Figure 2.10- Mechanical properties of different biological tissues. Young's or elastic modulus (E) of tissue structures on the same scale with the lowest modulus on the left (mucus) and highest modulus on the right (glass). The range of elastic modulus of different brain tumours are shown by the red line below. Figure adopted from [165].

Previous studies have performed the explicit measurement of different force components for the purpose of penetration of 2.5-mm spherical probe and ventricular catheter probes into human brain tissue[166]. The results of force measurements carried out in these studies indicated that significantly lower force was needed to penetrate a free floating untethered sphere through brain tissue compared with the catheter probe. The data from the 2.5-mm-diameter sphere (Fig 2.11 A) showed an initial steady rise in force as the sphere contacts the cortical surface and begins to displace the superficial brain tissue ($F_{penetration}$). After the sphere traverses this boundary, and is beyond 0.5 cm in depth, the subsequent penetration forces stabilize to a level value ($F_{friction}$) of approximately 8 g +/- 2 g (0.08 +/- 0.02 N). Significant temporary increases in force that occur in a delayed fashion after a sphere has passed well beyond the cortical surface was mentioned to reflect the probe's contact with a subsurface structure that does not consist of grey/white matter. In contrast to the flat force curve observed with sphere propulsion post penetration inside tissue, ventricular catheters experienced increasing resistance force as more of the probe became embedded in the brain tissue (Fig. 2.11 B). The linear increase in the exertion force of the ventricular catheter beyond the penetration point is attributed to the additional drag resistance force which increases constantly as more of the catheter surface comes into contact with the brain tissue. Such experimental observations confirms that a millimetre-sized spherical object could be successfully directed along lengthy trajectories using relatively low magnitude forces in human brain.

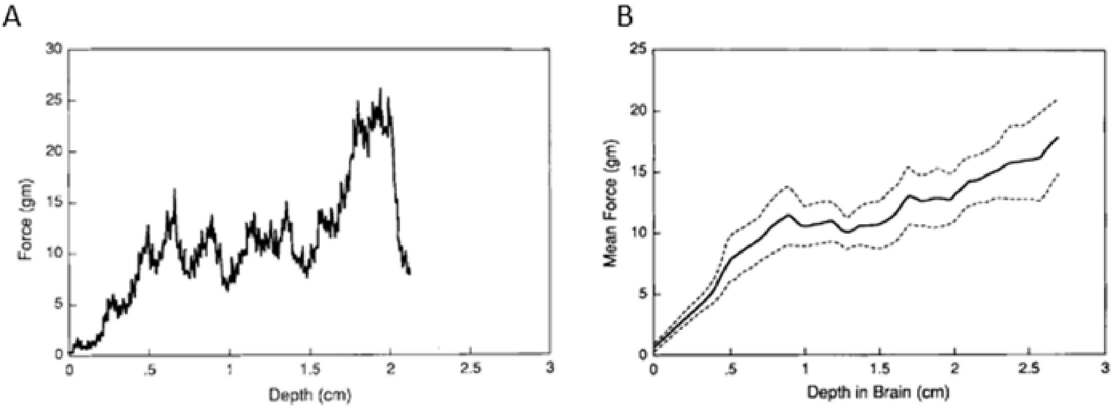

Figure 2.11- Resistive penetration force required to insert surgical probes in brain tissue. (A) Representative plot of the penetration forces encountered as a 2.5-mm-diameter stainless-steel sphere was advanced through the temporal lobe tissues. The forces gradually increased as the sphere penetrated the superficial gray matter of the middle temporal gyrus. Subsequent movement through subcortical tissues was achieved with minimal increases in force. (B) Cumulative data for a surgical catheter drag gathered from ten first-time penetrations with a ventricular shunt. The force measurements were collected at a continuous rate of four samples per second as the 3-mm-diameter SilasticTM catheters were advanced at a constant speed. Mean forces and standard error lines are plotted as a function of the distance traversed from the cortical surface. Figure is adapted from [166].

Another study has aimed to characterise the effect of the probe size, rate of insertion, location of insertion and age of the animal on the penetration force when inserting surgical probes into the brain[167]. The results from this study indicated that frictional forces are significantly affected by the rate of insertion of the probe, size of the probe base and location of insertion (olfactory bulb vs the cortex) while the age of the animal did not have a significant effect on the maximum resistant forces. The parameter which is of particular importance for the methods investigated in this thesis is the size of the implant. As indicated in section 2.3.4, magnetic actuation force applied by the MRI system is proportional to the volume of the magnetic seed. However, the resistance force experienced by the seed is proportional to the surface area of the seed[168] and therefore increasing the seed size will result in more efficient propulsion.

While the studies indicated in this section provide insight into some main physical components, there has been no prior work on the explicit mathematical modelling of different force components for the purpose of magnetic seed insertion into tissue. Accurate modelling of magnetic seed actuation requires extensive knowledge on mechanical properties of different biological tissues and structures; which is beyond the scope of this thesis. However, to move a 3 mm sphere through brain tissue at a rate of 1 cm / 15 seconds, an estimated minimum force of 0.07N has been quoted[168], which requires gradient amplitudes that exceed the strengths of existing MRI gradient coils. To overcome this limitation, previous investigations have aimed to develop penetrating systems (Gauss gun[161] (Fig. 2.12 A) and magnetic hammer[169] (Fig. 2.12 B)) that can be moved in tissue using the gradient amplitudes that existing MRI gradient coils can produce. The magnetic actuation hammer was composed of a steel sphere inside a cylinder with a spring at one end and an impact plate on the other with a pointed tip at the end. The gradients are then applied to push the sphere onto the spring to generate large, pulsed forces on the impact plate when the gradients are switched off. A hammer which was 7.5 mm in diameter, 50 mm long and contained a 5 mm sphere penetrated up to 9 mm into *ex vivo* goat brain using gradients of 23 mT/m. To realise whether MRI could be used for tissue penetration of a single spherical particle, chapters 5 and 6 of this thesis will aim to investigate navigation of magnetic beads using a preclinical MRI system with a clinical end-point in mind.

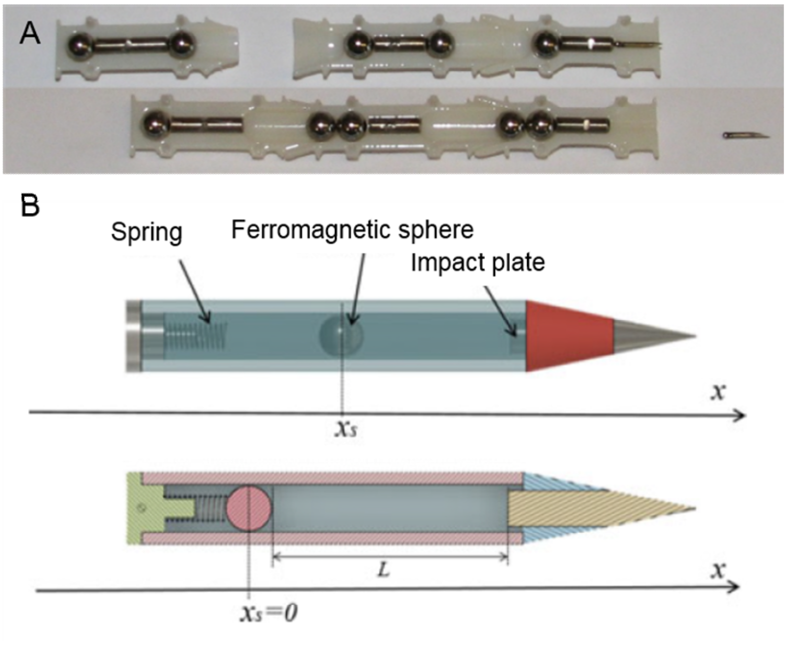

Figure 2.12- The Guass gun and magnetic hammer systems. (A) photo of the cross section of the gauss gun in Becker et al,.[161] showing the positions before and after firing. (B) Schematic of the magnetic actuation hammer from Leclerc et al,[169].

3. Magnetic targeting of SPIONs using a surface permanent magnet

As described in chapter one, external magnetic field sources used for magnetic targeting applications can be classified into two main groups: (i) permanent magnets and (ii) electromagnets. While electromagnets provide control over the applied force, most magnetic targeting studies have utilised permanent magnets for their simplicity and strength. This chapter focuses on using a powerful permanent magnet (disk magnet) to target individual nanoparticles (single magnetic carriers, SMCs) to tumours. A flow phantom setup was first constructed to investigate capturing efficiency of nanoparticles using the disk magnet. Magnetic targeting and imaging of nanoparticles was then investigated in a bilateral tumour model *in vivo*.

3.1 Introduction

One of the current challenges in cancer therapy is delivering a high concentration of drug to the tumour tissue whilst reducing systemic dosing, thereby limiting off-target adverse effects[11,108]. Magnetic nanoparticles, in combination with applied magnetic field gradients, can increase delivery of small molecule drugs[170] and cells[35,36,61,62] to a specific site within the body to enhance their therapeutic effect. Additionally, SPIONs can also act as a magnetic resonance imaging (MRI) contrast agent [34,40,41], enabling non-invasive imaging of particle delivery to the region of interest, as well as hyperthermia cancer therapy[85] or triggering of drug release[171,172], and mechanical rotation to induce cancer cell death[173]. The multiple actions of biocompatible SPIONs means they are well-suited as a bimodal drug delivery and diagnostic imaging agent[174].

As discussed in chapter 1, the efficacy of magnet targeted therapies depend on magnetic content and pharmacokinetic properties of the magnetic particles such as size and surface composition, as well as the magnet design and depth of the targeting region[34,175]. Much of the magnetic drug targeting literature has focused on developing small and surface modified nanoparticles in order to increase blood circulation time, bio-stability and extravasation efficiency of the delivery system[5,12,28,176]. However, an important question is whether the applied magnetic field gradient is sufficient to capture such nanoparticles at the target region. A larger net force can be applied to heavily SPION loaded cells or capsule magnetic carriers (CMCs) over single magnetic carriers (SMCs), leading to greater targeting efficiency due to their larger size and iron content. This creates a significant challenge for magnetic drug targeting using unencapsulated nanoparticles. To this end, I have utilised unencapsulated nanoparticles in this thesis, in order to investigate the targeting efficiency of simple permanent magnets in a more challenging design.

Chertok et al.,[123] have shown that magnetic targeting using an electromagnet could enhance the delivery of unencapsulated nanoparticles to rat brain tumours. However, despite positive preclinical investigations, clinical studies on magnetic drug targeting[11,108] have been limited, mainly due to the poor penetration depth of the magnetic field gradient, resulting in sub-optimal targeting to deeper tissues of the human body. One benefit of electromagnets is their ability to generate gradients to target SPION loaded cells[31,63] and micron sized particles[177] to deeper locations within the body[178]. However, to date there has been no evidence to suggest that electromagnets can exert magnetic forces strong enough to capture sub-micron particles at internal organ targets at the clinical scale. Instead, much of the magnetic targeting literature has focused on using simple permanent magnets[11,35,36,108] as they are cheap, versatile and do not require a power supply, additional cooling or sophisticated control algorithms.

In this chapter I employed a systematic approach to investigate magnetic targeting of unencapsulated nanoparticles using external permanent magnets. I setup a vascular flow phantom to choose an appropriate particle size and characterise the targeting efficiency of a surface disk magnet based on the extent of particle capture at regions of interest around the magnet. I chose to study the 100 nm size since they were previously utilised to deliver anti-cancer medications in clinical trials[11] and the 50 nm particles since I hypothesised that smaller particles may be advantageous due to their reduced rate of uptake by the RES system and their higher chance of extravasation (i.e. the ability of nanoparticles to pass through blood vessel walls into surrounding tissue). I then used a single particle size with the appropriate capture efficiency for *in vivo* magnetic tumour targeting experiments.

The aims of these experiments were:

(i) To investigate the effect of particle size and distance from the magnet on magnetic targeting at physiologically relevant flows.

(ii) To investigate magnetic tumour targeting of unencapsulated nanoparticles using a strong surface magnet.

(iii) Utilising MRI as a non-invasive technique to predict, visualise and quantify nanoparticle delivery to the region of interest within the body.

3.2 Materials and Methods

3.2.1 Disk magnet

A cylindrical neodymium iron boron permanent magnet (1 T residual magnetism, grade N52) with 4.5 cm diameter and 3 cm height was used in this study; which is referred to as the disk magnet thoroughout this thesis. In order to understand the spatial distribution of the magnetic force applied by the disk magnet, I simulated the magnetic flux density map on various planes around the magnet using Opera Cobham simulation software (Oxfordshire, UK). As indicated in section 2.2.2, the magnetic force is dependent on the $(\boldsymbol{B}.\nabla)\boldsymbol{B}$ acting on particles below saturation magnetisation of particles. My investigations indicated that the highest magnetic field gradient is generated proximal to the edge of the magnet. Therefore, I simulated magnetic flux density map around the edge of the magnet in two orthogonal planes (Fig 3.1). These planes are oriented at 30 degrees from the circular face of the magnet where the vascular flow phantom and the subcutaneous tumours were positioned. The orientation of the magnet used for the phantom and *in vivo* experiments are shown in figures 3.1 A and B respectively.

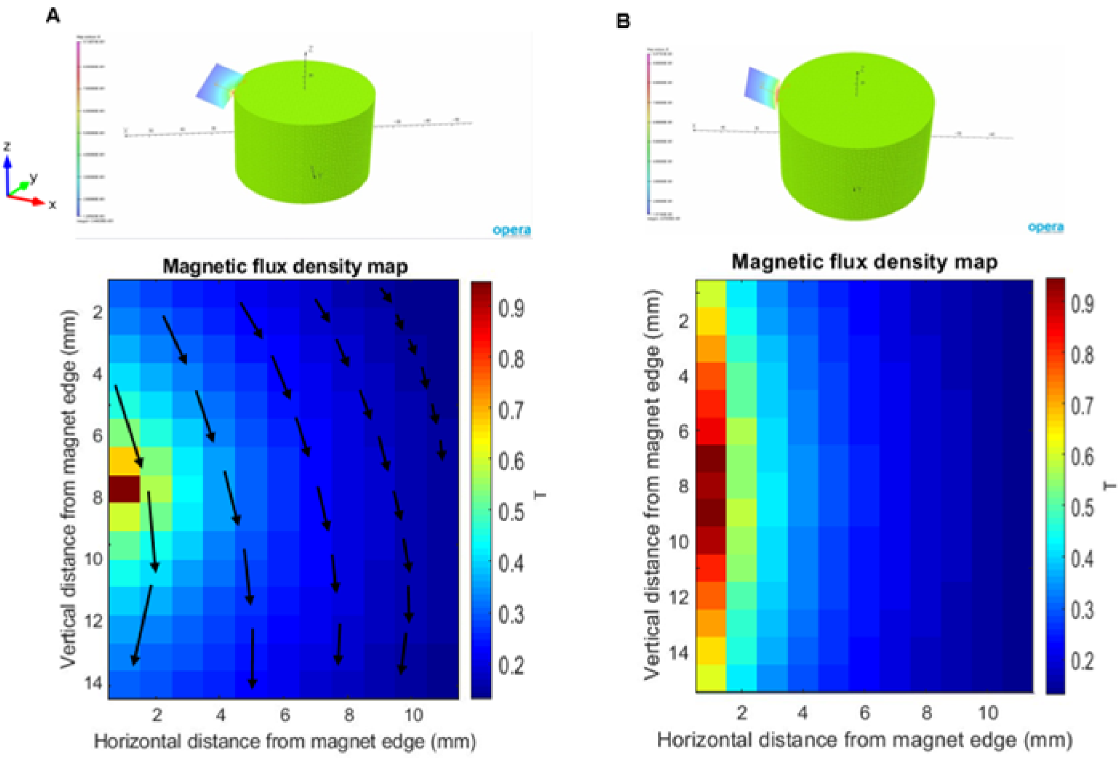

Figure 3.1- Simulation of the magnetic flux density around the disk magnet. (A) Magnetic flux density map around the edge of the magnet 30 degrees wrt the positive x-axis at the xz plane. This orientation of the magnet was used for the phantom experiments. The flux direction is shown. (B) Magnetic flux density map around the edge of the magnet at the orthogonal plane (30 degrees wrt the negative x-axis). This orientation of the magnet was used for the *in vivo* experiments. The flux direction is towards the perpendicular plane.

The $(\boldsymbol{B}.\nabla)\boldsymbol{B}$ magnitude was calculated and plotted using MATLAB 2016a (MathWorks, Inc., Massachusetts, US) to demonstrate the magnitude of the magnetic actuation force applied by the magnet below the saturation magnetisation (Figure 3.2). These data are used to provide insight on magnetic force applied on nanoparticles during flow phantom and *in vivo* experiments (sections 3.3.1, 3.3.2).

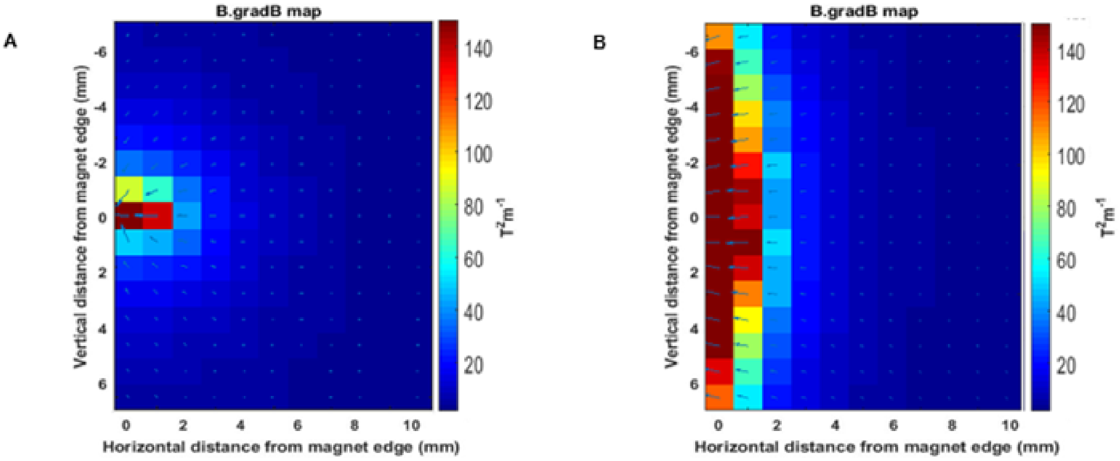

Figure 3.2- Calculation of the B.gradB values around the disk magnet. (A) B.gradB map around the edge of the magnet 30 degrees with respect to the positive x-axis. (B) B.gradB map in the orthogonal plane. The direction of the vector fields are shown on the maps.

3.2.2 Flow phantom simulation of magnetic targeting

Vascular flow phantom:

A phantom flow experiment was used to simulate magnetic targeting of magnetic nanoparticles in a simplified model. A standard configuration consisting of the magnet and a 0.38 mm internal diameter capillary tube (Smiths Medical Ltd, UK) was used. A total mass of 0.4 mg (equivalent to a 20 g mouse injection dose of 20 mg/kg) of fluidMAG-CT particles (Chemicell, Germany, 100 nm and 50 nm diameters with a magnetite core and carboxyl functional group coating) were diluted with 1.5 mL of PBS (average mouse blood volume) and infused into the tube using an infusion pump (PHD 2000 Harvard Apparatus, US). Physiologically relevant capillary blood flow velocities were chosen based on the values used in previous *in vitro* studies[22,179,180] at 5 mms^{-1}, 8 mms^{-1} and 10 mms^{-1} corresponding to flow values of 0.037 mL/min, 0.060 mL/min and 0.075 mL/min respectively. The total infusion volume was kept constant for all experiments. The disk magnet was placed at five distances (0, 3, 6, and 8, 10 mm) from the tube for each flow velocity value.

Quantification using ferrozine assay:

The tubes containing accumulated nanoparticles were flushed with 0.6 M hydrochloric acid and incubated in a heat block at 65 °C for 2 h. 30 µL of pre-made ferrozine reagent was then added to the samples and the absorbance was measured at 570 nm using a benchtop spectrophotometer (Multiskan^{TM} FC microplate photometer, Thermo scientific). The same procedure was carried out for serial dilutions of known amounts of fluidMAG-CT particles to allow calibration. Linear interpolation to serial dilution absorbance results, allowed iron quantification from the absorbance results acquired from the samples. The capturing efficiency for each sample was calculated as the percentage of the captured particles over the total perfused mass of particles.

3.2.3 *In vivo* magnetic targeting and imaging

Magnetic targeting:

All animal studies were approved by the University College London Biological Services Ethical Review Committee and licensed under the UK Home Office regulations and the Guidance for the Operation of Animals (Scientific Procedures) Act 1986 (Home Office, London, UK). Mice (n=6) were subcutaneously injected on each flank with 1 million LS174T colorectal tumour cells (ATCC, CL-188) and monitored every 2 days by visual inspection. Two weeks after cell implantation, anaesthesia was induced and maintained in 1.5-3.0% isoflurane in 1 L/min O_2 and 0.4 mg of 100 nm fluidMAG-CT particles were intravenously injected into the mouse via a tail vein, and the magnet was positioned directly over the surface of one of the bilateral tumours during and for 20 minutes after nanoparticle injection.

MR imaging:

Mice were positioned in a 35 mm Rapid RF coil with temperature monitored and maintained at 37 °C with warm water tubing; respiration rate was monitored at typically 60-80 bpm. T_2-weighted and T_2* map images were acquired before and after nanoparticle administration using respiratory-triggered fast spin echo sequence (TR/TE 1000/9 ms, ETL 4, 20x1 mm thick slices, 1 average, data matrix 256^2, field of view 30 x 30 mm, ≈1 min) and multiple gradient echo sequence (TR 500 ms, 16 echoes 1.51 – 27.25 ms, 2 averages, 256^2, 30 x 30 mm, 5 x 1 mm thick slices) using a 9.4 T Varian Inova scanner (Varian, Santa Clara, CA).

Image analysis:

The T_2^* maps were estimated by mono-exponential fitting of signal decay to each voxel in manually chosen regions of interest (ROIs) using non-linear least squares method in MATLAB. To map the distribution profile of nanoparticle accumulation within tumours, the T_2^* value of line segments located at 1 mm intervals through the tumour were measured for both targeted and non-targeted tumour groups before and after nanoparticle injection (n=6). This was performed between the ranges of 1 to 4 mm within the tumours. Data were analysed with in-house MATLAB code.

3.2.4 Histology

Tumour samples (n=2) were fixed in 4% paraformaldehyde and then processed for histology, embedded in paraffin wax blocks and sectioned in 5 µm slices. Prior to staining, adjacent sections were cleared in xylene and then rehydrated through 100%, 95% and 50% ethanol to distilled water. The sections were then incubated in freshly prepared 5% potassium ferrocyanide (Sigma-Aldrich) solution with 10% hydrochloric acid for 20 minutes, rinsed and then counterstained with 0.1% nuclear fast red solution (Sigma-Aldrich) for 5 minutes. The tumour slices were dehydrated again through 95% and 2 changes of 100% ethanol and cleared in xylene and the coverslip was mounted with DPX (distyrene, plasticiser and xylene, Sigma-Aldrich). Images of the tumour slices were taken using a slide scanner (Nanozoomer, Hamamatsu, Japan).

3.2.5 Direct Iron quantification by ferrozine assay

To validate MR imaging results, iron-oxide accumulation was quantified directly in the *ex vivo* tumour samples. Following on from the *in vivo* targeting experiments, mice were sacrificed and the subcutaneous tumours (n=4) were removed; 2 mL Lysing matrix D tubes containing tissue homogeniser beads were purchased from BP Biomedicals (Santa Ana, California, USA). The tumour samples were placed in the lysing tubes and a high-speed benchtop reciprocating homogeniser (Fastprep-24™ Sample Preparation Instrument, MP Biomedicals) was used to homogenise the tissue samples. 50 mg of each tissue sample was transferred to a 1.5 mL test tube, 100 µL of 0.6 M hydrochloric acid was added to each sample and the samples were incubated in a heat block at 65 °C for 2 h. 30 µL of pre-made ferrozine reagent was then added to the samples and the absorbance was measured at 570 nm using a benchtop spectrophotometer (Multiskan^{TM} FC microplate photometer, Thermo scientific). The same procedure was carried out for serial dilutions of known amounts of fluidMAG-CT particles to allow calibration.

3.3 Results

3.3.1 The effect of nanoparticle size and distance on magnetic targeting

The ability to capture individual magnetic particles, and as such a therapy, depends on magnetic force, which is contingent on design, the distance between the magnet and the particle, and the size and magnetic properties of the particle. To investigate these individually, I used a flow phantom to magnetically capture nanoparticles at various distances, flow velocities, and sizes (50 and 100 nm) using the disk magnet. The following sections will aim to present the results on investigations of (i) the effect of size of the nanoparticles, and (ii) the effect of distance from the magnet (B.gradB) on magnetic capturing efficiency of nanoparticles whilst flowing with physiologically relevant flow velocities.

3.3.1.1 Effect of nanoparticle size

I observed that nanoparticles were readily attracted to the capillary tube wall at clinically relevant tumour flow velocities (Fig. 3.3 A). Detectable amount of 100 nm particles was observed attached to the tube wall at different distances from the magnet (Fig. 3.3 B). Conversely, when repeated with 50 nm-sized particles, fewer particles were captured in all cases compared with 100 nm-sized particles. Magnetic capturing of 50 nm particles was only possible up to 6 mm away from the magnet at 5 mms^{-1} velocity (Fig. 3.3 C). The maximum capturing distance was reduced to 3 mm at 8 mms^{-1} (Fig. 3.3 D) and to 0 mm at 10 mms^{-1} (Fig. 3.3 E). Compared with the 100 nm particles, I observed an average of 2-fold lower nanoparticle capturing at 0 mm distance across the three flow velocities (n=3, *P ≤ 0.05). I also observed a significant difference between capturing efficiency of 100 nm and 50 nm particles at 6 mm distance when flowing at the lowest flow (5 mms^{-1}) and at 0 mm distance when flowing at 8 and 10 mms^{1} (n=3, *P ≤ 0.05). From these results, it was determined that 100 nm particles were more suitable for *in vivo* magnetic targeting experiments.

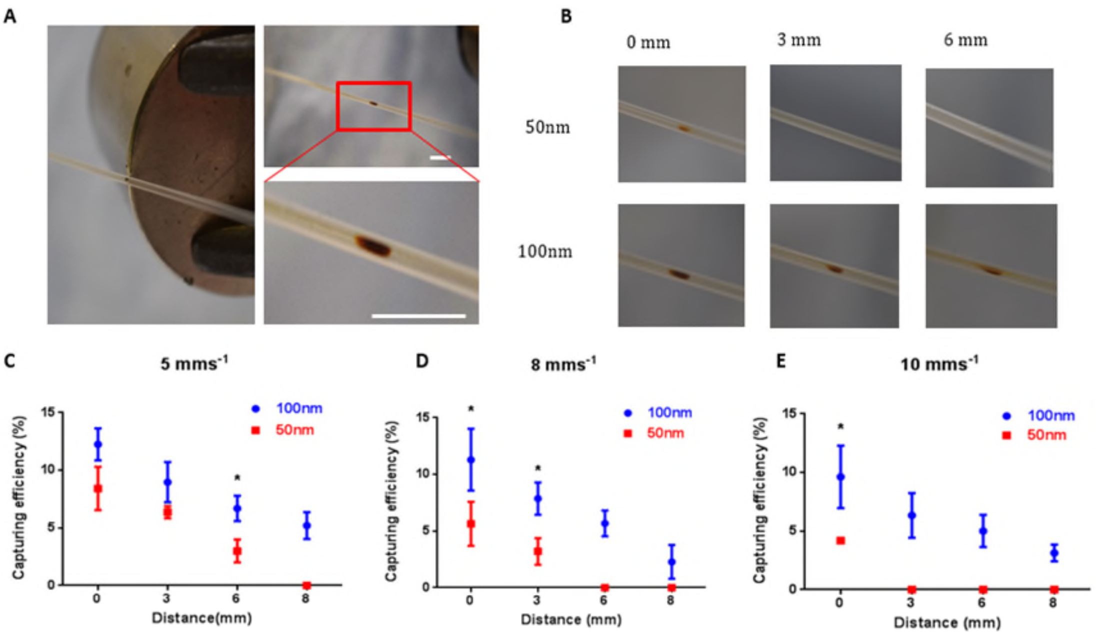

Figure 3.3- Magnetic targeting of nanoparticles in a flow phantom - Effect of particle size (A) Experimental set up showing tubing with particles flowing past the disk permanent magnet at flow rate of 8 mms^{-1}. Accumulation of nanoparticles clearly visible on internal tube wall, scale bars 5 mm. (B) Accumulation of 50 and 100 nm particles directly after magnet removal for three magnet distances at flow rate of 10 mms^{-1}. Capturing efficiency of accumulated particles (100 nm or 50 nm-size) at (C) 5 mms^{-1}, (D) 8 mms^{-1}, and (E) 10 mms^{-1} flow velocities. Capturing efficiency values were measured using quantitative ferrozine assay (*P<0.05, n=3). Data shown as mean ± SD.

3.3.1.2 Effect of distance from magnetic source

Magnetic retention of nanoparticles was monitored at various distances (0, 3, 6, 8, 10 mm) from the edge of the disk magnet. The B.gradB topography produced by the magnet at these distances is shown in figure 3.4 A (dashed lines). I observed that magnetic targeting decreased with increasing distance from magnet edge. Detectable amount of nanoparticles were only observed up to a maximum distance of 8 mm from the magnet (B.gradB of 3 T^2m^{-1}) at all three flow velocities. The capturing efficiencies at 5 mms^{-1} flow velocity corresponding to magnet distances of 0, 3, 6 and 8 mm were 12.3 ± 0.6%, 8.9 ± 0.8%, 6.7 ± 0.5% and 5.3 ± 0.5%, respectively (Fig. 3.4 B). Nanoparticle capturing at 0 mm distance was observed to be 2.4-fold higher (n=3, **P ≤ 0.025) than 8 mm distance at the same flow velocity. Corresponding differences were 5.1-fold (n=3, **P ≤ 0.025) and 3.1-fold (n=3, *P ≤ 0.05) at 8 mms^{-1} and 10 mms^{-1} flow velocities respectively. In a similar fashion, magnetic capturing decreased with increasing flow velocity. Taking 0 mm distance as the example, capturing efficiency values were observed to be 12.3 ± 0.6%, 11.3 ± 1.3% and 9.6 ± 1.3% for flow velocities of 5, 8 and 10 mms^{-1} respectively. From these results, it was concluded that our disk permanent magnet was suitable for *in vivo* magnetic targeting of 100 nm particles as 8 mm distance or less would provide total coverage of a subcutaneous tumour.

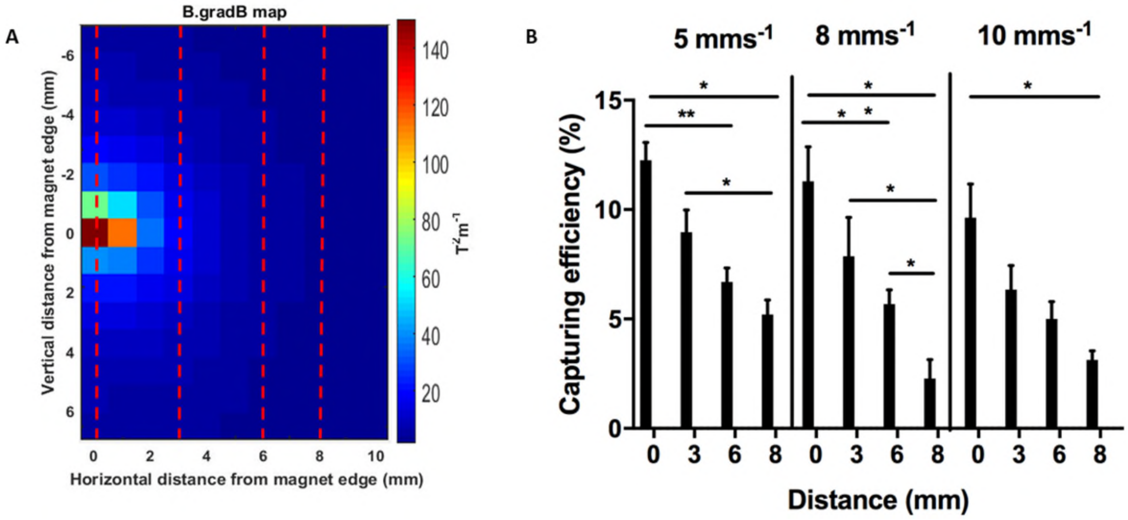

Figure 3.4- Magnetic targeting of SPIONs in a flow phantom - Effect of magnet distance. (A) B.gradB topography around the magnet edge in the same plane as the vascular tube. (B) Capturing efficiency of 100 nm particles at three flow velocities and four distances from the magnet measured using quantitative ferrozine assay (**P*<0.05, n=3). Data shown as mean ± SD.

3.3.2 *In vivo* magnetic targeting and imaging of tumours

Following on from the *in vitro* phantom experiments, I performed *in vivo* experiments to investigate magnetic targeting of individual nanoparticles to subcutaneous tumours using the disk magnet. As these particles act as an MRI contrast agent, quantitative MRI was used to detect and quantify particle delivery and distribution. I observed marked magnetic targeting of nanoparticles to tumours on the MR images as patches of hypointense regions (decreased T_2*) within the targeted tumours (circled, Fig. 3.5 A). Quantitative T_2* maps (overlaid onto anatomical T_2-weighted images, Fig. 3.5 B) give a clear indication as to the extent and spatial distribution of nanoparticle accumulation in the targeted tumour. These maps were acquired by mono-exponential fitting of the signal decay at different TEs to calculate T_2* of each voxel in the chosen regions of interest (ROIs) (Fig. 3.5 C). T_2* was markedly reduced in the targeted tumours (n=6, $*P \leq 0.05$, Fig. 3.5 D) when using the disk magnet, while the non-targeted tumours did not change. To validate the MR imaging results, a quantitative ferrozine assay measurement was carried out on homogenised tumour tissues. The assay showed a higher concentration of nanoparticles in the targeted tumour tissue compared to non-targeted controls (n=4, $*P \leq 0.05$, Fig. 3.5 E). The Perl's Prussian blue histology indicated the presence of the accumulated iron-oxide nanoparticles (blue spots) in targeted tumour slices (Fig. 3.5 F,G).

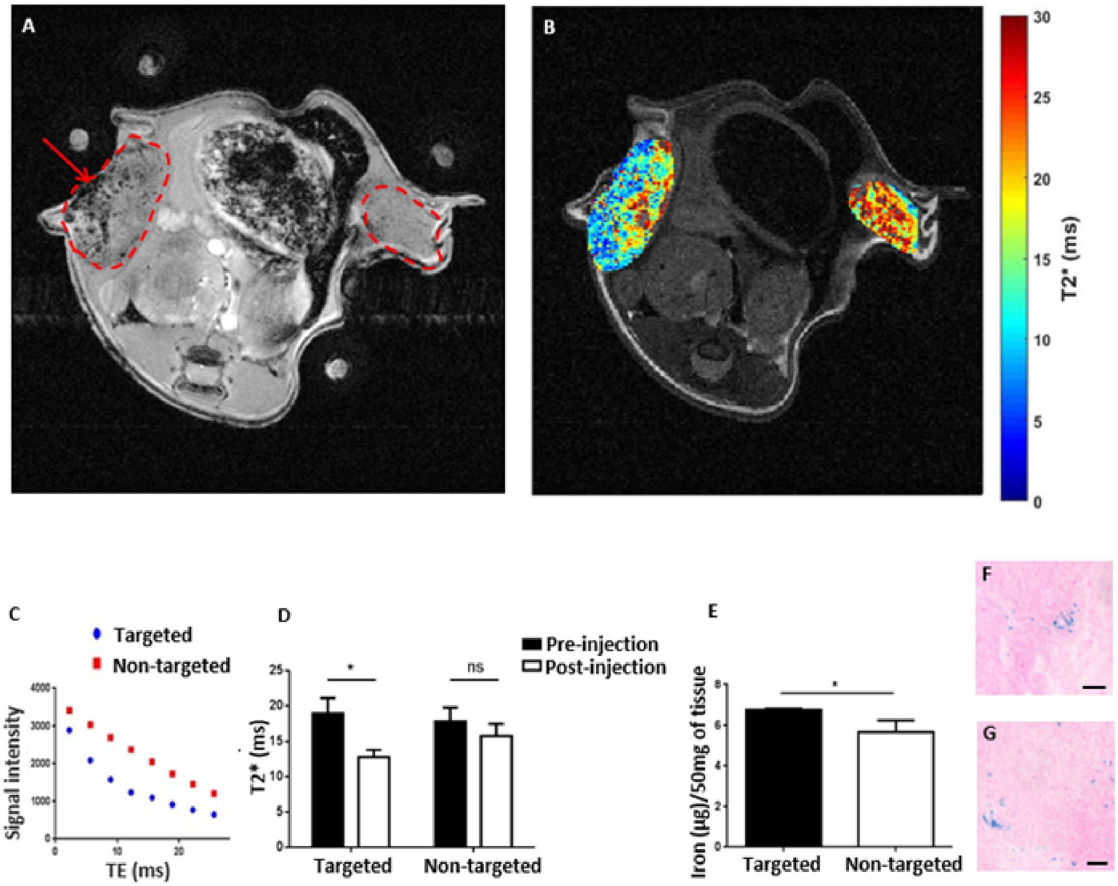

Figure 3.5- *In vivo* magnetic targeting of nanoparticles using the disk magnet. (A) T_2*-weighted MR image showing bilateral subcutaneous tumours (circled) with hypointense regions in tumour exposed to external magnetic field (left) during intravenous nanoparticle injection; homogenous MR signal in non-targeted tumour (right). (B) T_2* map of same tumours overlaid on T_2-weighted image indicating spatial distribution of T_2* reduction as a consequence of nanoparticle accumulation. (C) Signal intensities at different TE for the magnetically targeted and non-targeted tumours fitted to the mono-exponential decay model to calculated T_2^* of the drawn ROI. (D) *In vivo* magnetic targeting using the disk magnet design significantly reduces mean T_2* after injection of nanoparticles (**P*<0.05, n=6). (E) Magnetic targeting significantly increases iron measurement in the tumour after injection of nanoparticles indicated by quantitative ferrozine assay (**P*<0.05, n=4). (F) Perl's Prussian blue staining on histological slices of tumours exposed to magnetic field post nanoparticle intravenous injection. Scale bar 100 µm. (G) Perl's Prussian blue staining on a different tumour slice. Data shown as mean ± SEM.

In order to acquire more insight into the accumulation profile of the accumulated nanoparticles, I investigated the spatial distribution of hypointense regions in T_2* weighted images of targeted tumours. In most tumours, I observed more T_2* hypointense regions in locations closest to the magnet (Figure 3.6 A, red arrow), which were not present prior to injection of nanoparticles and magnetic targeting (Figure 3.6 B). Prussian blue staining of the *ex vivo* tissue sample provided further confirmation of iron in the proximal region of the tumour (Figure 3.6 C). I quantified spatial distribution of nanoparticles by measuring the T_2* values across tumours (1 to 4 mm within each tumour) before and after nanoparticle administration. I observed an increasing trend in post-injection T_2* of the targeted tumours. The slope of the post-injection T_2* was different from zero (n=6, *P ≤ 0.05, Figure 3.6 D, red line) and as expected, the further away from the magnet, the less targeting was observed. Among the four investigated line segments across the tumour, I only observed a difference between the pre and post injection T_2* values at 1 mm depth (n=6, *P ≤ 0.05). I further calculated the percentage reduction in T_2* after particle administration and targeting (Fig. 3.6 E). A difference of 24.5 ± 9.36% was observed in percentage reduction of post magnetic targeting T_2* between 1 mm and 4 mm across the tumours. The approximate position of the tumour within the spatial topography of the B.gradB magnitude indicates the sharp decline in strength of the magnetic force applied at deeper locations within the tumour (Fig. 3.6 F).

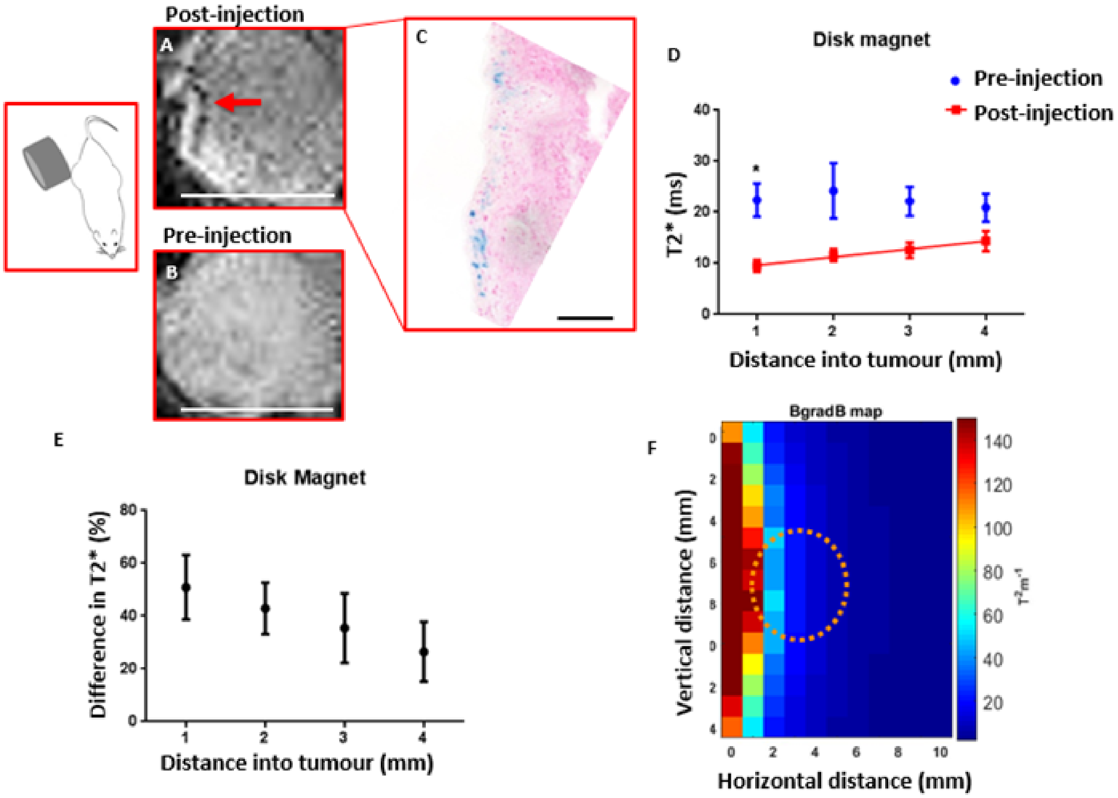

Figure 3.6- Tumour distribution of magnetic targeting. (A) Subcutaneous tumour after nanoparticle injection and targeting; Scale bar 5 mm (B) same tumour prior to magnetic targeting. (C) Nanoparticle accumulation confirmed by Prussian blue histology. Scale bar 100 µm. (D) The spatial T_2* distribution of the magnetically targeted tumours pre and post nanoparticle injection (**P*<0.05, n=6). (E) Percentage reduction in T_2* between pre and post nanoparticle injection for magnetically targeted tumours (n=6). (F) B.gradB topography of the disk magnet with the approximate tumour position within the map. Data shown as mean ± SEM.

3.4 Discussion

Magnetic targeting of drug labeled SPIONs offers a promising method to increase the delivery of chemotherapeutic agents to tumours whilst reducing the systemic dosing of the drug. However, it is unclear whether it will be possible to target SPIONs to tissues deeper in human body when conventional permanent magnets are used for targeting[5,11]. In this chapter, the ability of a conventional permanent magnet to target unencapsulated nanoparticles was assessed in a variety of conditions. There are four major findings from this study:

- The disk magnet can target commercially available 100 nm particles up to a distance of 8 mm away from the magnet (B.gradB value of 3 T^2/m).
- T_2* weighted images can be used to visualise and quantify the regional distribution of nanoparticle accumulation within the tumour tissue.
- The disk magnet enhances delivery of 100 nm particles to subcutaneous tumours *in vivo*.
- Nanoparticle distribution is more prevalent at superficial tumour locations when a conventional surface magnet is used for targeting.

3.4.1 Flow phantom experiments

Although simple flow phantom experiments do not accurately reproduce the *in vivo* situation, they adequately represent the interplay between the magnetic and hydrodynamic components of magnetic targeting. There has been a wealth of previous reports on the use of flow phantom experiments[22,179,180] and theoretical simulations of magnetic targeting using a variety of particle sizes and magnetic designs[181,182]. Lunnoo et al.,[181] investigated capturing efficiency of 100 nm particles in a mimicked pulsatile flow simulation. They observed low capturing efficiencies (below 10%) at B.gradB values of about 90 T^2/m, and similar flow velocity ranges to the flow phantom experiments in this study. The results of our experiments were in close agreement with these theoretical simulations. It should be noted that only a small fraction of these particles can be captured when they flow past the permanent magnet in a single pass. However, in the *in vivo* situation, the particles will be passing the magnet multiple times, as they circulate in the bloodstream before being captured by the reticuloendothelial system (RES) (see section 1.1.1), which increases the chance of targeting.

3.4.2 Effect of particle size and magnet distance on magnetic targeting

I used the phantom flow experiments to gain insight into the effect of particle size and magnet distance on magnetic capturing of nanoparticles whilst in physiologically relevant flow velocities. Carriers with d > 100 nm are eliminated faster (than d < 100 nm) from the cardiovascular system by the liver and spleen[10], whereas smaller particles (d < 10 nm) are cleared by renal clearance[10]. Therefore, carrier sizes of 10–100 nm in diameter are more appropriate for *in vivo* delivery of therapeutic agents[10]. Here, I have utilised magnetic particles with 50 nm diameter (magnetite core < 30 nm) and 100 nm diameter (magnetite core > 50 nm)[183]. I observed a marked difference in capturing efficiency between the two particle sizes at all flow velocity and magnet distances suggesting that 100 nm particles are far more suitable for *in vivo* targeting.

In addition to particle size, another aim of these experiments was to identify the effective targeting distance of nanoparticles by the disk magnet. The results indicated that the disk magnet was suitable for magnetic capturing of 100 nm particles up to a maximum distance of 8 mm at capillary flow velocity of 10 mm/s. The corresponding magnetic field gradient and B.gradB values at this distance are 21 T/m and 3 $T^{2/}$m respectively. These observations were consistent with the results of the flow phantom experiments carried out by Takeda's group[127] where they concluded that a minimum gradient of 20-50 T/m is needed to capture 100 nm particles at flow velocities of even as high as 100 mm/s.

3.4.3 *In vivo* magnetic targeting and imaging

I investigated *in vivo* magnetic targeting of 100 nm particles to subcutaneous tumours and utilised MRI to non-invasively quantify particle delivery. As shown in previous investigations on glioma tumour models[123,184], a reduction of T_2* was observed in magnetically targeted tumours while no significant change was observed in the contralateral control tumour. The T_2* weighted images are particularly important in this method due to their sensitivity to the local field inhomogeneity brought by magnetic particles. This was also previously demonstrated by a handful of magnetic targeting publications[5,12,123,156]. While Chertok et al.,[123] noted homogenous hypointensities in their glioma

MR images, I observed discrete patches of hypointense regions distributed across the tumour tissue. This is likely the result of the difference in passive delivery of nanoparticles between the two tumour models as the glioma model used in the previous reports has about 4.5-fold higher capillary blood perfusion[179,185] compared with the tumour model used in this study[186]. The discrete regions of hypointensities observed in this study allowed for the spatial mapping of accumulated particles using MRI.

Quantitative analysis on the spatial distribution of T_2* demonstrated that nanoparticles accumulate preferentially on the side of the tumour directly adjacent to the magnet, with less of an effect on the distal side when targeting is performed using the disk magnet. T_2* reduced to 51% of its initial value after magnetic targeting at 1 mm across the tumour whereas the corresponding decline was only 27% at 4 mm tumour depth. These observations are consistent with the phantom flow findings as well as previous investigations on magnetic cell targeting[36], which indicate the limited ability of the traditional surface magnets to target magnetic nanoparticles in tumours. The next chapter of this thesis demonstrates the novel scalable magnetic designs which aim to improve the depth penetration limitation of permanent magnets.

3.5 Conclusion

Since the first application of magnetic drug targeting in the 1970s[6], cylindrical surface magnets have traditionally been the magnet of choice for magnetic micro/nanoparticle targeting studies. The systematic approach we employed in this study allowed us to characterise the ability of a strong traditional surface magnet on magnetic targeting of commercially available SPIONs. Flow phantom studies demonstrated the limited spatial range (8 mm) of nanoparticle capturing when the traditional disk magnet is used for targeting. These observations were confirmed in our *in vivo* investigations when limited magnetic targeting was observed at deeper locations across targeted tumours. This led to the design and investigation of our scalable magnetic devices which will be discussed in the next chapter of this thesis.

4. Magnetic targeting of SPIONs using custom made permanent magnets

Chapter 3 of this thesis demonstrated magnetic targeting of individual nanoparticles using a single disk permanent magnet. My observations indicated the limited ability of the conventional single magnet to target nanoparticles in deep locations within the tumour tissue. This chapter reports marked magnetic targeting of individual nanoparticles to tumours using novel custom-made permanent magnetic designs, which have a clinical end-point in mind. The efficiency of targeting of the proposed magnetic design was first validated *in vitro* using flow phantom experiments. Subsequently*, in vivo* magnetic tumour targeting experiments were performed to investigate depth penetration of such magnet designs in subcutaneous tumours. Finally, a scaled up magnet design was proposed, which has the potential to target individual nanoparticles in deep locations of the human body (< 7 cm) for the first time.

4.1 Introduction

Magnetic drug targeting aims to direct magnetisable therapeutic agents to tumour[27,187,188], blood clot[189] or infection[190] regions. Such targeting strategies can reduce the distribution of drugs to the rest of the body, thus minimising side effects such as those caused by systemically administered chemotherapy[191,192]. As discussed in previous chapters, the effectiveness of magnetic drug targeting depends, in addition to the vascularisation of the targeted region [123,193] , on the magnetic force applied on the drug carriers. As such, magnet design plays an important role in delivery of therapy to pathological tissues. Developing or choosing an ideal magnetic system for specific targeting purposes is thus very important.

Existing magnetic drug delivery techniques commonly use permanent or electromagnets to capture particles at the blood vessels of the target tissue by placing the magnets in close proximity to accumulate the therapy[182,194](see section 1.2). The magnetic field strength of used magnets ranges from 70 mT[195] to 2.2 T[196] with corresponding applied field gradients from 3 T/m[197] to 100 T/m[124]. This magnetic field strength and gradient range reflects desired or possible depth of targeting versus magnet cost, complexity, and ease-of-use. Although the proposed magnet designs produce a large magnetic field strength and gradient at short ranges, the distances over which they produce useful magnetic forces are substantially limited. To date, only a targeting depth of 0.5 cm has been achieved in human clinical trials with individual 100 nm diameter particles using 0.8 T strength magnets[11,198]. To address such limitation, optimised permanent magnetic arrays have been designed to target microparticles up to a distance of 5 cm in the brain[118]. However, as discussed in chapters 1 and 3, utilising microparticles for drug delivery is not very desirable due to the higher risk of blood vessel blockage, increased rate of clearance of larger particles by the RES system, and lower chance of extravasation through vasculature of tumours[10].

The focus of this chapter is to investigate novel magnetic designs to increase the depth over which unencapsulated nanoparticles can be captured in the body. Compared to the traditional disk magnet, these magnetic setups generate a larger region of space with useful magnetic forces; which we refer to as ‘magnetically active space’. Such magnetic design facilitates deeper body targeting as well as increasing homogeneity of nanoparticle capturing throughout the target site.

In this study, I investigated the effect of the larger magnetically active space on magnetic tumour targeting of 100 nm particles using two novel magnet designs**. (i) Magnetic mangle**: a double cylindrical permanent magnet designed to achieve a more uniform exposure of magnetic field gradient compared to a single magnet. **(ii) Pyramid magnet:** a bespoke disk magnet with a pyramidal magnetically active space, which creates a 3 dimensional exposure of strong magnetic field gradient by encompassing the tumour volume. I employed an *in vitro* flow phantom to test capturing efficiency of the 100 nm particles using a larger magnetically active space. The flow phantom results were then validated using *in vivo* magnetic tumour targeting experiments in combination with quantitative MRI. The capturing efficiency and nanoparticle distribution achieved with the two novel magnetic designs were compared with the results of the conventional permanent magnet discussed in chapter 3. Finally, I present an up-scaled magnet capable of targeting nanoparticles up to a depth of 7cm within specific parts of the human body.

The aims of these experiments were:

(i) To investigate the effect of magnetically active space on capturing efficiency of unencapsulated nanoparticles using *in vitro* phantom experiments

(ii) To produce a bespoke permanent magnet and investigate the effect of magnetically active space using *in vivo* tumour targeting experiments

(iii) Producing an up-scaled permanent magnet design to increase depth of targeting within the human body.

4.2 Materials and methods

4.2.1 Custom magnet designs

(i) Magnetic mangle: a magnetic configuration consisting of two cylindrical N42 Neodymium magnets (20 mm X 20 mm thick diametrically), which are fixed in place with a gap of 14 mm in between them. This device was originally designed and produced for magnetic stimulation of brain cells by Chris Payne and Yichao Yu under supervision of Professor Quentin Pankhurst. These magnets are diametrically magnetised perpendicular to their long axis, and are able to rotate about their long axis. The magnetic field topography in the magnetically active space of these magnets is a function of angle between magnetisation directions of the two magnets. In these experiments, a collinear magnet configuration was used with an N-S-N-S pole arrangement between the two magnets. The magnetic field strength between the magnets was simulated in this orientation (magnets aligned), in two orthogonal planes (Fig. 4.1) using Opera Cobham simulation software (Oxfordshire, UK). The $(\boldsymbol{B}.\nabla)\boldsymbol{B}$ magnitude was calculated and plotted using MATLAB 2016a (Fig. 4.3 A,B).

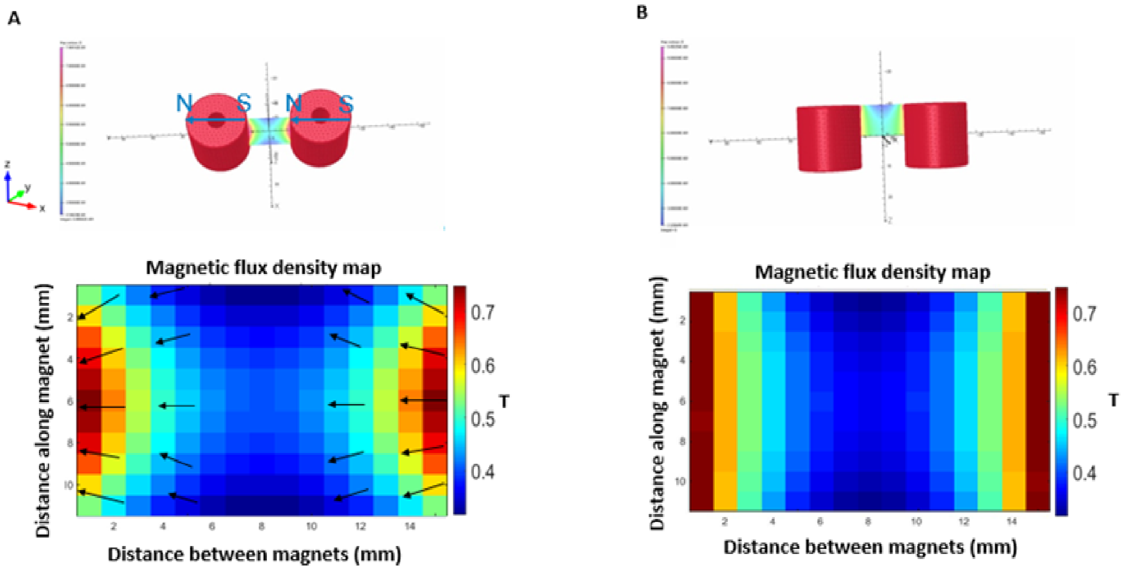

Figure 4.1- Simulation of the magnetic flux density around the mangle magnets. (A) Magnetic flux density map between the two cylindrical magnets in the xy plane. The flux direction is shown on the map. (B) Magnetic flux density map in the orthogonal plane between the two magnets in the xz plane. The flux direction is pointing towards the perpendicular plane.

(ii) Pyramid magnet: To maximise the chances of nanoparticle capturing within subcutaneous tumours, I needed to design a magnet that encompasses the whole tumour volume rather than being applied on the surface. As such, I approached Giamag magnet manufacturing company to investigate whether they could employ their high-gradient magnetic assemblies to produce the magnetic design I had in mind. I collaborated with Henrik Høyer in Giamag technologies and after theoretical optimisations he came up with the pyramid magnet design, which is a cylindrical neodymium iron boron permanent magnet (1.45 T residual magnetism, grade N52) containing a pyramidal hollow space to accommodate the subcutaneous tumour. The pyramidal space has a length and width of 12 mm and depth of 6 mm. The magnetic flux density (Fig. 4.2) and B.gradB (Fig. 4.3 C, D) maps were simulated and shown for a circular surface with diameter 10 mm inside the pyramidal cavity in two orthogonal planes where the subcutaneous tumours were positioned during magnetic targeting. Simulations were made using COMSOL multiphysics software.

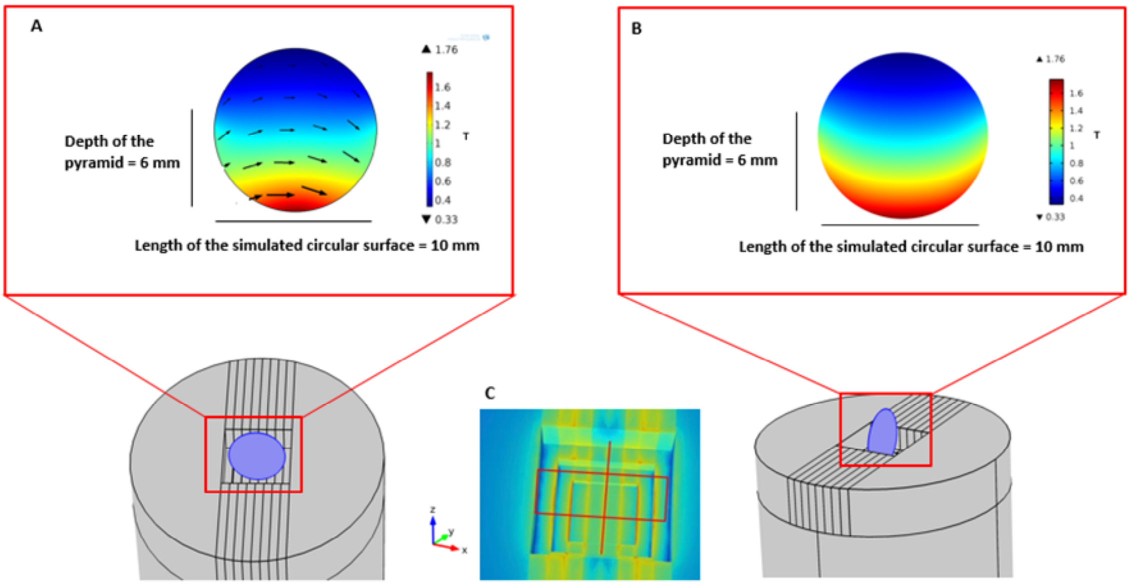

Figure 4.2- Simulation of the magnetic flux density inside the pyramid magnet. (A) Magnetic flux density map inside the pyramidal cavity. The flux direction is shown in the figure. (B) Magnetic flux density map in the orthogonal plane. The flux direction is pointing towards the perpendicular plane and hence not visible on the map. (C) The pyramidal cavity inside the magnet. The cavity has a length and width of 12 mm and a depth of 6 mm. The two planes where the magnetic field strength was simulated are indicated by red boxes.

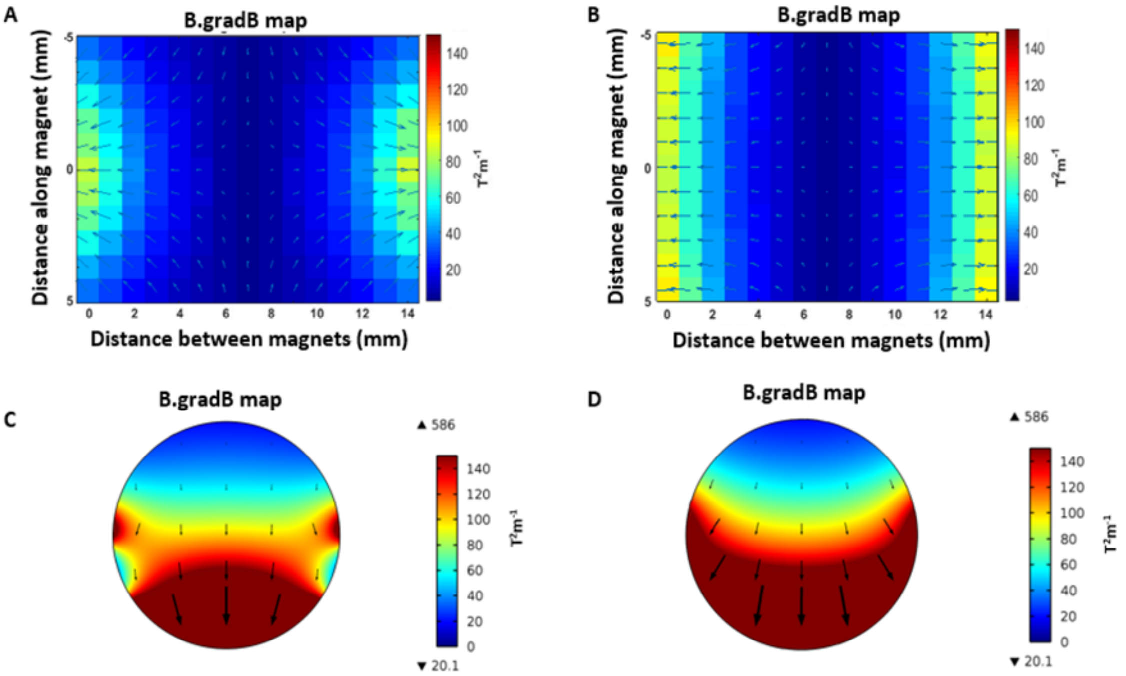

Figure 4.3- Calculation of the B.gradB values around the magnet designs. (A) Magnetic mangle: B.gradB map in the horizontal plane between the magnets. (B) B.gradB map in the vertical plane between the magnets (C) Pyramid magnet: B.gradB map inside the magnetic space. (D) The B.gradB map of the pyramid magnet in the orthogonal plane. The directions of the vector fields are shown on the maps.

4.2.2 Vascular flow phantom

A phantom flow experiment was used to simulate magnetic targeting of magnetic nanoparticles in a simplified model. The experimental setup was similar to the experiments presented in chapter 3. A standard configuration consisting of the magnet and a 0.38 mm internal diameter capillary tube (Smiths Medical Ltd, UK) was used. A total mass of 0.4 mg (equivalent to a 20 g mouse injection dose of 20 mg/kg) of fluidMag-CT particles (Chemicell, Germany, 100 nm) were diluted with 1.5 mL of PBS (typical mouse blood volume) and infused into the tube using an infusion pump (PHD 2000 Harvard Apparatus, US). Similar flow velocities as the experiment performed by the disk magnet (see section 3.2.2) were chosen at 5 mms^{-1}, 8 mms^{-1} and 10 mms^{-1} corresponding to flow values of 0.037 mL/min, 0.060 mL/min and 0.075 mL/min respectively. The total infusion volume was kept constant for all experiments. The tube was positioned at 6 distances (0, 3, 6, 8, 11 and 14 mm) relative to one of the magnets in the magnetic mangle design and nanoparticles were infused into the tube at similar flow velocities.

Quantification using ferrozine assay:

Similar to the results in chapter 3, the tubes containing accumulated nanoparticles were flushed with 0.6 M hydrochloric acid and incubated in a heat block at 65 °C for 2 h. 30 µL of pre-made ferrozine reagent was then added to the samples and the absorbance was measured at 570 nm using a benchtop spectrophotometer (Multiskan$^{\text{TM}}$ FC microplate photometer, Thermo scientific). The same procedure was carried out for serial dilutions of known amounts of FluidMag-CT particles to allow calibration. Figure 4.4 A indicates the samples after addition of the ferrozine reagent. Linear interpolation to serial dilution absorbance results allowed iron quantification from the absorbance results acquired from the samples (Fig. 4.4 B). The capturing efficiency for each sample was calculated as the percentage of the captured particles over the total perfused mass of particles.

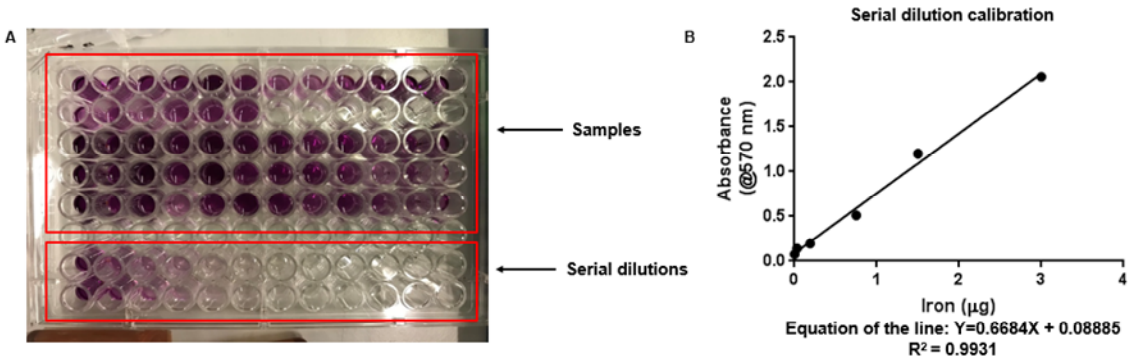

Figure 4.4 - Quantification of nanoparticle accumulation using colorimetric ferrozine assay. (A) An example 96 well plate containing the assay samples and serial dilutions for calibration of iron quantification. (B) Calibration line from serial dilutions ($R^2 = 0.0031$)

4.2.3 *In vivo* magnetic targeting and imaging

The experimental setup was similar to the experiments presented in chapter 3. All animal studies were approved by the University College London Biological Services Ethical Review Committee and licensed under the UK Home Office regulations and the Guidance for the Operation of Animals (Scientific Procedures) Act 1986 (Home Office, London, UK). Mice (n=12) were subcutaneously injected on each flank with 1 million LS174T colorectal tumour cells (ATCC, CL-188) and monitored every 2 days by visual inspection. Two weeks after cell implantation, anaesthesia was induced and maintained in 1.5-3.0% isoflurane in 1 L/min O_2 and 0.4 mg of 100 nm fluidMAG-CT particles were intravenously injected into the mouse via a tail vein. The magnets (Mangle, n=6 and pyramid, n=6) was positioned directly over the surface of one of the bilateral tumours during and for 20 minutes post nanoparticle injection.

MR imaging:

Mice were positioned in a 35 mm Rapid RF coil and maintained at 37 °C with warm water tubing and temperature and respiration monitoring with rectal probe and pressure-sensitve pad (SA instruments Inc.); respiration rate was typically 60-80 bpm. T_2* map images were acquired before and after magnetic targeting experiment using respiratory-triggered and multiple gradient echo sequences (TR 1500 ms, 5 echoes TE 5.2-30 ms, 1 average, 192^2, 30x30 mm, 1 mm thick slices) using a 1 T Bruker ICON scanner (Bruker, Germany).

In order to perform three-dimensional MRI scan on *ex vivo* tumours, tumour samples were fixed in 4% paraformaldehyde overnight. The samples were then placed in a phantom with 1% agar and the phantom was imaged using 3D spoilt gradient echo (SPGR) sequence (TR = 15 ms, TE = 7 ms, matrix = 512 x 512 x 512, FOV = 30 x 30 x 30 mm, total acquisition time = 5h 27 min, image resolution 59 x 59 x 59 μm^3) using a 9.4 T Varian Inova scanner (Varian, Santa Clara, CA).

Image analysis:

Similar to the post MRI image analysis performed in chapter 3, the T_2* maps were estimated by mono-exponential fitting of signal decay to each voxel in manually chosen regions of interest (ROIs) using non-linear least squares method in MATLAB. To map the distribution profile of nanoparticle accumulation within tumours, the T_2* value of line segments located at 1 mm intervals through the tumour were measured for both targeted and non-targeted tumour groups before and after nanoparticle injection (n=6) for each magnet experiment group. This was performed between the ranges of 1 to 4 mm within the tumours. Data were analysed with in-house MATLAB code.

The 3D images of tumour samples were manually segmented on 3D gradient echo images. Firstly, the intensity values were scaled to between zero and one by dividing by the maximum signal intensities and then thresholding was performed on regions that were less than an arbitrary value chosen to be 0.2. The manually segmented images were then volume rendered using ImageJ software 3D Viewer (Rasband, ImageJ, NIH, Bethesda, Maryland, USA).

Direct Iron quantification by ferrozine assay:

Similar to the experiments described in chapter 3, to validate MR imaging results, mice were sacrificed and the subcutaneous tumours were removed; 2mL Lysing matrix D tubes containing tissue homogeniser beads were purchased from BP Biomedicals (Santa Ana, California, USA). The tumour samples were placed in the lysing tubes and a high-speed benchtop reciprocating homogeniser (Fastprep-24™ Sample Preparation Instrument, MP Biomedicals) was used to homogenise the tissue samples. 50 mg of each tissue sample was transferred to a 1.5 mL test tube, 100 µL of 0.6M hydrochloric acid was added to each sample and the samples were incubated in a heat block at 65 °C for 2 h. 30 µL of pre-made ferrozine reagent was then added to the samples and the absorbance was measured at 570 nm using a benchtop spectrophotometer (Multiskan™ FC microplate photometer, Thermo scientific). The same procedure was carried out for serial dilutions of known amounts of fluidMag-CT particles to allow calibration.

4.2.4 Mathematical modelling of magnetic targeting in human body

In order to scale-up the magnet size to human dimensions, I employed mathematical calculations in accordance with Nacev-shapiro magnetic targeting construct[180] to validate that a B.gradB value of 3 T^2m^{-1} is large enough to produce successful magnetic targeting in human blood vessels. This section provides explanation about the mathematical equations, models and parameters that were used to perform these calculations.

Estimation of the forces acting on the 100 nm FluidMAG-CT particles:

1. Magnetic force:

The magnetic force exerted on nanoparticles was estimated using the equation $F_m = \frac{V_m \Delta\chi}{\mu_0}(B.\nabla)B$, where μ_0 is the permeability of free space, V_m is the volume of the magnetic core of the particles (volume of the SPION), and $\Delta\chi$ is the relative susceptibility of the SPION [32]. As with the Al Jamal et al[5], we took the first approximation of the spatial B.gradB values ($|(B.\nabla)B| \approx$

B.gradB) that has been calculated for each magnet in the plane going away from the magnet edge or surface. Since the magnetic properties of the FluidMAG particles are well established within the literature, I used parameters already reported in previous studies. To calculate the volume of the magnetic entity, I used a mean diameter value of 70 nm for the multicore cluster of 100 nm FluidMAG particles as previously quoted from HRTEM images[183]. The effective susceptibility of the magnetite (Fe_3O_4) that constitutes the core of the particles was estimated as $\Delta\chi \approx \rho_s\chi_s$, where $\rho_s \approx 4.9 \times 10^3$ kg m^{-3} is the density and $\chi_s \approx 9.8 \times 10^{-4}$ m^3 kg^{-1} is the mass susceptibility of magnetite[180]. Using these values, an effective magnetic force of 2×10^{-15} N was estimated on a single particle using a B.gradB value of 3 T^2m^{-1}.

2. Stokes drag force:

The magnetic force applied on the nanoparticles is counteracted by the drag force of the flowing blood within the blood vessels. This force can be estimated by the equation $F_s = 3\pi d_H \eta V_{blood}$ where d_H is the hydrodynamic diameter of the magnetic particle, η is the blood viscosity and V_{blood} is the maximum blood velocity[5]. I used a hydrodynamic diameter of 110 nm for the 100 nm FluidMAG particles as quoted from the HTREM images[183]. Using these values, an effective drag force of $F_s = 3.11 \times 10^{-10}$N was estimated on each individual particle.

Comparing the magnetic forces per particle to Stokes drag shows an apparent mismatch between these two values which predicts a non-successful magnetic targeting as it was previously demonstrated in calculations carried out in previous studies[180]. However, the rough comparison above is deficient for two main reasons[180]. Firstly, the drag force experienced by particles varies with their position in the blood vessels. Particles near the blood vessel walls experience lower drag force than the ones at the vessel centre. Secondly, the particles aggregate to some degree despite the fact that they were engineered to minimise aggregation. As the magnetic force grows with volume, much more than Stokes drag, which grows with radius, the aggregation increases magnetic capturing of nanoparticles. As such, the Nacev-Shapiro calculation which is a more reliable mathematical model was utilised as described below.

Nacev-Shapiro model calculations:

Nacev-Shapiro model explores the behaviour of magnetic particles experiencing diffusive, convective, and magnetic forces in a straight idealised blood vessel surrounded by tissue[180]. Three different behaviour regimes are predicted by this model: magnetic dominated, blood velocity dominated, and a boundary layer formation based on three physical parameters. Only in the case of the boundary layer formation regime magnetic particles can be concentrated in the target region by the applied magnetic force. The three physical parameters are as follows:

(i) Magnetic Richardson number (Ψ). This is the ratio of the magnetic force to the Stokes drag force acting on nanoparticles.

(ii) The mass Peclet number (Pe). This is the ratio of the convective and diffusive coefficients in the blood $Pe = \frac{d_B V_{blood}}{D_{total}}$, where d_B is the blood vessel diameter and D_{total} is the total diffusion coefficient.

(iii) The reduced Renkin diffusion coefficient (D) which is the ratio of the membrane (D_m) or tissue coefficient (D_t) coefficient over the total diffusion coefficient.

Nacev-Shapiro prediction on magnetic targeting in humans using our scaled-up magnet:

I used a magnetic entity radius of 35nm and particle hydrodynamic diameter of 110nm. I also used the same blood and blood vessel parameters reported by Al Jamal *et al*[5], as adopted from Lubbe *et al*[11] η = 0.003 Pa, V_{blood} = 0.1 m/s and d_B = 5 x 10^{-3} and the appropriate diffusion coefficients. After performing relevant calculations using a minimum B.gradB value of 3 T^2m^{-1}, the following results were obtained:

F_m = 2 x 10^{-15} N , $F_s = 3.11$ x 10^{-10} , $\psi = 7$ x 10^{-6} , $Pe = 8$ x 10^5 , $D = 0.001$

These results predict a boundary layer formation regime (successful magnetic targeting) within the tumour when a B.gradB of 3 T^2m^{-1} is applied. The predicted behaviour is shown in Fig 4.9.

4.3 Results

4.3.1 Flow phantom experiments

In chapter 3 I presented the results of my investigations on the effect of distance (B.gradB value), particle size and flow velocity on magnetic capturing of individual nanoparticles using a disk permanent magnet in a vascular flow phantom. In order to investigate the effect of magnetically active space on nanoparticle entrapment, I repeated the flow phantom experiment on 100 nm particles using the magnetic mangle design. The tubing was placed between the two magnets at distances of 0-14 mm (Fig. 4.5 A). Compared to the disk magnet, magnetic mangle produces a larger region of space with substantial magnetic field gradients. For example, the sum of B.gradB values in the vertical direction at 3 mm distance (dashed area, Fig. 4.5 B, C) from one of the magnets in mangle design (212 T^2m^{-1}) was found to be 1.6-fold higher than the corresponding value for the disk magnet (133 T^2m^{-1}).

Capturing efficiency was markedly increased comparing to the disk magnet at 0, 3 and 8 mm distances when flowing at 5 mms^{-1} (n=3, $*P \leq 0.05$, Fig. 4.5 D). When flowing at 8 mms^{-1} capturing efficiency was significantly increased at 3 and 6 mm distances (n=3, $*P \leq 0.05$, Fig. 4.5 E). At 10 mms^{-1} velocity, capturing was markedly increased at all tested distances (n=3, $*P \leq 0.05$, Fig. 4.5 F). The capturing efficiency at 5 mms^{-1} and 3 mm distance (17.3 ± 1.3%) was observed to be 1.9-fold higher than the corresponding value for the disk magnet experiments (8.9 ± 0.8%). Interestingly, the difference in capturing efficiency between the two magnets was similar to the 1.6-fold difference in the B.gradB generated by the magnets at this distance. Due to the design of the pyramid magnet similar experiments could not be performed for comparison.

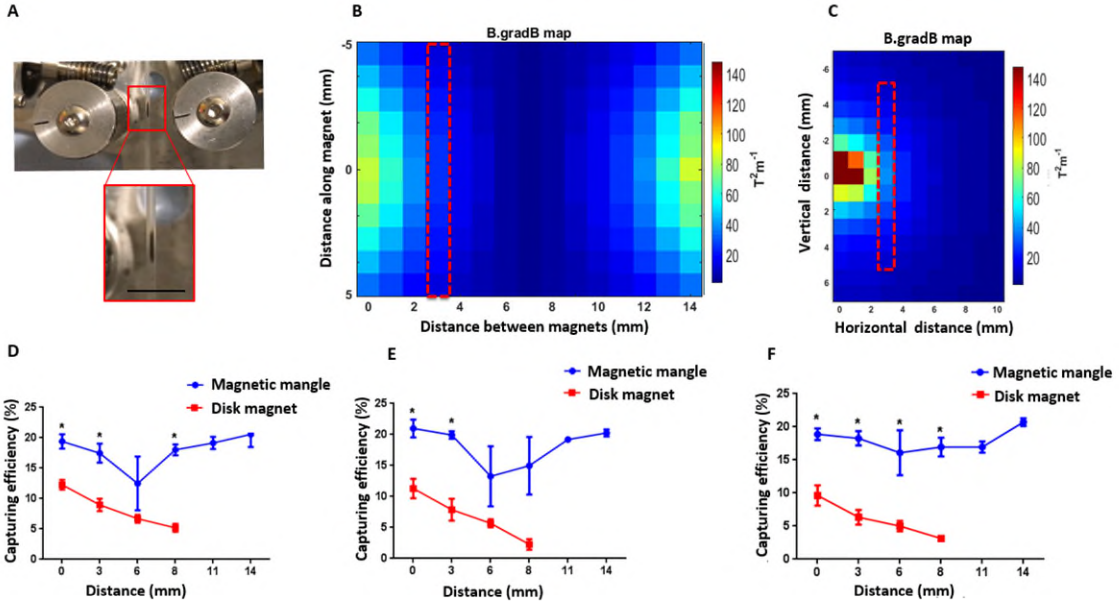

Figure 4.5- Magnetic targeting of nanoparticles in a flow phantom – Effect of magnetically active space. (A) Experimental set up showing tubing with the accumulated nanoparticles flowing past the two magnets at flow rate of 5 mms^{-1}. Accumulation of particles visible on internal tube wall, scale bar 10 mm. (B) The B.gradB map (T^{2}m^{-1}) of the magnetic mangle in the plane between the two magnets where the tubing was positioned. The direction of the vector field is towards the surface of each magnet. (C) The B.gradB map (T^{2}m^{-1}) of the disk magnet in the plane moving away from the edge and at 30 degrees from the circular face of the magnet where the tubing was positioned. The direction of the vector field is towards the magnet edge. Capturing efficiency of accumulated 100 nm particles at 5 mms^{-1} (D), 8 mms^{-1} (E), and 10 mms^{-1} (F), flow velocities and 6 distances produced by the disk and mangle magnet designs (*$P<0.05$, n=3). Data shown as mean ± SD.

4.3.2 *In vivo* magnetic targeting

To investigate *in vivo* targeting of tumours exposed to a larger magnetically active space, I performed *in vivo* experiments using the mangle and pyramid magnet designs (Fig. 4.6 A, B). Compared with the disk magnet results, more homogenous magnetic targeting in post injection T_2* images of the targeted tumours were detectable. I observed a significant reduction in the T_2* of the tumour tissues targeted with both the magnetic mangle (n=6, *$P < 0.05$) and pyramid magnet (n=6, *$P < 0.05$) designs. In the contralateral control tumour, the tumour T_2* did not change after injection of nanoparticles. Ferrozine assay measurement of the *ex vivo* tumour tissues demonstrated a significant difference in iron content between the targeted and non-targeted tumours for both magnet experiment groups (n=6, *$P < 0.05$, Fig. 4.6 C, D). Linear regression analysis revealed a significant correlation between the percentage enhancement in iron measurement of the ferrozine assay and the T_2* reduction of the targeted tumours (R^2=0.9635, *P ≤ 0.05, Fig. 4.6 E).

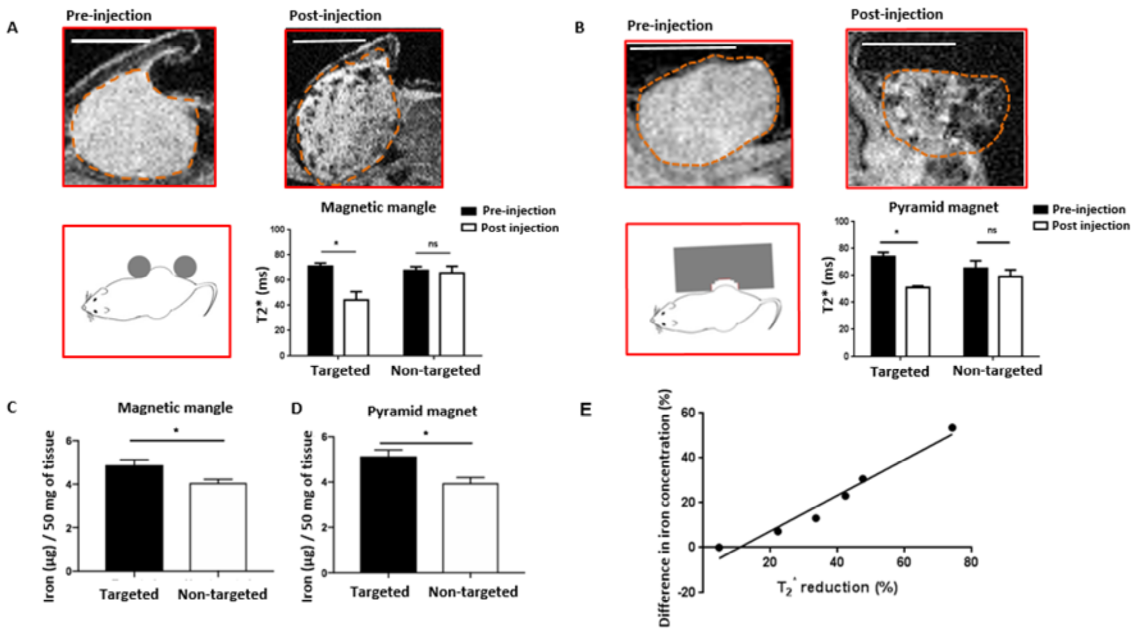

Figure 4.6- *In vivo* magnetic targeting of nanoparticles using the mangle and pyramid magnets. (A) *In vivo* magnetic targeting using the magnetic mangle design. The figure shows the ROIs of the pre and post injection for a targeted tumour. Scale bars 5 mm. Magnetic targeting significantly reduces the mean tumour T_2* after injection of magnetic nanoparticles (*P<0.05, n=6). (B) *In vivo* magnetic targeting using the pyramid magnet design. The figure shows the ROIs of the pre and post injection for a targeted tumour. Scale bars 5 mm. Magnetic targeting significantly reduces the mean tumour T_2* after injection of magnetic nanoparticles (*P<0.05, n=6). (C) Quantitative ferrozine assay of magnetically targeted tumours using the magnetic mangle (*P<0.05, n=6). (D) Quantitative ferrozine assay of magnetically targeted tumours using the pyramid magnet (*P<0.05, n=5). (E) Reduction in T2* vs enhancement in nanoparticle capturing measured by the ferrozine assay for each individual tumour targeted with the pyramid magnet (P=0.0005, R^2= 0.9635). Data shown as mean ± SEM.

In order to acquire more insight into the accumulation profile of the targeted nanoparticles, high resolution 3D gradient echo images were acquired from the *ex vivo* tumour tissues. Figure 4.7 shows three-dimensional reconstructions that display the nanoparticle distribution within the targeted (Fig. 4.7 A) and non-targeted (Fig. 4.7 B) tumours. Hypointensities (segmented as red) can be observed throughout the whole volume of the targeted tumour and are not confined to the region closest to the magnet, consistent with the strong force experienced by the nanoparticles from the pyramid magnet over the whole volume (see Fig. 4.3 C, D).

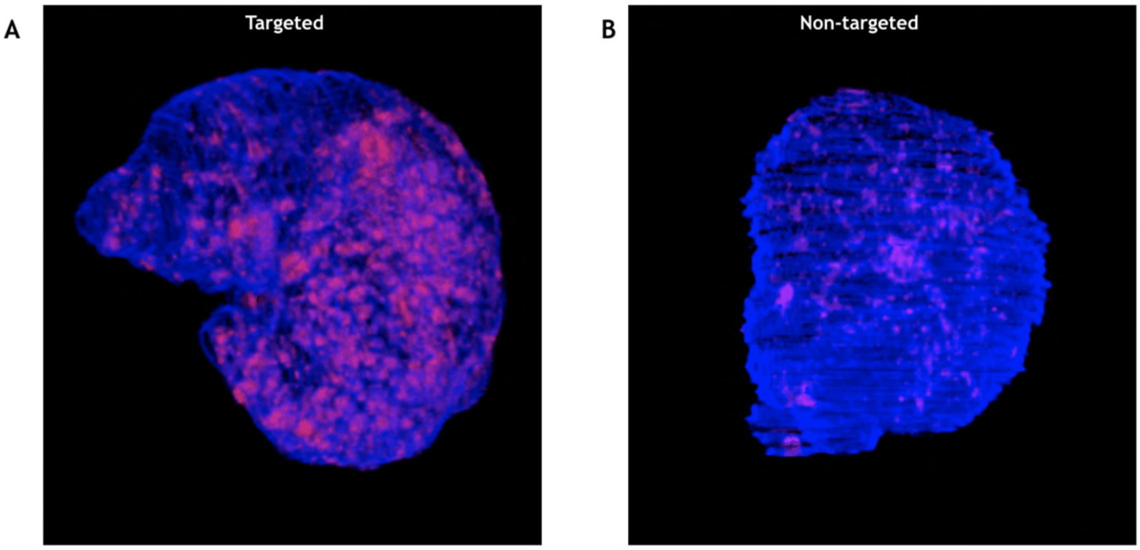

Figure 4.7- Three-dimensional reconstruction of *ex vivo* tumour tissues. Targeted (A) and non-targeted (B) tumours post nanoparticle injection. The figure indicates the homogenous distribution of nanoparticles within the tumour targeted using the pyramid magnet. Segmented hypointense regions are shown in red.

4.3.3 Effect of larger magnetically active space – *in vivo* targeting distribution

The ideal magnet design would apply a sufficiently strong magnetic force throughout the whole tumour. As such I took a quantitative approach to compare our 3 magnet designs. I investigated the spatial distribution of nanoparticles within the tumours quantitatively by measuring the T_2* values across tumours (1 to 4 mm within each tumour) before and after nanoparticle administration (Fig. 4.8 A-C, similar to section 3.3.2). I further performed linear regression analysis on the post-injection T_2* values to investigate whether the slope of T_2* deviates from zero as we move deeper within the tumour.

Investigating the magnets individually: i) *Disk magnet,* as shown in chapter 3 (section 3.3.2), I observed an increasing trend in post-injection T_2* of the targeted tumours. The slope of the post-injection T_2* was different from zero (n=6, $^*P \leq 0.05$, Fig. 4.8 A) and as expected, the further away from the magnet, the less targeting was observed. A significant reduction in T_2* was observed only at 1 mm distance within the tumour.

ii) *Mangle design*, I found a similar increasing trend in post-injection T_2* of the targeted tumours, presumably as the tumour was located close to one of the magnets. The slope of the post-injection

T_2* was different from zero (n=6, *P ≤ 0.05, Fig. 4.8 B). T_2* significantly reduced up to a distance of 3 mm into the tumour.

iii) *Pyramid magnet*, T_2* of targeted tumours showed no change in T_2* with respect to distance. No deviation from zero was observed on the slope of the post-injection T_2* line (n=6, P =0.9117, Fig. 4.8 C). T_2* reduction was significant at all depth within the tumour (n=6, *P ≤ 0.05). As such, it can be concluded that the pyramid magnet produces the most uniform and most homogeneous targeting within tumours.

In order to compare the spatial distribution of nanoparticle accumulation with the magnetic force applied by each magnetic design, the force (denoted by the B.gradB map) generated by each magnet, and the approximate tumour position within each map are shown in two dimensional plots (Fig. 4.8 D-F)**.** The B.gradB magnitude at a distance of 6 mm away from the disk magnet (6 T^2m^{-1}) was similar to the corresponding value generated by one of the cylindrical magnets in the mangle design (5 T^2m^{-1}). The sharp decline in the magnitude of the applied force, accounts for the reduction in targeting at deeper locations of the tumour. Conversely, the pyramid magnet generates considerably larger B.gradB (>90 T^2m^{-1}) across the tumour volume, consistent with the observed homogenous targeting within the tumours.

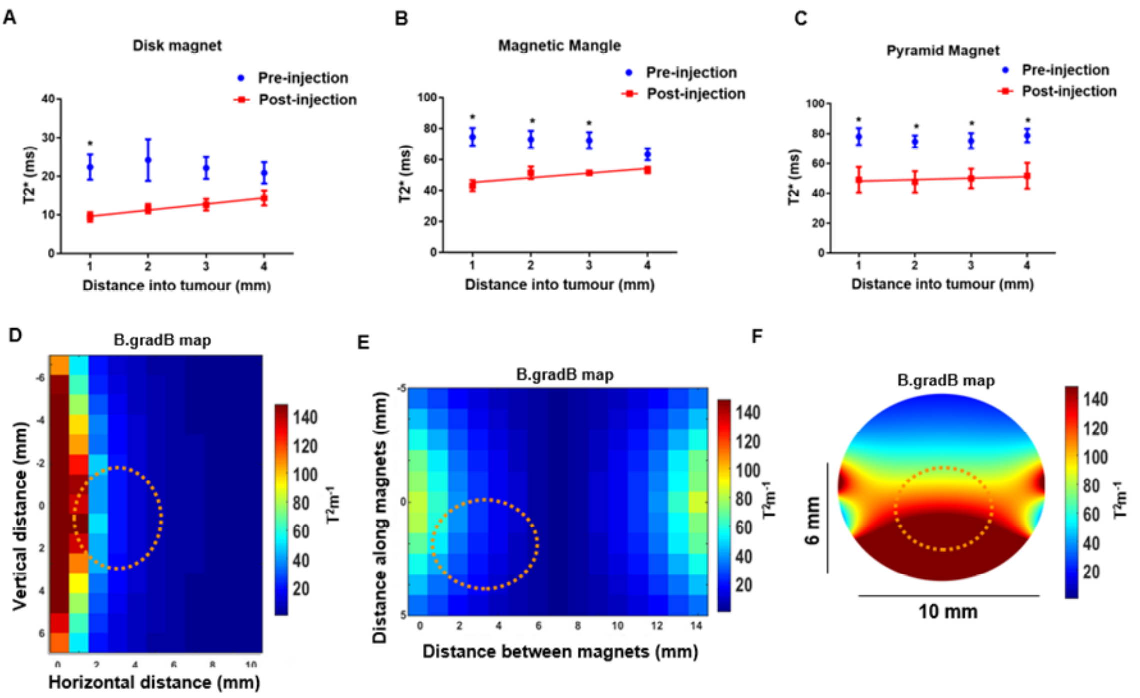

Figure 4.8- Effect of magnetically active space on magnetic tumour targeting. The spatial T_2* distribution of the magnetically targeted tumours pre and post nanoparticle injection using the three magnet designs. (A) The disk magnet (n=6, *P ≤ 0.05). (B) The magnetic mangle (n=6, *P ≤ 0.05). (C) The pyramid magnet (n=6, *P ≤ 0.05). B.gradB topography of the three magnet designs on the same colour threshold. The approximate tumour position is shown in each map. (D) The disk magnet. The direction of the vector field is towards the magnet edge. (E) The magnetic mangle. The direction of the vector field is towards the magnet surfaces. (F) The pyramid magnet. Data shown as mean ± SEM.

4.3.4 Upscaling magnet design from mouse to human

In order to target individual nanoparticles at distances similar to human proportions, I aimed to translate the magnet designs into larger dimensions. The ideal up-scaled magnet would have a magnetically active space large enough to accommodate a part of human body and strong enough to target individual nanoparticles in human tumours. The flow phantom experiments showed that the minimum B.gradB value, which allowed capturing of 100 nm particles against flow was 3 T^2m^{-1}. As such, I used mathematical modelling in accordance with Nacev-Shapiro magnetic targeting construct (see section 4.2.4) to confirm that this B.gradB magnitude is large enough to capture 100 nm particles in human blood vessels. I adopted the blood and blood vessel parameters in humans from the Lubbe et al clinical study[11], as reported in Nacev et al[180] and Al-Jamal et al[5]. The results of these calculations predicts a boundary layer formation regime when using a B.gradB value of 3 T^2m^{-1}, which indicates successful magnetic targeting (Fig. 4.9).

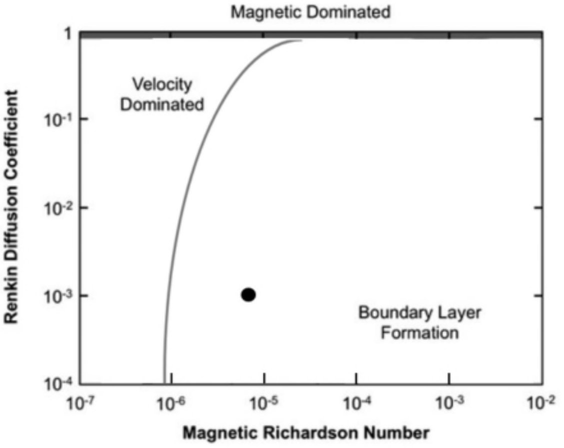

Figure 4.9- The results of the nacev-shapiro magnetic targeting model using a clinical parameter scale and a minimum B.gradB value of 3 T^2m^{-1}. The circular notation indicates the location of the calculated parameters within the boubdary layer formation. Mathematical calculations are explained in section 4.2.4.

I then worked with Giamag magnet manufacturing company to design a scaled-up magnet, which generates a minimum B.gradB value of 3 T^2m^{-1} (threshold value). The threshold value generated by the magnet decreases with increasing the size of the magnetically active space. As such the high-magnetic gradient design[199] of the pyramid magnet was used to design a magnet with a magnetically active space that generates the threshold strength value, and is readily constructed. Finite element modelling and simulations resulted in a U-shaped magnet design, which contains a magnetically active space of 10 cm long, 7 cm deep and 7 cm wide, equivalent to a total volume of 490 cm^3 (Fig. 4.10 A, designed by Giamag Technologies), producing a feasible solution for targeting chemotherapeutic agents in the breast, neck, leg, and other body organs with similar sizes. The maximum depth at which the threshold B.gradB value is generated is in the range of 5-7 cm from the bottom surface of the magnetically active space depending on the position with respect to the x-axis of the magnet (Fig. 4.10 B). The direction of the magnetic force is pointing towards the nearest magnet surface at any point within the magnetically active space (Fig. 4.10 C). These data made us confident that the high-magnetic gradient design of the pyramid magnet can be scaled-up to a magnet with suitable strength and dimensions for a clinical setting.

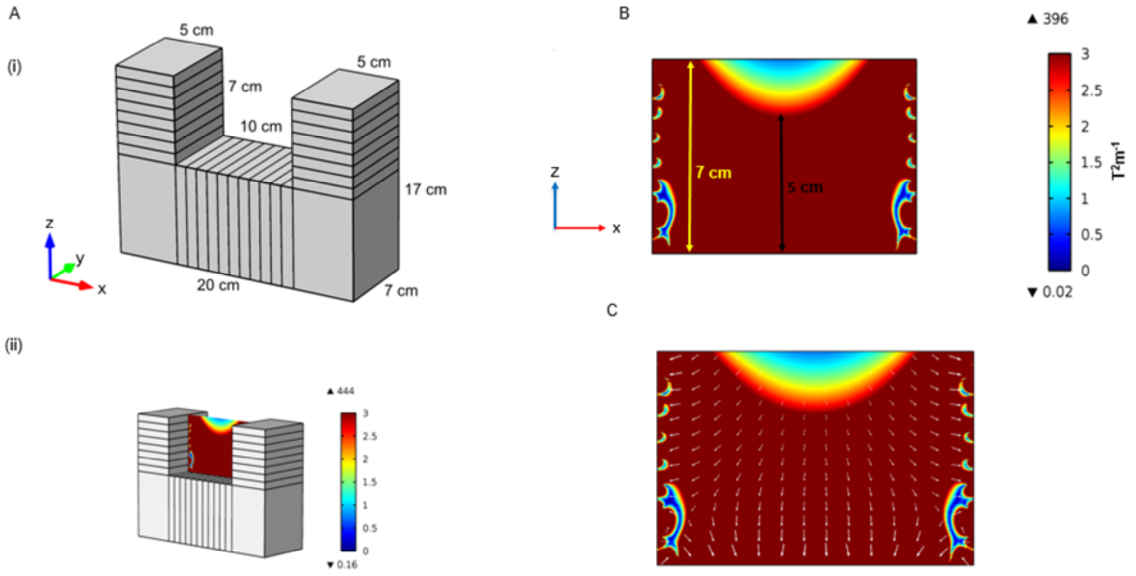

Figure 4.10- The scaled-up magnet design. (A) (i) The magnet shape and dimensions. (ii) The B.gradB plane within the magnetically active space in the xz plane. (B) The B.gradB map of the magnetically active space with a colour scale threshold of 3 T^2m^{-1}. (C) The vector field map of the B.gradB in the same plane. The direction of the vector field is towards the closest magnet surface.

4.4 Discussion

As a tool to target magnetic carriers to specific sites within the body, magnetic system plays a crucial rule in magnetic drug targeting. Different magnetic systems are used in previous investigations depending on the magnetic carrier and the target location. However, it is still unclear whether it will be possible to target nano-sized carriers to tissues deeper in the body[5,198]. This chapter reports marked magnetic targeting of unencapsulated nanoparticles to tumours using novel custom-made permanent magnetic designs, which have a clinical end-point in mind. These magnets were designed to target a specific volume of tissue, known as the 'magnetically active space', where a substantial magnetic field gradient is produced.

There are three major findings from this study:

- Magnetic capturing of 100 nm particles is increased with a larger magnetically active space.
- Exposing tumours to a larger magnetically active space increases targeting depth.
- The novel strategy introduced in this study has the potential to target tumours within 7 cm depth in human body.

4.4.1 Effect of magnetically active space – phantom experiments

Clinical investigations suggest that targeting of unencapsulated nanoparticles with single traditional permanent magnets is limited to less than 5 mm into the human body[5,11]. Using our magnetic mangle design, composed of one magnet on either side of the targeting region, we show that capturing depth is almost double (14 mm) that of the single magnet (8 mm). Moreover, improved capturing efficiency was observed throughout the entire targeting region of the mangle compared to the disk magnet, highlighting the need for designing magnets with a large magnetically active space. This led to the development of the pyramid magnet, designed to deliver a strong magnetically active space that would encompass the total volume of the subcutaneous tumours. Unlike previous custom-made electro and permanent magnets for magnetic nanoparticle targeting[123,200], the high-gradient design of the pyramid magnet[199] is readily scalable to human size proportions.

4.4.2 *In vivo* magnetic targeting using larger magnetically active space

Similar to the experiments performed by the disk magnet, I investigated *in vivo* magnetic targeting of unencapsulated 100 nm particles to subcutaneous tumours using the magnetic mangle and pyramid magnet designs. As reported in chapter 3, the discrete regions of hypointensities observed in the post-injection T_2* images of targeted tumours allowed quantitative investigation on distribution of nanoparticle accumulation within these tumours. When targeting was performed using the pyramid magnet, hypo-intense patches were observed throughout the whole tumour region with significant T_2* reduction at all tumour depths (<4 mm). Conversely, using the conventional surface magnet hypo-intensities were only observed at locations close to the magnet with T_2* reduction only significant at a depth of 1 mm. These results are consistent with the bespoke pyramid magnet having a magnetically active space covering the entire tumour volume.

Previously, Chertok et al[184] created a modified electromagnet setup, which exhibits an improved magnetic field gradient across the tumour region over their standard electromagnet design. Compared to the B.gradB value produced by this modified electromagnet setup (14.4 T^2/m), the pyramid magnet produces a minimum of 6 times higher strength (90 T^2/m) across the targeting region, which increases the likelihood of nanoparticle entrapment during their passage through the circulation. To date, the only other existing systems for magnetic drug targeting that are capable of applying similar field gradients over millimetre length scales are based on superconducting magnets[201].

4.4.3 Scaled-up magnet design

Magnetic drug targeting has been demonstrated in animals and human patients, but its utility has been limited to shallow targets[11,108]. The first clinical trial demonstrated efficacy of this technique in superficial tumours, which were located up to a depth of 5 mm from the skin in head, neck and breast cancers. Here, we have investigated minimum gradients required to capture unencapsulated nanoparticles in human blood vessels (see part 4.2.4) and have designed a scaled-up U-shaped permanent magnet capable of delivering these gradients. One cancer treatment which would specifically benefit from such magnet design is breast cancer, where single or multiple tumours are located within the breast tissue. Previous studies have demonstrated the efficacy of surface functionalised drug conjugated magnetic nanoparticles in breast tumour suppression and reducing systemic toxicity of drugs[202,203]. In addition to the selective accumulation of magnetic nanoparticles in tumours, the present study also shows that introduction of external magnetic field can significantly enhance such delivery, which is in agreement with previous reports[5,123]. Additionally, this study provides the potential to substantially increase achievable targeting depth of traditional permanent magnets from 5 mm to 7 cm distance into the breast or body organs that can fit inside the magnetically active space of the U-shaped magnet. It has to be noted that generating such magnetic gradients at centimetre distance scales is remarkable. To our knowledge, the most optimised permanent magnetic system designed for magnetic drug targeting[118] is capable of producing B.gradB values of about 0.3 T^2/m at 5 cm distance from the magnet. The U-shaped magnet can generate a minimum B.gradB value of 3 T^2/m at the same distance, delivering a 10-fold higher magnetic force.

4.5 Conclusion

In this study, two magnetic devices were developed, generating a larger magnetic exposure in comparison to a conventional disk magnet. Magnetic targeting of unencapsulated nanoparticles was then investigated using these magnet designs both *in vitro* and *in vivo*. In summary, our results suggest that compared to the disk magnet, our bespoke magnet design produces more homogenous and deeper nanoparticle distribution within the tumour. Using theoretical simulations, we have shown that our magnetic setup can be extrapolated to target unencapsulated nanoparticles in human tumours of up to 7 cm depth at specific locations of human body. To the best of my knowledge, this is the first study to report magnetic tumour targeting of nanoparticles using custom-made, strong and scalable magnetic designs. The next stage of this project will involve manufacturing the U-shaped magnet and performing in vivo investigations using this magnet.

5. Navigation of magnetic seeds in tissue using MR system

In chapters 3 and 4 of this thesis, I described my investigations on targeting individual nanoparticles using a range of permanent magnet designs. While permanent magnets can produce large gradients and are simple to operate, it may be challenging to use them at a clinical scale. The remaining chapters of this thesis will focus on targeting particles using clinically available electromagnets; the gradient sets of the MRI scanner. I propose an image-guided interstitial navigation strategy, whereby an MRI scanner could be used to guide an untethered ferromagnetic bead (referred to as thermoseed) through tissue to the tumour site, before inducing localised cell death via hyperthermia or delivering chemotherapy drugs. I have produced theoretical estimations for the amount of force that can be applied by the MRI system to a range of particle sizes and materials, and have used these results to select the appropriate ferromagnetic particle for phantom and brain slice work. Subsequently, I have demonstrated precise movement of these particles in viscous fluids. In summary, the movement of a 2 mm magnetic seed was investigated for the first time in *ex vivo* brain tissue using a standard preclinical MR imaging gradient set.

5.1 Introduction

With the increasing interest in micro robotic devices, the ability to manipulate their position in the body with precision would provide surgeons with a minimally invasive method for localised detection[204,205], drug delivery[156] and tissue ablation[2]. This is particularly important for cancer therapy as the preservation of healthy tissue is influential when it comes to improve patient prognosis and outcome of the treatment. In addition to high soft tissue contrast images provided by MRI for cancer diagnosis, ferromagnetic particles can also be imaged by MRI as they cause signal dropout and hypointense regions. The ability to diagnose cancer and localise the ferromagnetic particle can be further complimented by the magnetic field gradient inherent in all MRI scanners, which can generate translational forces onto the ferromagnetic device to steer it towards a target region within the body. Such a method has been previously demonstrated by guiding iron-oxide loaded cells[60,63,31], micro-carriers[156] and ferromagnetic objects[206] inside the body. As the MRI scanner can be used to both move and image an untethered device or therapeutic agent, it has the potential to replace the conventional surgical operations as a minimally invasive alternative. Additionally, delivering therapy using a single modality would negate the image registration issues associated with other image guided techniques (see section 1.1.3.2).

To date, the field of magnetic resonance targeting (MRT), a concept whereby the magnetic field gradients of an MRI scanner are used to direct magnetic particles inside the body, has focused on steering magnetic micro or nanoparticles through vasculature for the enhancement of drug delivery. While using MRI for movement offers significant advantage over other magnetic systems in terms of spatial homogeneity of magnetic force, unless the conventional clinical MRI scanners are substantially modified[130,131,132], the force they could apply on nano- or micro-particles is extremely limited. One way to increase this force is to use larger magnetic particles, which should lead to much greater control over the propulsion of the particle towards the target region. Preliminary studies have shown precise magnetic control of a single millimetre-sized magnetic object using a MRI scanner for navigation and tracking of micro-robots in the vascular network [207,206,208,209]. Although this method offers various advantages including limiting off target effects by bringing the therapy closer to the target site, the need for navigation of the magnetic particle through the vascular system limits the targeting ability to regions of the body with large vessel networks.

An alternative route of delivery of a magnetic object would be movement through tissue, which provides the ability to deliver therapy to any location within the disease region. The magnetic forces needed to guide magnetic particles through tissue, however, is far greater than that needed to move through the vasculature[210]. For this reason, the idea of tissue penetration using MRI was initially dismissed by Becker et al[161] due to the insufficient forces generated by MRI imaging gradients, which are typically < 80mT/m. This has brought about the development of more elaborate technologies such as the gauss gun[161], or magnetic hammer[169], which can be used with existing clinical MRI systems. However, these technologies would introduce additional complexity to the surgical procedure as well as lacking the required movement precision to become viable medical devices. To this end, we hypothesised that, with minimal modification to existing MRI gradients, tissue penetration may be possible using the MR system.

In this chapter, I have explored the capabilities of a conventional set of preclinical MRI scanner gradients on magnetic targeting of single millimetre-sized particles or ‘seeds’ in a variety of media including tissue. Firstly, three-dimensional movement of an iron-oxide magnetic seed was demonstrated using MRI gradients. Theoretical calculations were then employed to identify particles with improved magnetic properties in order to maximise the applied propulsion force. Subsequently, the control and accuracy of movement of these particles was investigated in agar and viscous media using a range of different particle size and magnetic gradient strengths. Finally, the possibility of movement of a 2 mm chrome steel seed in *ex vivo* tissue was demonstrated for the first time using a conventional set of preclinical imaging gradient coil. Observations on the movement are then discussed along with potential applications and suggestions for future investigations and optimisations.

The aims of this study were:

(i) To investigate the appropriate particle material and size for image-guided magnetic navigation using the MRI scanner.

(ii) To assess control and accuracy of movement of these particles in agar and viscous media.

(iii) To investigate possibility of movement of a single magnetic seed in ex-vivo brain tissue using a conventional preclinical gradient coil.

5.2 Materials and methods

This section will provide information on the materials and methods used to produce results demonstrated in section 5.3.

5.2.1 Demonstration of movement

Iron-oxide seed preparation:

In order to investigate possibility of movement using an MRI scanner, millimetre-sized magnetic particles were produced by forming large aggregates of iron-oxide powder. Fe_3O_4 powder (sigma Aldrich®) were purchased and 1-2 mm sized aggregates (approximately 80% Fe_3O_4) were made by sticking the powder grains together using super glue (Loctite).

Magnetic resonance targeting:

A magnetic targeting sequence was developed for magnetic resonance targeting of iron-loaded cells in previous studies[63]. This sequence provides control over the three gradient directions in MRI (Gro, Gpe and Gss) by allowing the user to control the strength, duty cycle and number of loops (repetitions) for each gradient direction (see Fig. 5.3).

For the purpose of the experiments carried out in this chapter, a 60 mm diameter bore gradient insert (Varian, Santa Clara, CA) was used capable of delivering a maximum of 1 T/m gradients. Due to the hardware limitation of cooling the gradient coil within safe ranges, at 500 mT/m a maximum duty cycle of 22% (ON/OFF of 2/7 or 20/70 ms) was used as with previous MRT demonstrations [63].

To demonstrate movement of magnetic particle using MRI gradients, a 1 mm iron-oxide particle was inserted in a 10 x 20 mm cylindrical well containing deionised water. In each direction, a gradient strength of 500 mT/m was applied with a 22% duty cycle ratio and a total of 100 loops.

MR imaging:

In order to locate the magnetic particle prior and post magnetic targeting, T_2*-weighted images were acquired after each magnetic targeting sequence using a Gradient Echo (GE) sequence

(TR = 15.428 ms, TE = 0.69 ms, 1 average, 64^2, FOV = 21.6x21.6x2 mm) using a 9.4 T Varian Inova scanner (Varian, Santa Clara, CA).

5.2.2 Theoretical calculation of magnetic force

The magnetic propulsion force was calculated for the iron-oxide aggregates and chrome steel spheres (AISI 52100) using the magnetic force equations 2.23 - 2.25 and magnetic saturation values were obtained from data sets from textbooks[211] for iron-oxide and previous investigations of chrome steel beads[153]. It should be noted that the numerical validity of these results is dependent on the accuracy of model assumptions of magnetic components reaching their saturation magnetisation at 9.4 T. Such assumptions are valid based on the well described hysteresis behaviours of iron-oxide particles and chrome steel beads[211,161].

5.2.3 Movement in weak agar

Sample preparation:

0.5 and 1 mm diameter chrome steel spheres (AISI 52100) were placed in a 22 x 25 x 25 mm container filled with 0.125% agar (Sigma Aldrich®). Agar was prepared by adding 0.5 g to 100 ml of distilled water, heated until boiling, diluted to 0.125% with 300 mL of distilled water, poured into phantom and left at room temperature to set. The sample was then placed inside the 39 mm Rapid RF coil and a constant temperature of 22°C was maintained throughout the experiment using a warm air blower controlled with thermometer feedback.

Magnetic resonance targeting:

Preclinical scanner: Gradient strength = 100-500 mT/m with a duty cycle = 22% (ON/OFF of 2/7 ms) and number of loops = 500. For each sample, the total targeting on-time was calculated by multiplying the total number of loops by the duration of one targeting sequence. Experiments were performed using a 9.4 T Varian Inova scanner (Varian, Santa Clara, CA).

Clinical scanner: Gradient strength = 100-300 mT/m with a duty cycle = 15% (ON/OFF of 15/85 ms) and number of loops = 2. Experiments were performed using a 3 T Siemens scanner

(Germany, Berlin) and a Magnetom Skyra Connectom (Siemens, Germany) gradient set at the CUBRIC centre in Cardiff (Prof Derek Jones).

MR imaging:

Figure 5.1A shows the susceptibility effect introduced into the GE image by a 0.5 mm seed. I used in-house MATLAB image analysis to convert the acquired GE to a binary image (Fig. 5.1B). The distance moved between two image acquisitions was then calculated by subtracting the pre from the post movement image (Fig. 5.1C). The gradient echo imaging parameters were: FOV = 25.6 x 25.6 x 2 mm, data matrix = 64x64, TR = 15.428 ms, TE = 0.69 ms. Movement was always measured in the phase encoding direction (perpendicular to B_0).

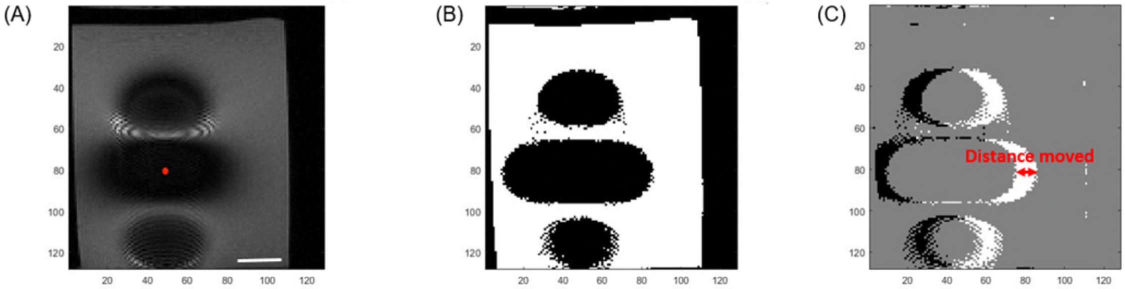

Figure 5.1- MR image of a 0.5 mm magnetic seed. (A) Gradient echo image of the seed in agar sample. Approximate location of the seed is indicated using the red circle. Large susceptibility effect apparent in the image as a result of the magnetic distortion produced by the seed. Scale bar 5 mm. (B) Binary image of the same 0.5 mm seed produced using Otsu's method in MATLAB. (C) Image produced by subtracting the binary image before the movement from the after image. Distance moved measured as indicated in the figure.

5.2.4 Movement in viscous media

Magnetic resonance targeting:

To demonstrate movement of magnetic particle using MRI gradients, a 2 mm chrome steel seed was inserted in a 22 x 22 x 25 mm cubic box containing golden syrup (Lyle's). A gradient strength = 500 mT/m was applied with duty cycle = 22% (ON/OFF of 2/7 or 20/70 ms) and number of loops = 500-2000. Total targeting on-time was calculated by multiplying the total number of loops by the duration of one targeting sequence.

MR imaging and movement detection:

Prior to insertion of magnetic seed, MRI images were acquired from the golden syrup container. Samples were positioned in 39 mm Rapid RF coil with temperature monitored and maintained at 22 °C using an air pump feedback control system. A layer of water was added above the viscous medium to provide MR signal. T_2-weighted images were acquired before insertion of the magnetic seed using fast spin echo sequence (TR/TE 1000/9 ms, ETL 4, 20x1 mm thick slices, 1 average, data matrix 256^2, FOV = 30 x 30 mm, ≈1 min).

While calculating the binary image allowed quantification of movement for 0.5 mm and 1 mm seeds, such method would not be appropriate for measurements when a larger size seed is used as the signal loss significantly increases with size of the seed. To address this limitation, we employed magnetic signature selective excitation method which was previously developed to image ferromagnetic beads[212].

When a ferromagnetic object is placed in the magnetic field of an MRI system, it is magnetically saturated and acts like a magnetic dipole, which produces significant distortion to the main magnetic field (Fig. 5.2A). Magnetic signature selective excitation works by selecting a region of the surrounding distorted space during a slice-selective RF excitation (Fig. 5.2B). This method detects signal at a selected frequency offset (Foffset) to the bulk signal which is specific only to the magnetic particle. Figure 5.2C shows the simulated change in Larmor frequency caused by a ferromagnetic particle in the XZ plane. The greatest change in frequency occurs closest to the seed surface where the field distortion produced by the seed is strongest. When a particular bandwidth of offset frequencies are chosen, bands of signal are seen on the MRI image occurring each side of the seed (Fig. 5.2B, C). This excited region will act as a signature for locating the object at any point of time. This signature can be projected on three orthogonal directions of space (x,y,z) using a simple 1D projection image (Fig. 5.2D). The 1D projection was obtained by summating each line of pixels in the readout and phase encoding directions from the 2D non slice selective spin echo image to obtain two 1D projections. This method was developed and introduced by Martel group[212]. I implemented this method in my movement studies with the help of my colleague Rebecca Baker.

In order to locate the seed, T_2-weighted images were acquired after each magnetic targeting sequence using selectively excited fast spin echo sequence (TR/TE 500/13.8 ms, ETL 4, Foffset

= -30 kHz, BW = 2 kHz, 1 average, data matrix 128^2, field of view 50 x 35 x 30 mm, ≈1 min). The relative movement of the seed was then calculated from the cross correlation of the 1D projections (of the two positions) and placed in a 2D vector (containing relative positions in the readout and phase encoding directions). The coordinates of the starting point was manually chosen on the pre-acquired T_2-weighted image and the relative position vector was overlaid on the image to produce the movement data presented in section 5.3.4.

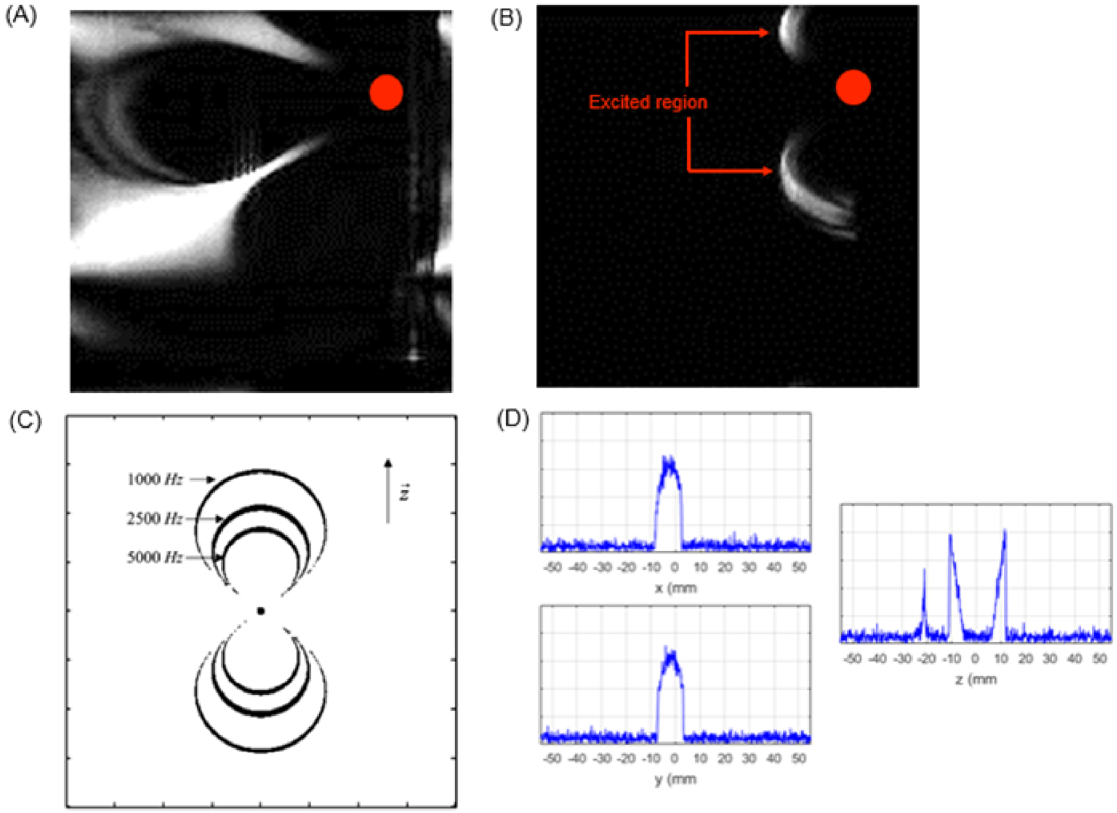

Figure 5.2- Detection of seed position using magnetic signature selective excitation method. (A) Fast spin-echo image of a 2mm seed in agar sample. Magnetic dipoles produced by the field distortion of the seed is clearly visible. (B) Fast spin-echo image of the seed using frequency selective excitation of the off-resonance bands. Selected regions appear as hyper-intense bands. C) Simulation of the spatial distribution of the resonant frequencies of 1, 2.5, and 5 kHz. Figure adapted from[212]. (D) 1D projection of the excited regions on three orthogonal directions of space (x,y,z).

5.2.5 Movement in *ex vivo* brain tissue

Sample preparation:

Whole pig brains were acquired from Meat16, London and were used within 4 days post mortem. Appropriate brain sizes were sectioned and placed in the 22 x 22 x 25 mm container. 0.5 mL PBS solution was added to the sample to rehydrate the brain tissue and the sample was kept in incubator at 37 °C for 1 hour to reach the body temperature.

Magnetic resonance targeting:

Gradient strength = 500mT/m with a duty cycle = 20/70 ms (22%) and number of loops = 500 – 4000. For each sample, the total targeting on-time was calculated by multiplying the total number of loops by the duration of one targeting sequence.

MRI imaging and movement detection:

To produce the movement data presented in section 5.3.5, the MR imaging and seed detection method used in section 5.2.4 was repeated on the brain tissue samples.

5.3 Results

5.3.1 3D movement of magnetic particle using MRI scanner

In order to test the possibility of moving magnetic seeds with MRI system, I investigated 3D movement of a millimetre-scale particle prepared using iron-oxide powder. The first step was to setup an MRI pulse sequence that would enable control over direction, duration and strength of the magnetic gradients used for imaging. The magnetic targeting pulse sequence used for this purpose is shown in figure 5.3 A where the three gradient vectors (Gpe, Gro, Gss) can be adjusted according to the intended direction and strength. I then prepared a phantom containing a millimetre-sized aggregate of iron-oxide powder (Fig 5.3 B, red circle in upper panel) in water and used MRI to image and move the particle in three dimensions. When imaging the seed using a gradient-echo pulse sequence, I observed a susceptibility artefact of about 1.3 cm in diameter (Fig 5.3 B, red circle in lower panel), which is due to the large volume of iron-oxide particles (80% of volume) used in the seed. The seed moved across the 2 cm diameter water sample when gradients were applied in the Z-direction (Fig 5.3 C, upper panel) and X-direction (Fig 5.3 C, middle panel) and outward from the imaging slice when applying gradients in the Y-direction (Fig 5.3 C, lower panel). These observations demonstrated that the imaging gradients of MRI can be used to perform remotely controlled three-dimensional movement of the iron-oxide seed.

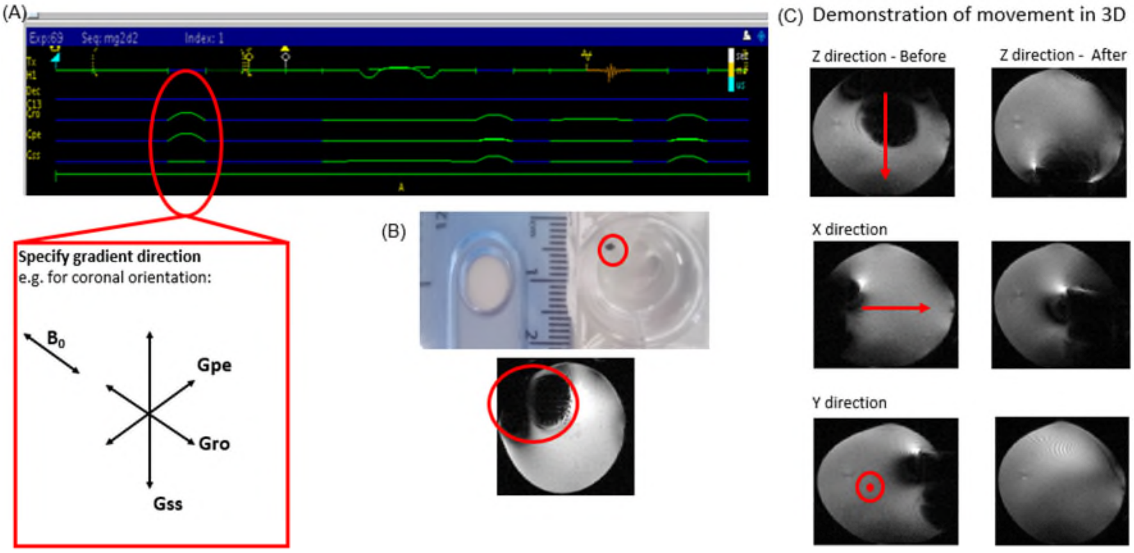

Figure 5.3- Demonstration of 3D movement of millimeter-sized iron-oxide seeds using MRI gradients. (A) Magnetic targeting pulse sequence on MRI software. Three dimensional gradient directions (Gpe,Gro,Gsl) can be controlled for any image orientation. (B) Iron-oxide particle in a water sample and the gradient echo image of the particle. (C) Movement of the iron-oxide particle in three-dimensions using MRI. Location of the particle and the direction of applied force indicated on pre magnetic targeting images and the position of the particle on the same slice visible on the post image.

5.3.2 Effect of particle material and size on magnetic force

After establishing the possibility of movement of magnetic seeds in liquid using MRI, the next step was to test the possibility of movement in viscoelastic media, which are more comparable to tissue in terms of stiffness. The distance moved by the seed depends on the viscosity of the liquid or the Young's modulus of the tissue. Increasing these properties will reduce the likelihood of movement or at least the distances moved by the seed. Therefore, in order to move the same distances through more viscous media or stiffer tissue, the force applied on the seed needs to be increased as much as possible. The magnitude of the applied force depends on the size and magnetisation saturation of the particle as well as the applied gradient strength and duty cycle (equations 2.23-2.25, section 2.3.4). Optimising seed material and size as well as the applied gradient strength is therefore critical for generating enough force on a seed to move it through tissue.

In order to maximise the applied force, I decided to use magnetic seeds made of steel, which were reported to have stronger magnetisation than neodymium inside the MRI scanner's static magnetic field[161]. One suitable material for this purpose is chrome steel, which has a saturation magnetisation of about 2.8-fold higher than iron-oxide powder[211]. Using mathematical calculations (see section 5.2.2), I demonstrated that the magnetic force applied on a 1 mm chrome steel (0.286 mN) is about 5.6-fold higher than that of iron-oxide with the same size (0.0514 mN) at a gradient strength of 500 mT/m (Fig. 5.4 A). These results indicated the significant advantage of chrome steel compared to iron-oxide seeds, which encouraged us to take chrome steel seeds forward for future experiments.

In addition to saturation magnetisation, I performed force calculations on different sizes of chrome steel seeds at different gradient strengths. As magnetic force is proportional to the volume of the particle, size plays an important role on the amount of applied magnetic force. As a result, the magnetic force applied on a 4 mm magnetic seed is 64-times higher than a 1 mm seed (Fig. 5.4 B). However, increasing the size of the seed will produce a larger signal loss in the MR image and may compromise the precision of seed detection and navigation. To this end, I aimed to commence my movement characterisation experiments using smaller seeds (0.5 mm and 1 mm) with a longer-term goal of increasing the size when I perform movement through tissue.

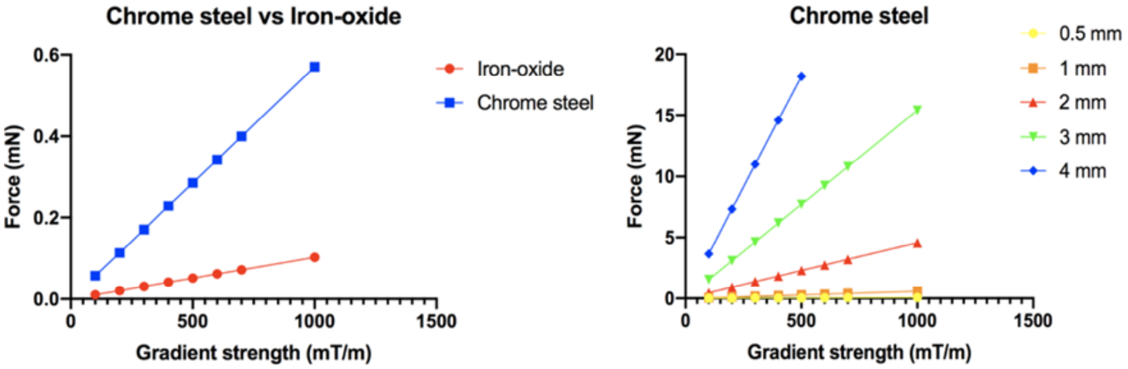

Figure 5.4 - Effect of particle material and size on magnetic propulsion force. (A) Graph indicating the magnetic propulsion force of the MRI system on chrome steel and Iron-oxide seeds of the same size at different gradient strengths. Results shows notable effect of material and magnetic saturation on magnetic force. (B) Graph indicates the force applicable on chrome steel seeds of various sizes at different gradient strengths. Results show notable effect of seed size on applied force. These data are the simulated theoretical magnetic force.

5.3.3 Effect of magnetic field gradient strength and seed size on movement

The ability to control movement of the seed by applying different magnitudes of magnetic force is an important requirement to be investigated. In order to gain insight on the effect of gradient strength and seed size on the movement, I attempted to move two different sizes of the magnetic seed through 0.125% agar using different gradient strengths (Fig. 5.5 A). I observed that movement increased with gradient strength and size of the magnetic seed (n=6, *P ≤ 0.05, Fig. 5.5 B). For example, for a 0.5 mm seed, the distance moved by the 300 mT/m gradient strength (1.2 mm ± 0.62) was approximately 2-fold lower than the distance moved (2.4 mm ± 0.51) by 500 mT/m. Similarly, a 3.5-fold difference was observed in the movement of 0.5 mm seed (1.2 mm ± 0.62) compared with a 1 mm seed (4.1 mm ± 0.97) at 300 mT/m gradient strength. These observations demonstrated that displacement of the seed can be controlled with gradient strength and size of the magnetic seed.

In order to demonstrate feasibility and control of movement using a clinical MRI scanner, the experiment was repeated on a 3 mm seed (to maximise chances of movement) using the Connectom (a customized high magnetic gradient set developed for diffusion tensor imaging[154]) system (Fig. 5.5C). Similar to the data acquired using a preclinical system, I observed consistent seed displacements which increased with gradient strength (n=4, *P ≤ 0.05, Fig. 5.5 D). These results indicated possibility of movement of the magnetic seeds in agar using a clinical imaging gradient system.

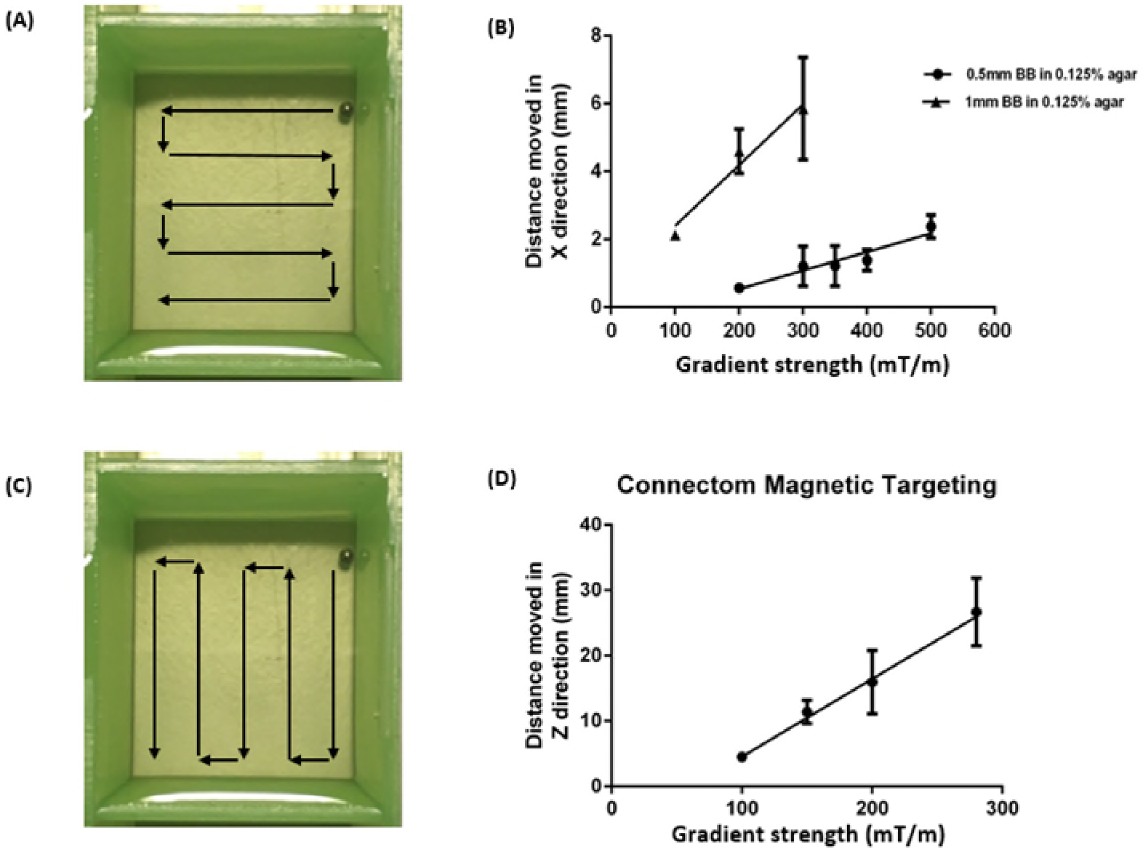

Figure 5.5- Distance moved can be controlled with gradient strength and seed size. (A) The path of movement of 0.5 and 1 mm seeds in agar sample using a preclinical MRI. (B) Effect of the seed size and gradient strength is clearly indicated by the displacement data (n>3). (C) Path of movement of a 3 mm seed in agar sample using a clinical MRI.(D) Control over movement of the seed indicated by displacement data (n>3). Data shown as mean ± SD.

5.3.4 Can we move the seed on a pre-determined path with accuracy?

Previous sections demonstrated the feasibility and control of movement of the chrome steel seeds using both preclinical and clinical MRI gradients. However, the ideal navigation strategy would need to deliver therapy to precise locations within human body. As such, I employed a qualitative approach to determine the degree of accuracy over movement of the seed in a pre-determined path. I used a more concentrated agar solution (0.4%) as a simple, yet comparable (in terms of stiffness), alternative to tissue.

A path consisted of moving 5 mm up along the phantom wall and 5 mm left into the tissue mimicking agar was planned. Unfortunately, this agar phantom had its own drawbacks, acting in a more plastic manner than tissue. Figure 5.6 shows how the seed (green circles) could be moved up parallel with the container and then left into the agar. I observed small movements at first before a single large movement (about 16 mm) occurred taking the seed to the other side of the phantom when the same number of loops was used. Similar results were observed in both samples (Fig 5.6 A,B). The inconsistent movements and jumps of the seed were likely due to the inhomogeneity in viscosity and cracking of the agar as a result of exceeding its yield point when the magnetic force was applied. These observations showed that the concentrated agar would not be a suitable medium to investigate accuracy of movement. I decided to replace the concentrated agar solution with a viscous medium which does not undergo cracking at any applied gradient strength. Golden syrup is a Newtonian fluid which has a viscosity 5 orders of magnitude higher than water [213]. As such, I chose to utilise golden syrup for further movement characterisations.

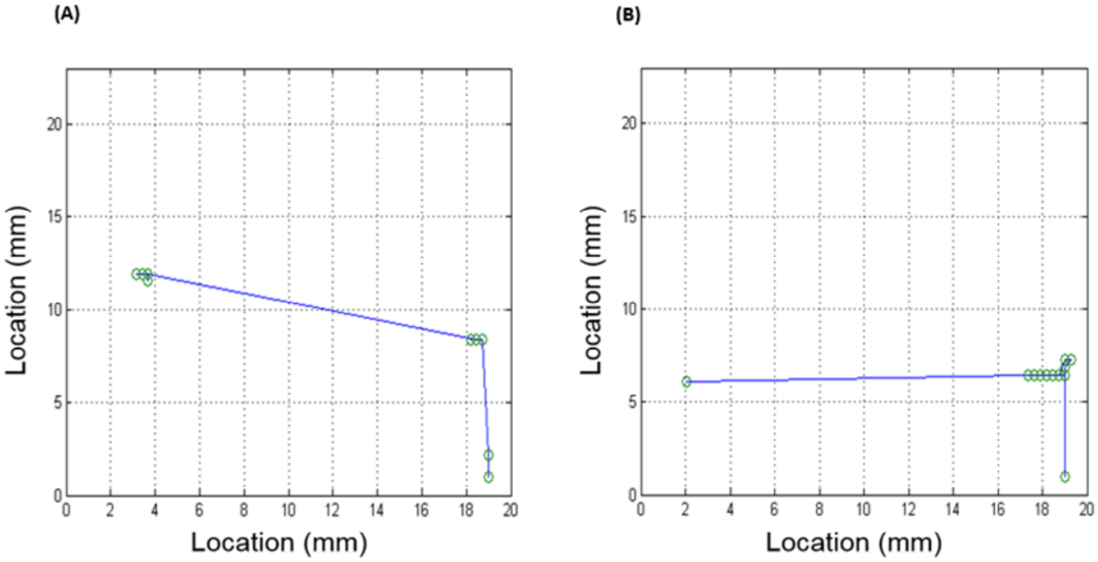

Figure 5.6- Accuracy of movement in 0.4% agar. (A) Movement of a 2 mm seed (green circles) in sample A. Small movements were observed at first followed by a single large jump to the other side of the phantom. (B) Similar results were observed in sample B.

In order to investigate the degree of accuracy over movement of the magnetic seed using MRI gradients, I propelled a 2 mm chrome steel seed in a pre-determined path in golden syrup. The planed path (red line in Fig 5.7A) consisted of a 3 mm movement parallel with the side of the phantom followed by a 7 mm movement to the left and 7 mm movement down (SS direction) towards the centre of the phantom (Fig. 5.7A). I performed movement of the seed along the path in golden syrup using 500 mT/m gradient strength, 22% duty cycle (2/7 ms ON/OFF) and 1000-4000 number of loops (gradient repetitions). This resulted in the seed (yellow sphere) moving 3 mm down, 7 mm to the left, and 7 mm downwards (Fig, 5.7B). As indicated by Figure 5.7B, I observed movements in line with the applied force, delivering consistent distances when the same number of loops were applied. For example, all downward movements were performed using 1000 loops and delivered consistent distances (0.4 mm) along the whole path showing that movement of the seed is precise in both magnitude and direction. After a total targeting duration of 459s, a total movement of 17 mm was observed corresponding to a movement efficiency (i.e. total displacement/total gradient on-time) of about 0.04 mm/s.

To assess the degree of control over movement in a non-linear path, a C-shaped path (Fig. 5.7C) was planned and propelled using the same gradient and duty cycle values. In order to deliver movements using fewer targeting sequences, the 2/7 ms duty cycle ratio was replaced with 20/70 ms while keeping the gradient strength 500 mT/m and changing the number of loops between 500 and 1000. The propelled path by the seed is shown in Figure 5.7D. The seed moved 5 mm to left (along horizontal axis) when left gradients were applied at 1000 loops. The following movements were performed using diagonal gradients (applied by using two directional gradients at once) pointing at angles -22.5°, -45° (anti-clockwise), 45° and 22.5° (clockwise) with respect to the horizontal axis all with 500 number of loops. Finally, the seed was moved 5 mm to the right direction when right gradients were applied at 1000 loops.

In addition to movement, another factor which contributes to the accurate delivery of the seed to the target location in tissue, is the precision of imaging and seed detection. This is particularly important as the information given by the detection sequence about the location of the seed will be used to determine the targeting parameters needed for the movement. Using the slice-selective RF excitation and 1d projection profile (see section 5.2.4) movements as small as 0.27 mm could be detected with MRI. These data demonstrated that it is possible to use MRI to image and guide the seed along a pre-determined path in a reliable and controllable way. Any differences in movement direction would be due to the characteristics of the tissue.

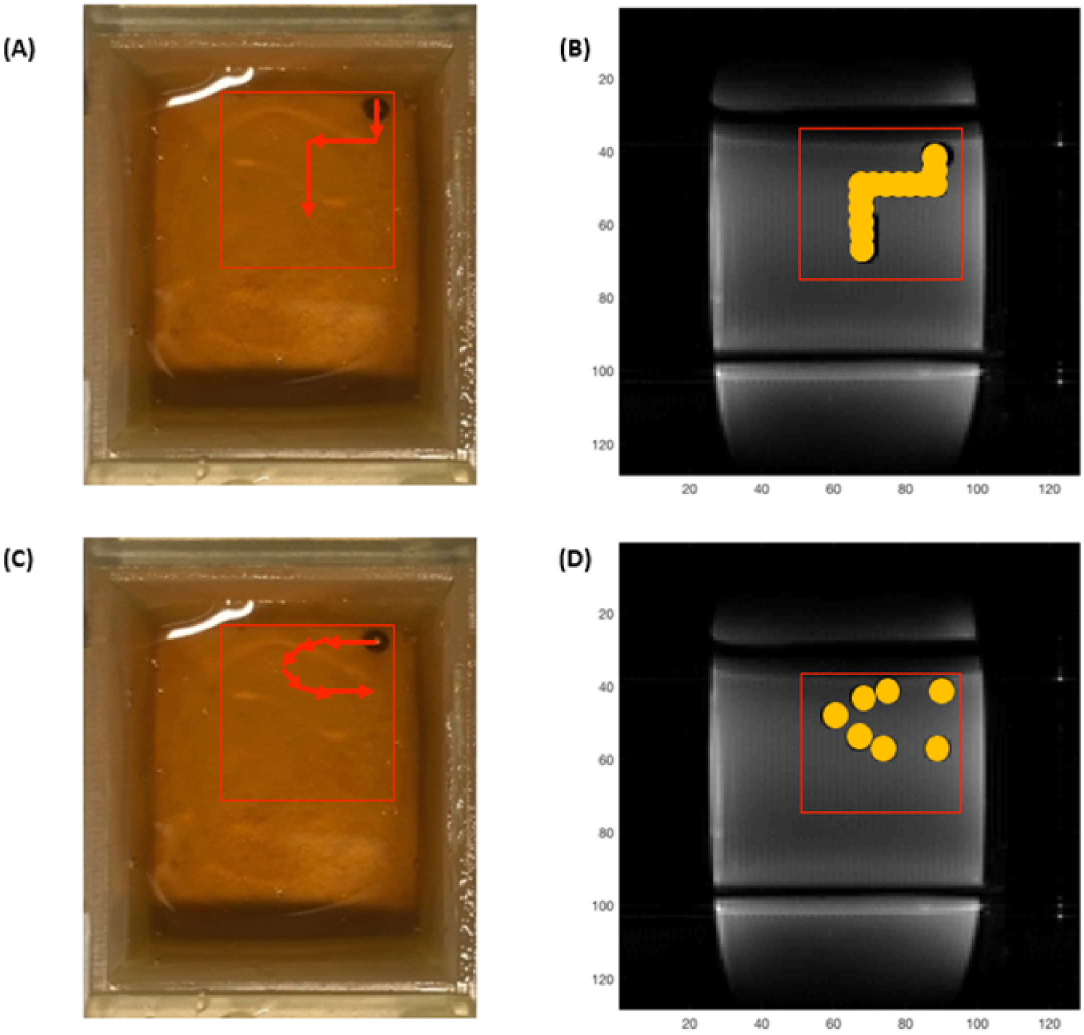

Figure 5.7- Accuracy of movement in golden syrup. (A) The pre-determined path of movement of a 2 mm seed in golden syrup. Arrows show direction of applied gradients. (B) Movement of the seed was demonstrated in a linear path in golden syrup. Yellow circle indicates position of seed after each movement. (C) The experiment was repeated in a pre-determined curved movement paths. (D) Movement of the seed was demonstrated in a C-shaped path in golden syrup.

5.3.5 Can we move the seed in tissue?

My previous investigations demonstrated the efficacy of MRI for controlled movement of millimetre-sized seeds towards a desired location in purely viscous media. However, an important question is whether we can move the seed in tissue. To address this, I investigated movement of 2 mm magnetic seeds in *ex vivo* brain tissue using 500 mT/m gradient strength, 22% duty cycle (20/70 ms ON/OFF) and number of loops (gradient repetitions) in the range of 1000-4000. This was performed in two tissue samples A and B as shown in figure 5.8. The relative movement of the seed was overlaid onto anatomical T_2-weighted images showing grey and white matter boundaries (Fig. 5.8). As shown by figures 5.8A and B, the seed was moved downwards several millimetres initially, then moved into the tissue (left in both samples). In both cases the seed was navigated around an intervening structure (blue arrows) before moving further in tissue by changing the direction of the applied force to 45º diagonal (counterclockwise wrt vertical axis).

In sample A, the seed was moved left and then 45º diagonally (counter-clockwise wrt horizontal axis) toward the middle of the sample. During the diagonal movements, the seed reached a position where no more movement was observed when force was applied. After a total targeting duration of about 1485 seconds, a total movement of 9 mm was observed, corresponding to a movement efficiency of approximately 0.006 mm/s.

In sample B, 45º diagonal movements (counter-clockwise wrt horizontal axis) were performed to move the seed into the middle of the sample. Although all movements were performed using the same number of loops (2000), a large jump (approximately 6 mm) toward the middle occurred during one movement, likely a result of reaching the grey/white matter boundary. This observation emphasises the need for real time imaging so that the amount of force can be altered according to the structure of the tissue surrounding the seed. The results of these experiments demonstrated that a 2 mm seed can be moved in *ex vivo* brain tissue using 500 mT/m gradient strength and 22% duty cycle.

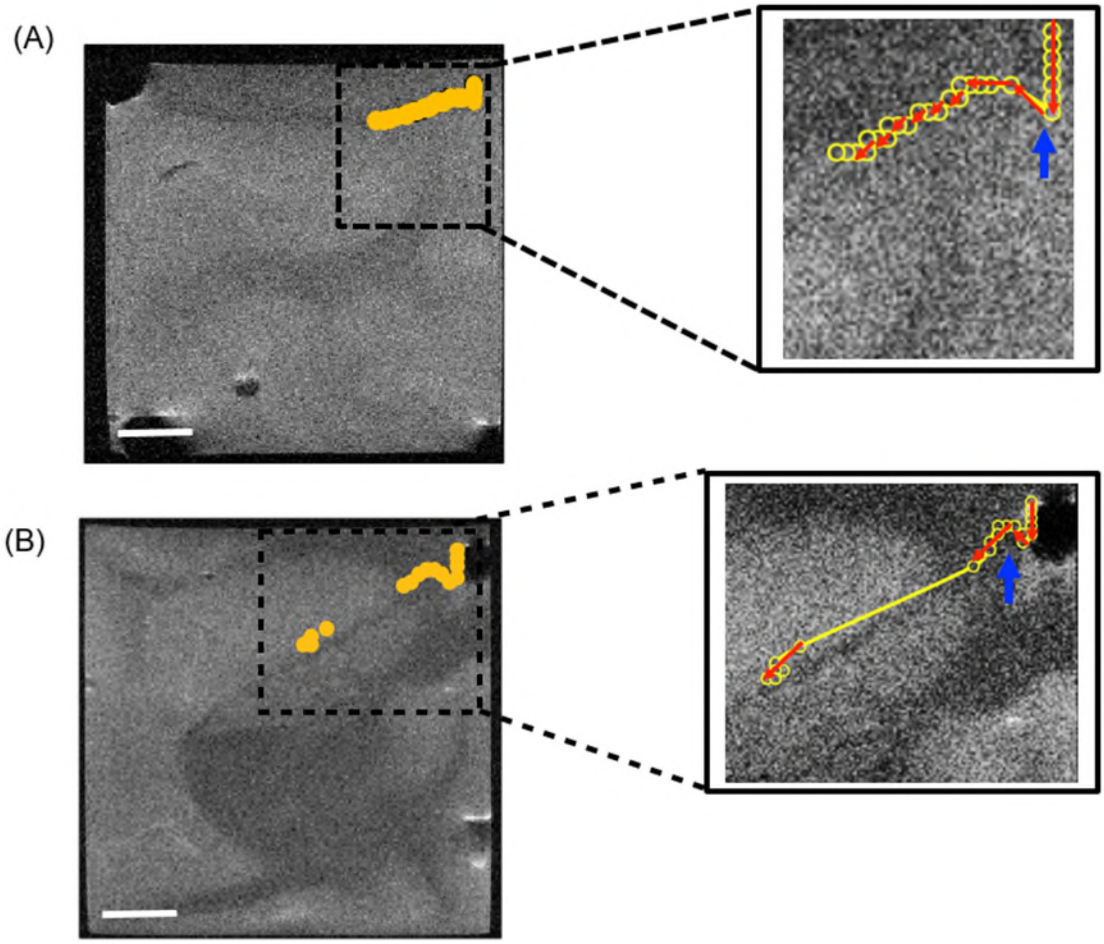

Figure 5.8- Movement of 2 mm seed in *ex vivo* brain tissue. (A) T_2-weighted image of ex-vivo pig brain tissue. Yellow circles indicate the position of a 2 mm seed in the brain after each movement. Circles were made smaller than real size to demonstrate movement more clearly. Red arrows indicate the direction of applied gradients. (B) Experiment repeated in a sample with apparent boundaries between grey/white matter. Clear jump in the movement was observed. Scale bar 5 mm.

5.4 Discussion

This study demonstrates the concept of movement of an untethered magnetic seed through brain tissue using an MRI scanner. Not only a 2 mm chrome steel sphere could be moved through *ex vivo* brain tissue using the magnetic force applied by the imaging gradients, but the position of the sphere could be detected with sub-millimetre precision. The use of the MRI imaging equipment to control the seeds position demonstrated the minimally invasiveness of this method while allowing the surgeon to steer the particle towards a target region. Once in the target location, the seed can be used to ablate, sense or deposit a therapeutic agent. These observations support the concept for an image guided navigation method, which utilises MRI to guide a magnetic particle through tissue. There are four major findings from this study.

- MRI gradients can be used to move millimetre-sized magnetic particles in 3 dimensions.
- Movement can be controlled by changing the strength and direction of the applied gradients.
- Particle moves precisely in line with the applied gradients in Newtonian viscous fluids.
- A 2 mm chrome steel sphere can be moved in *ex vivo* brain tissue using 500 mT/m gradients.

5.4.1 Movement of magnetic seeds using MRI scanner

This chapter investigated the degree of movement control of magnetic seeds using imaging gradient of an MRI system. The results of the movement in a viscous medium demonstrated that the forces applied to the seed using the imaging gradients are consistent and precise in both distance and direction. The seed could be manoeuvred in a pre-determined path towards a target location using the imaging and targeting ability of the MRI scanner. It was previously demonstrated that the seed could be detected with an accuracy of 0.27 mm[214], which means imaging and targeting using MRI can potentially deliver similar accuracy compared to an established focal ablation technology known as Gamma Knife[215] (0.5+/- 0.6 mm accuracy in spherical ablation volume). These data emphasised the potential benefits of the image guided interstitial navigation method proposed in this chapter as an accurate method of delivering treatment to diseased boundaries within the tissue.

5.4.2 Movement in tissue

Previous studies in the field, used rotatable electromagnets to demonstrate movement of a 5 mm x 4.5mm NdFeB cylinder in canine brain tissue in combination with fluoroscopic imaging[2]. In these experiments, no signs of severe haemorrhage to the brain tissue were observed[2], even though the magnetic particle utilised were larger in size compared to the current study. These observations provided preliminary evidence for safety of the procedure in terms of preserving healthy tissue. One of the main advantages of using the MRI system as a magnetic navigation method is the ability to map the structurally sensitive locations of the tissue anatomy and avoiding them in the pre-planned movement path.

The electromagnetic system used in the canine hyperthermia study[2] was capable of delivering magnetic field gradients of 2.6 T/m. Nonetheless, utilising such gradient values would not be possible with any currently available MRI system. While it has been shown that a 1.5 mm steel ball can be moved through the vasculature[207], to date there is no evidence that MRI gradient coils can move magnetic spheres through tissue, in part due to supposedly insufficient forces[161] of conventional MRI scanners. However, the results of these experiments show that using gradient strengths of 500 mT/m and duty cycle of 22%, a 2 mm magnetic seed can be moved through *ex vivo* brain tissue. This is the first demonstration of movement of magnetic particles in tissue using an MRI scanner.

One of the major observations of the present study was the high dependency of the seed movement on the properties of the tissue immediately surrounding the seed. The seed follows a path of least resistance, which was observed to be through grey matter and often parallel to the grey/white matter boundary. In addition, movement stopped at some point along the path while magnetic forces were still being applied. These observations indicate that, with the current forces available some areas of the brain are too dense to move through and must be navigated around. To increase the control over the movement in tissue, the amount of force applied to the seed must be increased. For this there are two options: Optimise the seed and/or optimise the gradients.

As the magnetic force is proportional to the volume of the seed, the most influential option with regard to seed optimisation is to increase the seed size. While chrome steel was shown to be significantly more magnetic in MRI compared with iron-oxide, there are a few metal alloys that have higher magnetic saturation values. Iron-Cobalt alloys are an example which can reach saturation magnetisations of around 1.72×10^{6} Am^{-1} (slightly higher than chrome steel 1.44×10^{6} Am^{-1})[153], however they have limitations for medical applications due to their brittleness and being prone to cracking. Another strategy is to reduce the resistant forces applied on the particle by changing the shape of the seed. Nonetheless, non-spherical objects will rotate to become aligned with the main magnetic field inside the MRI and therefore the range of movement will be restricted. Although optimisations could also be employed to design an optimal shape for the magnetic object to perform minimally invasive surgery, such optimisation would not lead to significant improvements as it has been previously shown that spherical objects encounter only about 10% higher fluid drag force (resistance to movement) compared to the ones with optimal shape[216]. For these reasons, we decided to take 0.5-3 mm sized chrome steel spherical seeds forward for further investigations.

For gradient optimisation, increasing the gradient strength would improve the control over the movement of the seed in denser regions of tissue. Nonetheless, we aimed to keep the gradient strength as low as possible to increase the feasibility of clinical translation. Custom made high amplitude gradient coils are previously developed for magnetic resonance navigation[153] (400 mT/m) and diffusion tensor imaging[154] (300 mT/m). As such, we hypothesised that applying continuous gradients with 100% duty cycle may increase the chance of movement in tissue using gradient amplitude below 500 mT/m. This led to the development of the bespoke imaging gradient system, which is capable of producing continuous gradients at gradient strength equal and below 500 mT/m (see chapter 6).

5.4.3 Efficiency of movement

In addition to control, another important factor in image-guided delivery of magnetic seeds is the efficiency of movement (i.e. movement speed) in tissue, showing that it is possible to deliver therapy within a typical surgical time scale. To move a 3 mm spherical seed through *ex vivo* brain tissue at a speed of 0.67 mm/s, it was previously shown that an average force of 0.07 ± 0.03 N[168] is needed. In our experiments, for a minimum detectable movement of 0.27 mm and a targeting on-time of 40 seconds (including rise time) an effective movement velocity of 0.006 mm/s was observed compared to their 0.66 mm/s. Such low speed of movement is expected as a theoretical force of 0.002 N is calculated for a 2 mm seed using a 500 mT/m strength of pulsed gradients. The ability to generate equivalent gradient strengths continuously would therefore also increase the efficiency of movement. While increasing the seed size to above 4 mm would produce a drastic increase in the applied magnetic force, our restricted imaging volume with our current preclinical MRI system limits seed size to a maximum of 3 mm as the susceptibility artefact becomes larger than the total imaging volume above this size. These considerations provided us with additional reasons for developing a purpose-built imaging gradient coil that is capable of delivering continuous gradients at similar strengths as well as increasing the seed size to 3 mm for movement in tissue. The next chapter of this thesis will report my investigations on movement using the custom-built magnetic targeting gradient coil and larger seed size.

5.5 Conclusion

In this chapter, I have demonstrated the proof of concept of an image guided interstitial navigation strategy, whereby an MRI scanner can be used to guide a magnetic thermoseed into a tumour, which could be destroyed by magnetic heating or delivering chemotherapy. With relatively little modification to existing MRI gradient coils, it is anticipated that they could be transformed into a new class of theranostic device. The results of the pilot studies performed in this chapter provided insight into the high degree of control and accuracy for delivering therapy using MRI. While preliminary data showed possibility of movement in tissue, we aimed to exploit this concept further by optimising the magnetic targeting parameters to achieve more controlled and efficient movement. The next chapter of this thesis will focus on my further investigations with navigation of magnetic seeds using MRI.

6. Optimisation of parameters for navigation of magnetic seeds in tissue

In previous chapters, I have assessed various magnetic designs that can circumvent the rapid fall in magnetic force away from conventional magnets. Chapter 5 demonstrated that by increasing the size of the magnetic particle, the magnetic force generated by an MRI system can be used to produce controlled movement of the particle within tissue. This chapter of my thesis aims to improve the navigation of magnetic seeds using an MRI system by introducing a novel targeting/imaging gradient coil that is capable of producing a high gradient field strength at 100% duty cycle. In this study, I demonstrate the benefits of using continuous gradients (100% duty cycle) in moving chrome steel beads (thermoseeds) in viscous medium and brain tissue. Additionally, I demonstrate that it is possible to move seeds in denser tissues such as liver using this gradient system.

6.1 Introduction

Magnetic resonance targeting relies on the ability of magnetic field gradients generated by MRI gradient coils to induce a steering force on bodies magnetised when immersed in the highly homogenous field of the MRI scanner. Conventional MRI gradient coils are able to switch from 0 to a typical maximum amplitude of around 40 mT/m in 200 µs[146]. However, in the previous chapter it was demonstrated that the gradient strength must be increased about ten-fold to allow tissue penetration of a millimetre-sized magnetic particle. High magnitude gradients can be provided by a separate magnetic targeting gradient coil insert (MTC) (i.e. a gradient coil that is designed to perform magnetic navigation), an imaging gradient coil (IGC), or a combination of both (see section 2.3.3). Previous studies have utilised IGCs to target cells [31,155] while some studies have used MTC inserts to target drug-loaded microparticles[130].

MTC inserts can produce gradient amplitudes up to 450 mT/m and can switch magnetic gradients from zero to maximum amplitude in 350 ms[157]. However, the slew rate for MTC inserts is typically much lower than what can be achieved with the IGCs. Producing fast slew rates is important for intravascular drug-delivery[130] or magnetic catheterisation systems[217] due to the fast directional changes needed in complex vessel geometries. Nevertheless, fast slew rates are not a necessary requirement for interstitial delivery as the magnetic navigation is performed through tissue as opposed to vasculature; making MTC inserts a feasible option for in vivo tissue studies.

While MTC inserts produce desirable gradient amplitudes for magnetic targeting, they are hampered by their lack of ability to acquire images due to their limited slew rates and need to be combined with an imaging insert in order to facilitate a combination of targeting and imaging [157]. Using a high-gradient IGC instead of an MTC for magnetic targeting is attractive, as it exhibits both gradient strengths of hundreds of milli Tesla per meter and the hardware required to perform imaging. As discussed in chapter 5, high amplitude gradient coils are in development and currently used in clinical research for applications such as diffusion tensor imaging, which requires fast gradient switches and gradient amplitudes of 300 mT/m[154,218,219]. Such imaging sequences usually use low duty cycle gradient pulses, thereby allowing a long experiment time without any temperature increase in the coil.

In contrast to imaging applications, MRT requires high-amplitude gradients for a prolonged duration (high duty cycle) and therefore the temperature of the coil may increase to potentially reach a critical threshold[146]. Experiments performed in chapter 5 demonstrated the limited ability of a pulsed-type gradient (22% duty cycle) in terms of control and efficiency of movement of thermoseeds in tissue. However, producing continuous gradients (100% duty cycle) at high amplitude needs large electrical currents that inevitably generate heating that could lead to irreversible damage to the system. As a result, producing systems that can run at high power values for a prolonged period are of considerable importance for MRT. As such, we worked with Tesla Engineering Ltd to develop an IGC insert that is capable of producing high-amplitude gradients (0.5-1.2 T/m) at 100% duty cycle without overheating.

In this study, I specified the requirement of the new IGC insert and used this system to characterise the effect of duty cycle on movement of millimetre-sized magnetic seeds in viscous media and biological tissue. The control and efficiency of the movement was first assessed in viscous and dense media using a range of magnetic targeting parameters. The movement in brain tissue was then tested using the optimised targeting parameters and gradient amplitudes that were previously produced in a clinical setting. Finally, movement of a 3 mm seed was investigated in tissues denser than brain such as liver tissue using 100% duty cycle and 500 mT/m gradient strength.

The aims of this study were as follows:

(i) To investigate the effect of duty cycle on control and efficiency of movement in dense and viscous media.

(ii) To investigate movement of thermoseeds in brain tissue using 100% duty cycle gradients.

(iii) To investigate possibility of movement in liver tissue.

6.2 Materials and methods

This section will provide the experimental methods used to acquire the data presented in section 6.3.

6.2.1 Theory and specifications of the imaging gradient coil

In this chapter, I investigated movement of 2-3 mm seeds using a range of different magnetic targeting parameters of the MRI propulsion pulse sequence. The gradient coil manufactured by Tesla Engineering Ltd is shown in the image below. Relevant parameters for magnetic targeting gradient pulse are also demonstrated.

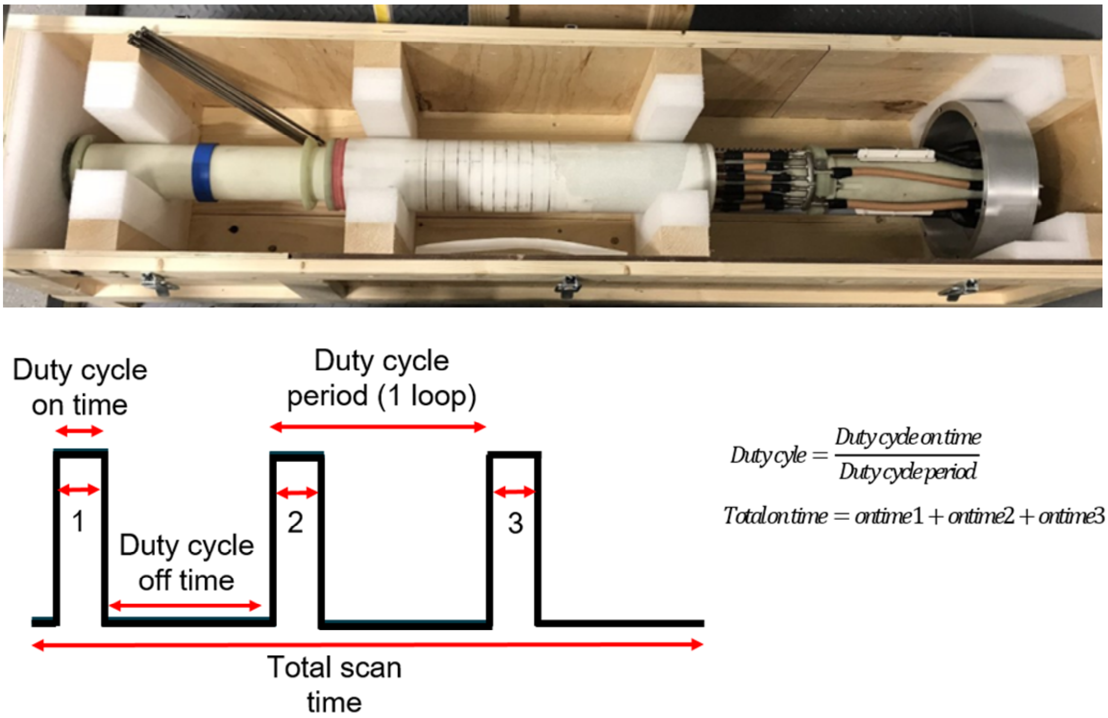

$$\text{Duty cyle} = \frac{\text{Duty cycle on time}}{\text{Duty cycle period}}$$

$$\text{Total on time} = \text{on time}1 + \text{on time}2 + \text{on time}3$$

Figure 6.1- Custom made IGC system. The imaging gradient coil manufactured by Tesla Engineering Ltd (Upper panel). Parameters used during the magnetic resonance targeting experiments (Lower panel).

Specifications of Tesla T118_60 gradient coil:

Dimensions and weight:

Internal diameter 60mm±1mm

External diameter ≤118mm

Length of gradient module 786 mm

Weight <75kg

Safe operating conditions: Peak operating voltage ≤400V, Peak current ≤200A

X axis: Efficiency: 6596 μT/m/A ±5%, Rise-time (0-98%): 19μs±5% (X axis alone), 65A steady state DC current, peak gradient strength: 1319 mT/m±5%

Y axis: Efficiency: 5766 μT/m/A ±5%, Rise-time (0-98%): 21μs±5% (Y axis alone), 89A steady state DC current, peak gradient strength: 1153 mT/m±5%.

Z axis: Efficiency: 6655 μT/m/A ±5%, Rise-time (0-98%):17μs±5% (Z axis alone), 200A steady state DC current. Peak gradient strength: 1331 mT/m±5%

All three axes together ≤56A Steady state DC current

Temperature, as measured by PT100 sensors ≤70ºC

A standard set of power supply and gradient amplifier (Copley Controls Corp.), which was used for Agilent imaging system was used to operate this gradient coil. The Tesla gradient coil is capable of producing 1200 mT/m, 500 mT/m and 500 mT/m amplitudes at 100% duty cycle in the Z, Y and X directions respectively. However, due to hardware limitations of the Agilent system (the MRI scanner), only a maximum of 7 s duration gradient pulse can be applied at a maximum gradient strength of 500 mT/m. As such, in order to apply long gradient pulses of tens of seconds' duration, multiple 5 s pulses were applied (multiple loops). As the rise-time (i.e. duration of gradient ramp) of gradients applied by this system is negligible (< 21 μs) multiple pulses with 100% duty cycle were approximated to be a single square pulse.

6.2.2 Movement in golden syrup

Magnetic resonance targeting:

To optimise movement of the seed, three different variables were investigated.

i) Duty cycle: Total scan time was kept constant and the duty cycle (total on-time) was changed. Gradient strength = 400 mT/m, Duty cycle: 22%: 2ms ON/7ms OFF, 50%: 2ms ON/2ms OFF, 100%: 2ms ON/0ms OFF; Loops: 2000, 4500, 9000; Total on-time: 4 s, 9 s, 18 s; Scan time: 18 s.

ii) Duty cycle on-time: Total on-time was kept constant and the duty cycle on-time was changed, Gradient strength = 400 mT/m, Duty cycle: 50%: 100ms ON/100ms OFF, 67%: 200ms ON/100ms OFF, 83%: 500ms ON/100ms OFF, 90%: 1s ON/100ms OFF, 95%: 2s ON/100ms OFF; Loops: 100, 50, 20, 10, 5; Total on-time: 10 s; Scan time: 10 s.

iii) Seed material: Duty cycle was kept constant and the gradient strength was changed for a 2 mm Neodymium bead (N42 grade) and a 2 mm chrome steel seed (AISI 52100), Gradient strength= 50 mT/m, 100 mT/m, 150 mT/m, 200 mT/m, 250 mT/m, 300 mT/m, 350 mT/m, 400 mT/m; Duty cycle: 100%: 1s ON/0 OFF; Loops: 10; Total on-time: 10 s; Scan time: 10 s.

MR imaging and movement detection:

Samples were positioned in a 39 mm Rapid RF coil with temperature monitored and maintained at 22 °C with an air pump feedback control system. A layer of water was added above the viscous medium to provide MR signal. To locate the seed, a 1D projection was obtained by summating each line of pixels in the readout and phase encoding directions from a 2D non-slice selective (off resonance frequency) spin echo image to obtain two 1D projections. Parameters for the spin echo sequence were: TR/TE 500/13.8 ms, ETL 4, Foffset = -30 kHz, BW = 2 kHz, 1 average, data matrix 128^2, field of view 50x35x30 mm, ≈1 min. The relative movement of the seed was then calculated by cross correlating the 1D projections of pre and post movement positions (see section 5.2.4).

6.2.3 Movement in margarine

Magnetic resonance targeting:

To test the advantage of continuous gradients over pulsed gradients (hammering action) on movement in dense media, I performed movement of a 2 mm chrome steel seed in margarine (Flora, Unilever UK) inside the 22x22x25 mm box. The temperature inside the sample was controlled and monitored using a temperature regulating system and a rectal probe respectively (SA instruments Inc.).

In these experiments the total on-time was kept constant while changing the duty cycle ratio (two different duty cycle off-times). For 100% duty cycle, Gradient strength = 400 mT/m; Duty cycle:

2ms ON/0ms OFF; Loops: 9000; Total on-time= 18 s; Scan time= 18 s. For 22% duty cycle, Gradient strength = 400 mT/m; Duty cycle: 2ms ON/7ms OFF; Loops: 9000; Total on-time= 18 s; Scan time = 81 s. The temperature of the sample was increased from 30 °C to 35 °C in steps of 1 °C during the experiment.

MR imaging and movement detection:

Samples were positioned in a 39 mm Rapid RF coil with the temperature monitored and controlled using an air pump feedback control system. To locate the seed, the cross correlation method explained in section 6.2.2 was used.

6.2.4 Movement in *ex vivo* brain tissue

Sample preparation:

Whole pig brains were acquired from Meat16, London and were used within 4 days post mortem. To investigate movement over a longer distance, a larger tissue phantom (35x60x12 mm) compared with experiments conducted in chapter 5 was prepared. Appropriate brain sizes were sectioned and placed in the container. 0.5 mL PBS solution was added to the sample to rehydrate the brain tissue and the sample was kept in an incubator at 37 °C for 1 hour, to reach body temperature. The brain tissue sample containing the 3 mm seed was inserted vertically into the gradient coil inside the MRI scanner, with the long axis of the sample along the MRI bore (Z direction).

In order to prevent movement of the seed while inserting the sample into the scanner, I filled the cavity through which the seed was inserted to the sample with margarine to avoid the seed being pulled by the fringe field of the MRI scanner when the sample is inserted into the bore. This method successfully kept the seed at the insertion point when the sample was placed into the MRI scanner. This was performed for samples B-E.

Magnetic resonance targeting:

Movement of a 3 mm seed was investigated using gradients strengths of 300-400 mT/m along the Y-direction. In these experiments, gradient strength and duty cycle ratio were kept constant along the Y-direction while changing the number of loops (total on-time). Five samples were investigated with the following targeting parameters.

Sample A) Gradient strength: Z= 400 mT/m, X=500 mT/m, Y= 400 mT/m; Duty cycle: 5s ON/0s OFF; Loops: 1-14; Total on-time: 5-70 s; Scan time: 5-70 s.

Sample B) Gradient strength; Y= 400 mT/m; Duty cycle: 5s ON/0s OFF; Loops: 1-20; Total on-time= 5-100 s; Scan time: 5-100 s.

Sample C) Gradient strength; Y= 400 mT/m; Duty cycle: 5s ON/0s OFF; Loops: 4-20; Total on-time= 20-100 s; Scan time: 20-100 s.

Sample D) Gradient strength; Y= 300 mT/m; Duty cycle: 5s ON/0s OFF; Loops: 4,8; Total on-time= 20,40 s; Scan time: 20,40 s.

Sample E) Gradient strength; Y= 300 mT/m; Duty cycle: 5s ON/0s OFF; Loops: 4-24; Total on-time= 20-120 s; Scan time: 20-120 s.

MRI imaging and movement detection:

Prior to insertion of magnetic seeds, MRI images were acquired to provide insight into the structure of the brain tissue. Samples were positioned in a 39 mm Rapid RF coil with temperature monitored and maintained at 37 °C, using an air pump feedback control system. T_2-weighted images were acquired before insertion of the magnetic seed using a fast spin echo sequence (TR/TE 1000/9 ms, ETL 4, 20x1 mm thick slices, 1 average, data matrix 256^2, field of view 40 x 40 mm, ≈1 min). In sample E, a T_2-weighted was also acquired after removal of the seed from the sample.

Once the seed was inserted in the brain tissue, a 1D projection was obtained by summating each line of pixels in the readout and phase encoding directions from a 2D non-slice selective spin echo image to obtain two 1D projections. Parameters for the spin echo sequence were: TR/TE 500/13.8 ms, ETL 4, Foffset = -30 kHz, BW = 2 kHz, 1 average, data matrix 128^2, field of view 50x35x30 mm, ≈1 min. The cross-correlation method used for detecting movement in golden syrup and margarine was altered for *ex vivo* tissue due to the incomplete signal signature from the seed near the edge of the sample. To detect relative positions in *ex vivo* brain tissue, the first point that reached half the maximum signal intensity in each 1D projection was found and placed in a 2D vector (for the readout and phase encoding directions individually). The coordinates of the starting point were manually chosen on the pre-acquired T_2-weighted image and the relative position vector was overlaid on the image with respect to the starting point to produce the movement data presented in section 6.3.4.

6.2.5 Movement in *ex vivo* liver tissue

Sample preparation:

Ex vivo sheep liver tissue was obtained from butchers and movement experiments were carried out in tissue samples, 3-4 days after the animal was culled. Appropriate liver tissue sizes were sectioned and placed in the 35 x 60 x 12 mm container. 0.5 mL PBS solution was added to the sample to rehydrate the liver tissue and the sample was kept in an incubator at 37 °C for 1 hour to reach body temperature

Magnetic resonance targeting:

Movement of a 3 mm seed through liver tissue was investigated using a gradient strength of 500 mT/m along the X-direction. In these experiments, gradient strength and duty cycle ratio were kept constant along the X-direction while changing the number of loops (total on-time). Three samples were investigated with the following targeting parameters.

Sample A) Gradient strength: X=500 mT/m; Duty cycle: 5s ON/0s OFF; Loops: 10,12,14; On-time: 50, 60, 70 s; scan time: 50, 60, 70 s.

Sample B) Gradient strength: X=500 mT/m; Duty cycle: 5s ON/0s OFF; Loops: 12,14; On-time: 60, 70 s; scan time: 60, 70 s.

Sample C) Gradient strength: X=500 mT/m; Duty cycle: 5s ON/0s OFF; Loops: 12,14; On-time: 60, 70 s; scan time: 60, 70 s.

MRI imaging and movement detection:

To detect relative positions in *ex vivo* liver tissue, I repeated the same method used for brain experiments (section 6.2.4). As individual movements were undetectable (< 0.3 mm imaging resolution), I used the relative distance between the first and last positions to work out the total distance moved by the seed. I then overlaid these data on the pre-acquired T_2-weighted images of the tissue sample to produce the movement data presented in section 6.3.6.

6.3 Results

6.3.1 Optimisation of seed movement using MRI

The results presented in chapter 5 indicated that in order to increase the control over the seed movement in tissue, the magnitude of applied magnetic force must be increased. To optimise movement of the seed, I performed further investigations on parameters which influence magnetic steering force on the seed. As shown in equations 2.23-2.25 (section 2.3.4), magnetic force is dependent on volume and material (saturation magnetisation) of the seed as well as the strength and duty cycle of the applied magnetic field gradients. The effect of the seed size and gradient strength was demonstrated empirically in experiments presented in chapter 5 (section 5.3.3). As such, I decided to investigate the effect of duty cycle and seed material on movement of seeds in golden syrup using our custom made IGC system (see methods section 6.2.1).

Investigating parameters individually:

Duty cycle: The effect of duty cycle on seed movement has never been investigated in the past. To test this, I performed movement of a 2 mm chrome steel seed using gradient strength of 400 mT/m and three different duty cycles (22% : 2/7 ms ON/OFF, 50% : 2/2 ms ON/OFF, 100% : 2/0 ms ON/OFF), which would lead to total gradient on-times of 4,9 and 18 s respectively. The total targeting scan time was kept constant at 18 s for all experiments.

Linear regression analysis demonstrated significance deviation from zero and a linear relation between duty cycle and movement (n=6, ***$P \leq 0.0001$, $R^2 = 0.9690$, Fig. 6.2 A), which is consistent with equations 2.23-2.25.

Duty cycle on-time: The next question was whether continuous gradients (duty cycle = 100%) would produce more movement compared with pulsed gradients (duty cycle < 100%) with the same total on-time. To address this question, I used a constant total targeting on-time of 10 s and duty cycle off-time of 100 ms, and changed the duty cycle on-time in the range of 0.1-2 s (100-5 number of loops). As the duty cycle on-time increases, fewer off-time periods are introduced within the targeting period, which results in more continuous gradients.

I observed an increasing trend of movement with increasing duty cycle on-time (Fig. 6.2 B). A significant difference was observed in movement between 2 and 0.1 s (n=6, $^{**}P \leq 0.025$, Fig. 6.2 B) and movement using 2 and 0.2 s on-times (n=6, $^{**}P \leq 0.025$, Fig. 6.2 B). These results demonstrated that continuous gradients provide more movement than pulsed gradients.

Seed material: The last parameter investigated in this section was the seed material. To test the degree of magnetisation of chrome steel seeds in MRI, I decided to compare movement of these seeds with spherical permanent magnets (Neodymium grade N42) of the same size. I performed movement experiments of 2 mm chrome steel and Neodymium seeds using continous gradients of different stregnths (50 – 400 mT/m).

When moving chrome steel seeds, a linear relation between gradient strength and movement was observed (n=6, $^{***}P \leq 0.0001$, $R^2 = 0.9176$, Fig. 6.2 C). Movements were precise with a maximum standard deviation of 0.59 mm when using 400 mT/m. When repeated using the Neodymium seed, movement increased with gradient strength (n=6, $^{***}P \leq 0.0001$, $R^2 = 0.9478$, Fig. 6.2 C). Although no statistical difference was observed, the slope of the line produced by the movement of chrome steel was 1.5-fold higher than the corresponding parameter for Neodymium. These data provided more confidence in the chrome steel seeds.

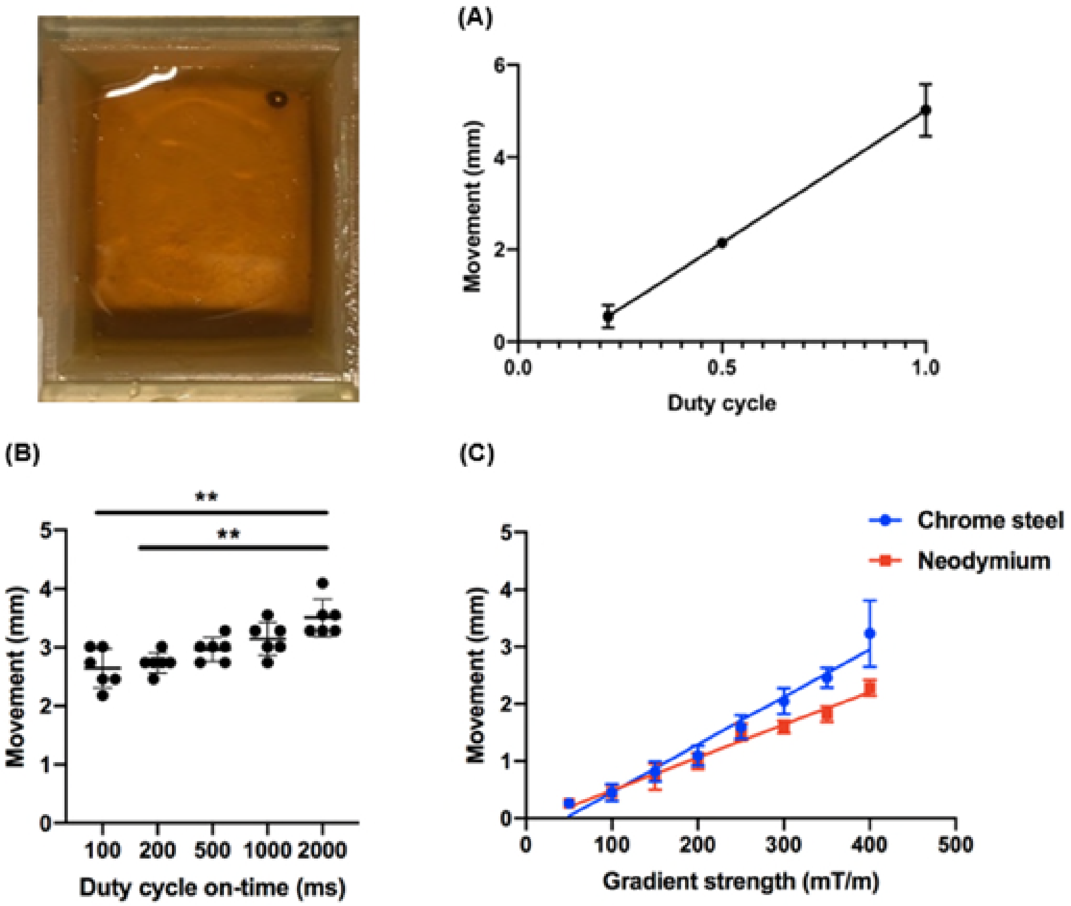

Figure 6.2- Optimisation of seed movement. (A) Movement is linearly dependent on the duty cycle (n=6, ***P ≤ 0.0001, $R^2 = 0.9690$). (B) Continuous gradients produce more movement than pulsed gradients when total on-time is constant (**P ≤ 0.025, n=6). (C) Movement of a chrome steel seed vs movement of a Neodymium seed at different gradient strengths. Data shown as mean ± SD.

6.3.2 Continuous gradients vs pulsed gradients in dense media

My investigations in viscous media (golden syrup) provided evidence for the advantage of continuous gradients (100% duty cycle) compared with pulsed gradients. However, one important question is whether continuous gradients facilitate more movement through dense (and viscoelastic) media compared with pulsed gradients (i.e. hammering action). To address this question, I used margarine, as the viscoelastic properties were found to be dependent on temperature[220–222] due to the amount of crystallised fat.

I performed movement experiments in margarine using a 2 mm seed and two duty cycles (100% and 22%) with the same gradient strength (400 mT/m) and total on-time (18 s) while increasing the temperature of the sample at steps of 1°C. No movement was observed at either duty cycles up to a temperature of 34°C (Fig 6.3). At 34°C, the seed moved with consistent displacements each time 100% duty cycle was applied, while no movement was observed for the 22% duty cycle (n=6, **P ≤ 0.025, Fig. 6.3), indicating the importance of continuous (as opposed to pulsed) forces on the seed. When the temperature was increased to 35°C, inconsistent movements (i.e. large jumps) were observed at both duty cycle values, likely as a result of the transition of the medium from a solid into a liquid phase at this temperature[223].

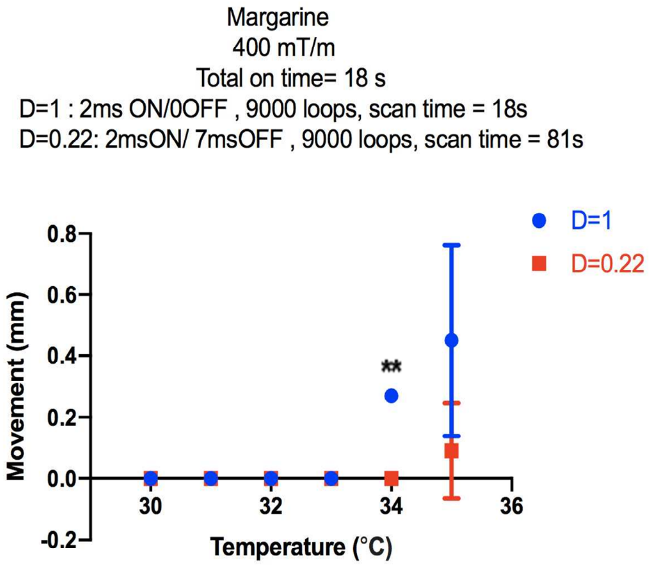

Figure 6.3- Effect of duty cycle on movement of the seed in margarine. Continuous gradients (100% duty cycle) increase movement of a 2 mm seed at 34 degrees Celsius in margarine compared with 22% duty cycle (**P ≤ 0.025, n=6). Data shown as mean ± SD.

6.3.3 Can we move the seed in brain tissue using gradients lower than 500 mT/m?

In chapter 5 it was demonstrated that a 2 mm seed can be moved in *ex vivo* brain tissue using pulsed gradients of 500 mT/m amplitude. It was also shown in chapter 5 that using a larger seed size plays an important role on increasing the amount of force applied on the seed. In addition to these observations, the results of optimisation experiments in this chapter demonstrated improvement in movement of the seed in dense media when continuous gradients are used as opposed to pulsed gradients. As such, the next step was to test whether combining the benefits of continuous gradients and increasing seed size would allow movement of the seed in brain tissue using gradient strengths that are closer to clinical settings.

To address this question, I performed movement of a 3 mm chrome steel seed in *ex vivo* pig brain tissue using continuous gradients of strengths 300-400 mT/m along a single direction (Y-direction). The data presented below describes the results of the movement experiments carried out using 400 mT/m (samples A-C) and 300 mT/m (samples D, E).

Investigating samples individually:

Sample A: Movement of the seed along the Y-direction was started from the position indicated in figure 6.4 A (red arrow). Consistent movements were observed (0.4-0.8 mm) through both grey and white matter tissue for total on-times < 70 s. When the total on-time was increased to 70 s, larger displacements was observed (2-10 mm). After a total targeting on-time of 1085 s, a total movement of 31 mm was performed, corresponding to a movement efficiency (i.e. total displacement/total on-time) of approximately 0.029 mm/s.

Sample B: After applying the first magnetic targeting sequence, the seed moved all the way through the grey matter into the white matter tissue (6.2 mm movement, Fig. 6.4 B, blue arrow). The following movements in white matter were in the range of 0 – 1.5 mm, and increasing the total on-time did not lead to increased displacements (Fig. 6.4 B, red arrow). The movement efficiency in sample B was 0.007 mm/s.

Sample C: After applying the first magnetic targeting sequence, the seed moved all the way through the grey matter into the white matter tissue (5 mm movement, Fig. 6.4 C, blue arrow). The following movements in white matter were in the range of 0 - 0.3 mm, and increasing the total on-time did not lead to increased displacements (Fig. 6.4 C, red arrow). The movement efficiency in sample C was 0.005 mm/s.

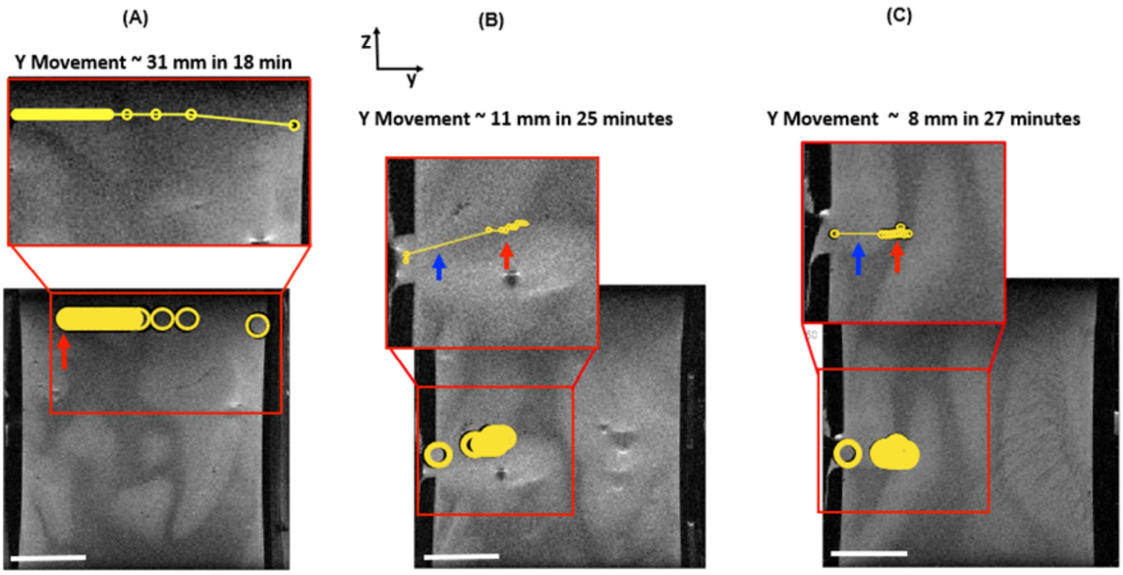

Figure 6.4- Movement of a 3 mm seed in *ex vivo* brain tissue using 400 mT/m. Movement of the seed along the Y-direction overlaid on T_2-weighted image of *ex vivo* pig brain tissue in samples A-C. Yellow circles indicate the position of a 3 mm seed after each movement; scale bars 10 mm.

Previous part provided evidence that a 3 mm seed can be moved in brain tissue using 400 mT/m gradient strength and 100% duty cycle. The next question that I aimed to address was whether the 3 mm seed can be moved using 300 mT/m gradient strength which was previously produced by the connectome gradient coil[154]. To assess this, I repeated the *ex vivo* pig's brain experiments in samples D and E.

Investigating these samples:

Sample D: Movements in the rage of 0.3 – 5.6 mm were observed mostly through grey matter tissue (Fig 6.5 A, blue arrow). The movement efficiency was measured to be 0.057 mm/s in this sample along the Y-direction. To test the possibility of movement in another direction, I carried out the movement along the Z-direction. After applying only two movement sequences, the seed moved all the way through the brain tissue (26 mm upwards, Fig. 6.5 A, red arrow).

Sample E: After applying the first magnetic targeting sequence, the seed moved all the way through the grey matter into the white matter tissue (13 mm movement, Fig. 6.5 B, blue arrow). The following movements in white matter were in the range of 0 - 0.3 mm, and increasing the total on-time did not lead to increased displacements (Fig. 6.5 B, red arrow). The movement efficiency in sample E was 0.007 mm/s.

To investigate movement of the seed through a pre-made path in tissue, gradients were applied in the negative Y-direction to take the seed back to the insertion point in sample E (Fig. 6.5 B, green arrow). After applying one magnetic targeting sequence, the seed moved approximately 17 mm in the negative Y-direction through the premade path in the brain tissue. Post magnetic targeting images from the brain sample, confirmed the tract made through the tissue during positive and negative Y-direction movements (Fig. 6.5 C, red arrow).

These data provided experimental evidence that increasing the size of the seed and applying continuous gradients can produce movement of the seed in *ex vivo* brain tissue when using 300-400 mT/m gradient strengths.

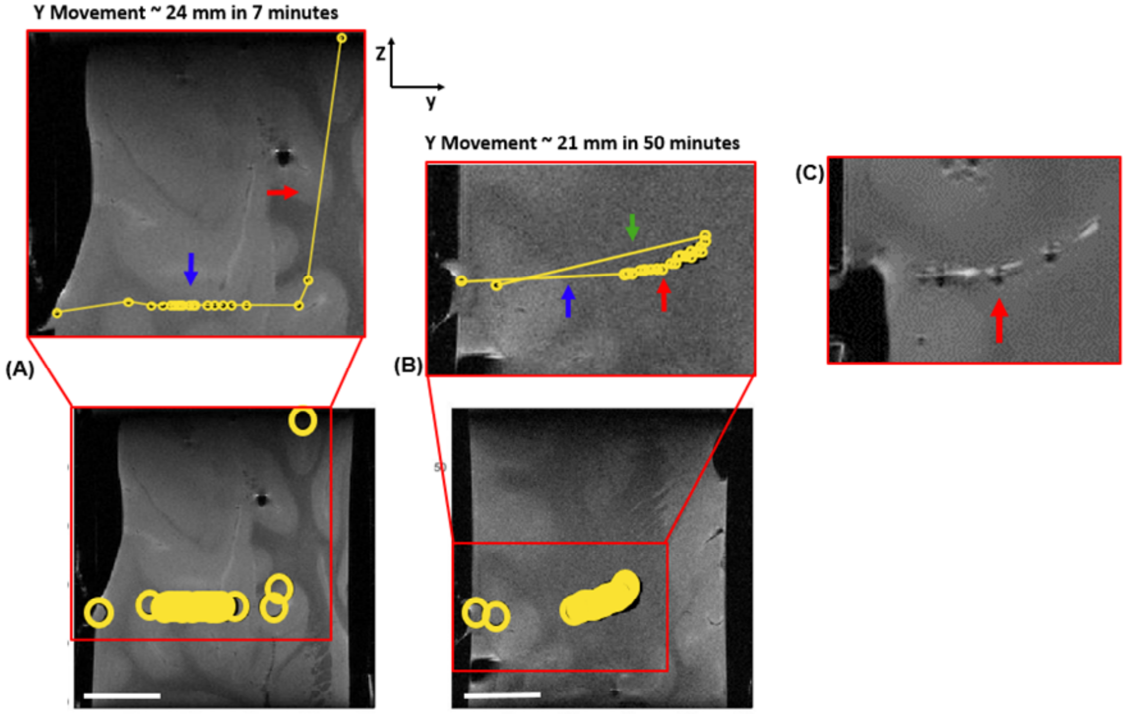

Figure 6.5- Movement of a 3 mm seed in *ex vivo* brain tissue using 300 mT/m. (A) Movement of the seed along Y and Z directions overlaid on T_2-weighted image of ex-vivo pig brain tissue in sample D. Yellow circles in lower panel indicate the position of a 3 mm seed after each movement. Upper panel shows the precise location of the seed within tissue after each movement; scale bar 10 mm. (B) Movement of the seed in sample E. (C) Post targeting T_2-weighted image of *ex vivo* pig brain tissue in sample E where the tract of movement of the seed is visible within the tissue.

6.3.4 Control over movement in brain tissue

The ability to guide the magnetic seed along a pre-determined path in tissue requires high degree of control on the direction and displacement of the seed movement. As such, I used the brain movement data demonstrated in previous section to measure the degree of control on movement of a 3 mm magnetic seed using continuous gradients.

To test the control over movement in terms of direction, I measured the displacement of the seed along the Z-direction while Y gradients were applied for movement. My observations indicated that total displacements in Z-direction (deviation from applied gradients) were 10.9 ± 7.3% (mean ± SD) of the total displacement in the Y-direction when magnetic targeting gradients were applied in the Y-direction. To assess the control over movement in terms of displacement, I measured the number of outliers in the displacement data and the number of movements which were too small to be detected. Only 5.2 ± 3.27% of movements were outliers (large jumps in displacement), while 37.4 ± 31.4% of the magnetic targeting gradients did not lead to movement or displacements were smaller than the detection resolution (< 0.27 mm [observed in white matter]).

Finally, the average movement efficiency of a 3 mm seed was measured to be 0.019 ± 0.018 mm/s in *ex vivo* brain tissue using gradient strengths that have been produced in a clinical scanner[130,154]. Despite the degree of variability in different tissue samples, these data demonstrated that not only movement is possible in brain tissue using gradient strengths lower than 500 mT/m, but also position of the seed can be reasonably controlled both in terms of direction and displacement of movement.

6.3.5 Can we move a 3 mm seed in liver tissue?

My previous investigations explored movement through brain tissue. However, another important question is whether we can move the magnetic seed through denser tissues than brain. To answer this question, I decided to test movement of a 3 mm seed in *ex vivo* liver tissue while maximising the amount of force and duty cycle values. I performed movement of 3 mm seed in liver tissue using 500 mT/m gradient strength and continuous gradients.

The results of movements in liver samples A-C are shown in figures 6.6 A-C. The average movement efficiency in liver tissue (0.00076 ± 0.0001 mms^{-1}) was significantly lower than the corresponding parameter produced in brain tissue (*$P \leq 0.05$, Fig. 6.6 D). Such difference in movement efficiency is expected due to the difference in mechanical properties of these tissues (see section 2.3.5).

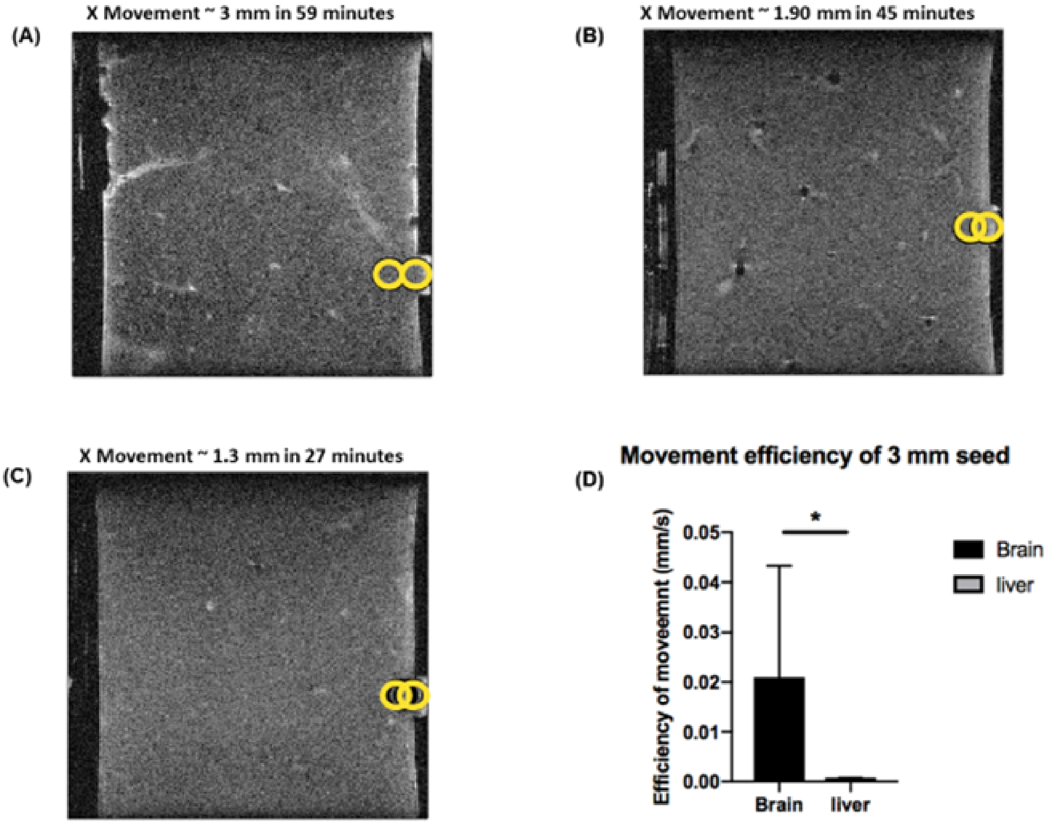

Figure 6.6- Movement of a 3 mm seed in *ex vivo* liver tissue using 500 mT/m. (A) Movement of the seed along X-direction overlaid on T_2-weighted image of ex-vivo liver tissue in sample A. Yellow circles in lower panel indicate the position of a 3 mm seed after each movement. (B) Movement of the seed in sample B. (C) Movement of the seed in sample C. (D) Efficiency of movement is significantly lower in liver tissue when compared with the brain tissue (*$P \leq 0.05$).

6.4 Discussion

Past studies in magnetic resonance targeting have utilised imaging gradient coils (IGC) or dedicated magnetic targeting systems (MTC) to guide magnetically labelled cells[31,155], ferromagnetic objects[206,207] or microparticles[130]. However, conventional imaging systems exhibit low duty cycles at high gradient amplitudes while magnetic targeting coils need an extra set of gradients to perform imaging. In this study we report production of an imaging gradient coil insert capable of producing 500 mT/m gradient strength at 100% duty cycle. This chapter reports experiments on movement of millimetre-sized magnetic seeds with the aim of improving the efficiency and control of movement in tissue while using gradient strengths which are closer to clinical settings. There were four major findings in this study.

- Movement is linearly dependent both on gradient strength and duty cycle (consistent with equations 2.23-2.25).
- Movement increases with duty cycle on-time.
- A 3 mm chrome steel sphere can be moved in *ex vivo* brain tissue using continuous gradients of 300 mT/m strength.
- Movement in liver tissue is significantly slower than movement in brain.

6.4.1 Optimisation of magnetic targeting parameters

The effect of duty cycle on movement of magnetic beads has never been studied in the past. The results of this study indicated that efficiency of movement increases with duty cycle and duty cycle on-time in viscous media. Moreover, continuous gradients (100% duty cycle) produced more movement in viscoelastic media (margarine) compared with pulsed gradients. This data confirm the efficacy of our novel magnetic targeting and imaging system in improving the movement of magnetic objects using an MRI system. As such, we decided to utilise 100% duty cycle gradients with maximised duty cycle on-time in future experiments.

In addition to the duty cycle, the magnetic force is also dependent on the saturation magnetisation of the seed (equations 2.23-2.25), which is in turn contingent on the seed material. When comparing movement of two different magnetic materials, more movement was observed with chrome steel seeds than neodymium (N42) beads; which was consistent with previous studies reporting that magnetic saturation of N42 magnets was 77% of that of steel beads in a 3T MRI[161]. As such, we decided to take the 3 mm chrome steel seed forward for movement in brain tissue investigations.

6.4.2 Movement in tissue using optimised parameters

Results from chapter 5 of this thesis indicated the possibility of movement of a 2 mm seed in brain tissue using 500 mT/m strength and 22% duty cycle. In this chapter I demonstrated that movement of a 3 mm magnetic thermoseed is possible in brain tissue with gradient amplitudes as low as 300 mT/m when 100% duty cycle were used. Recently a clinical imaging head gradient coil, known as the 'connectome coil', was developed to produce a gradient amplitude of 300 mT/m at 15% duty cycle[154]. However, our attempts to move the 3 mm seed in brain tissue were not successful when 300-400 mT/m gradient amplitudes were applied at 15% duty cycle (data not shown), indicating the significance of duty cycle. These data highlight the importance of developing clinical high-gradient IGCs or dedicated MTC systems that can produce high magnitude and prolonged gradients at 100% duty cycle without reaching the operational temperature limits[157].

It must be noted that brain tissue movements carried out in this study were along the positive Y-direction within the bore of the MRI scanner which was in line with the direction of gravity. However, the gravitational force produced by the weight of a 3 mm seed (1 mN) is about 6-fold lower than the magnetic force applied on this seed at 400 mT/m (6.2 mN) and therefore only a small contribution is made by the weight of the seed; although such contribution cannot be neglected.

Tissue penetration of magnetic devices using an MRI scanner has previously been investigated using methods such as Gauss gun[161] or magnetic hammer systems[169]. However, the systems used in these studies were notably larger (40 mm length and 7.5 mm diameter) than the 3 mm magnetic seed used in this study. In addition, these methods only allow one dimensional movement of a large and complicated device; and there was no demonstration on the control over movement in these studies. In contrast, our strategy provides 3 dimensional and controlled navigation of a single ferromagnetic seed using an MRI system. In our study, a great majority of seed movements within tissue were in line with the applied gradients and displacements were reasonably controlled. The average movement efficiency was measured to be 0.021 ± 0.022 mm/s in brain tissue, which was only about half the speed of tissue penetration reported by the magnetic hammer actuation (0.04 mm/s) system. This is to be excepted due to the larger magnetic object and the sharp blades placed on the tip of the magnetic hammer device to allow easier tissue penetration[169].

Experiments conducted in section 6.3.6 further illustrated that movement of a 3 mm seed is possible in *ex vivo* sheep liver tissue when 500 mT/m amplitude is used continuously. Although the efficiency of movement was drastically small, almost all targeting sequences resulted in movements and displacements were consistent in all three samples. Such consistency of movement (standard deviation of 0.0001) contrasts with the brain experiment movements (standard deviation of 0.0224) where a considerable degree of variability was observed in movement between different samples and different tissue structures within the same sample. In 3 of the brain samples tested in this study (samples B,C,E), the displacement of the seed slowed down considerably when reaching the white matter tissue and increasing the total on-time did not lead to improvements. However, in the other two samples (samples A, D) consistent movements were observed through all areas of the brain tissue, which further highlights the variability in mechanical properties of different structures and parts of the tissue.

The ability of producing more efficient movement in grey matter (0.057 mm/s) compared with white matter (0.007 mm/s) tissue was consistent with previous investigations where white matter tissue was measured to be on average 39% stiffer than grey matter[224]. Nonetheless, the white and grey matter at different parts of the brain are likely to have different properties. As such, future studies will need to investigate movement in white and grey matter at different parts of the brain to provide regional information about control and efficiency of movement. These information will be valuable for choosing the best path to navigate the seed through.

Future efforts should go into further optimisation of the magnetic seed in terms of size, material and shape in order to penetrate dense regions of the brain tissue such as those observed in this study. For example, adding cutting faces would allow for the seed to cut through tissue while the material and size optimisation can maximise the magnitude of the applied magnetic force. However, considering the effect of simply increasing seed size and gradient strength, the benefits of changing shape are less obvious and beyond the scope of this study.

6.4.3 Delivering therapy

In order to deliver therapy using the MRI scanner, the magnetic seed needs to be safely inserted and removed from the body. When the seed is inside the MRI scanner it experiences no translational force (in the absence of gradient magnetic field) as there exists a homogenous main magnetic field within the imaging volume. However, when moving from outside the scanner into the imagining volume, a large magnetic translational force is applied on the magnetic particle, which poses a challenge on safe insertion and removal of the seed. To provide a potential solution to this problem, we have demonstrated safe insertion and removal of a 3 mm chrome steel seed using a rampable MRI system (MR Solutiuons 7T scanner) when the main magnetic field was ramped down (data not shown). Likewise, other potential solutions such as using a mechanical device to hold the seed in place on entry into the MR system are currently undergoing investigation in parallel studies.

It has been demonstrated in separate studies at UCL that chrome steel seeds can be heated using an externally applied alternating magnetic field to cause well defined, localised regions of cell death (under publication). An MRI compatible heating coil was developed capable of generating an AMF of strength and frequency for specific heating of the seed alone. The extent of cell death around the seed was then controlled by changing the duration and strength of the AMF applied both *in vitro* and *in vivo* experiments. Clear cell death was observed after only 1 minute of heating, delivering fast ablation to open up the possibility of multiple ablation sites during one surgical procedure. The combination of results of the magnetic navigation (chapters 5 and 6 of this thesis) and ablation studies can lead to development of a minimally invasive image guided ablation system.

To deliver treatment to specific locations within the body, current methods implant millimetre-sized rods or arrays of smaller seeds into the target region to produce a homogenous therapeutic effect throughout the treatment region[225]. However, previous studies have reported issues associated with seed migration and chemical toxicity from seed degradation[226]. The ability to guide our seed into multiple positions, producing homogeneous ablation within the target region, and removing it safely during a single surgery overcomes the problems associated with the inaccuracies in positioning the seed and its migration. In addition, this method will allow ablation of multiple lesions with irregular shapes without the need for seed arrays reducing the invasiveness of the surgical operation. Future work will aim to utilise the real-time feedback control provided by the imaging system to produce an automated navigation/ablation method based on the predefined target points within the tissue.

6.5 Conclusion

In this study I have used a novel imaging gradient coil system to investigate movement of magnetic seeds using different duty cycles of applied field gradients. The results of the study have shown that movement efficiency is significantly improved when continuous gradients are applied compared with pulsed gradients. I have then used the advantage of increased duty cycle to produce movements of thermoseeds in tissue using gradient amplitudes that have been produced in clinical settings. These results further indicated that thermoseed movements were reasonably controlled in tissue; however, the dynamic range of the magnetic navigation mechanism needs to be increased to overcome the variability in mechanical properties of brain tissue. Combining the results of this study and the heating investigations from parallel ongoing studies demonstrates the essential components for transforming an MRI scanner into a theranostic tool: precise localisation, controlled movement through tissue, and accurate ablation using magnetic thermoseeds.

7. Conclusions and future directions

Magnetic targeting has the potential to become an impactful technology to improve treatment efficacy. In order to realise this potential major hurdles need to be overcome. This includes technical limitations of insufficient forces deep inside the body for external magnets, availability of clinically approved magnetic propulsion systems and particles, as well as the safety and efficacy of the treatment based procedure.

Chapter 3 and 4 focused on investigating the efficacy of external permanent magnets for magnetic targeting. Potential advantages of permanent magnets are the simplicity of use and cost-effectiveness, the lack of need for cooling and control electronics, strong magnetic fields and magnetic field gradients.

Experimental results from chapters 3 and 4 indicated that our novel magnetic designs can increase the depth and improve the spatial distribution of nanoparticle targeting in tumour tissue. Based on these observations, a clinical (U-shaped) magnet was then designed which has the potential to increase the targeting depth from millimetre to centimetre scales (< 7 cm) within human body. Such magnet design allows treatment of inoperable tumours (such as the head and breast tumours investigated in the human trial[11]) in a wider class of patients. However, to illustrate the clinical efficacy of such an approach, it will be necessary to perform validation phantom and *in vivo* investigations using this magnet.

The experimental results indicate that the major limitation is the weak magnetic force acting on individual nanoparticles at longer distances (> 7 cm) than the ones investigated in this study. However, while it is understood that the carrier formulation needs to be optimised for specific applications, the external magnetic system also needs to be tailored to the requirements of a given application accounting for the depth and physiological flow regime at the target. As indicated in chapter 4, one potential application of the U-shaped magnet is targeting deeply located breast tumours as this organ can fit inside the active space of the magnet. Magnetic drug targeting using 100 nm particles was previously shown to be safe and effective for targeting shallow breast tumours in the human trial[11]. As such, future experiments should aim to investigate and optimise the *in vivo* targeting efficiency of nanoparticles using this magnet specifically for deeply located primary or metastatic breast tumours.

Potential future steps of magnetic delivery of nanoparticles using our proposed magnet designs are as follows: Investigation of targeting efficiency of the U-shaped magnet using a flow phantom experiment, optimisation of nanoparticle size and surface chemistry, assessment of extravasation and retention of particles in tumour tissue, producing the drug loaded carrier formulation, and finally, *in vivo* investigation on the efficiency of treatment using U-shaped magnet design.

The flow phantom experiments and mathematical modelling performed in chapters 3 and 4 indicated the ability of the U-shaped magnet to target nanoparticles at centimetre distance scales inside the magnetically active space of the magnet. Future flow phantom experiments should aim to investigate the targeting efficiency of different nanoparticle sizes (100 - 300 nm) under simulated physiological flow regime of breast tumour microvasculature[227]. Such experimental approach will validate the efficacy of our proposed magnet and optimise the type and size of the nano-carrier used for magnetic tumour targeting using *in vitro* experiments.

Another strategy for increasing the targeting efficiency is to increase passive delivery of nanoparticles to the tumour vasculature. One way to achieve this is to optimise the surface chemistry of nanoparticles in order to reduce their uptake by the RES system (see section 1.1.1) and increase their blood circulation. Previous studies have demonstrated that cross-linked starch-coated particles[12] are a promising platform for enhanced magnetic tumour targeting as they increase the circulation time of the particles and consequently the tumour exposure of the drug.

Although the accumulation of nanoparticles could successfully be detected non-invasively by MRI, the experiments conducted in this study did not confirm extravasation of the captured nanoparticles from the blood vessels into the extravascular space. Additionally, this study did not include assessment of the retention period of nanoparticles within the tumours at various time points post targeting. Delivery of colloidal nanoparticles to the extravascular space and their retention has traditionally been attributed to the EPR effect (see section 1.1.1). However, experimental validation of the extent and duration of nanoparticle accumulation within the extravascular space will be of considerable importance for specific nanoparticle and tumour types. Another limitation is the inability to control the precise size of the nanoparticles *in vivo* due to the tendency of these particles to form larger aggregate sizes (see section 2.2.1). Although such aggregation can be advantageous as it increases the effective force on the particles, it could lead to vascular blockage and micro emboli in severe cases. Despite the fact that there is no direct evidence for this limitation, the risk of micro emboli formation should be assessed in a suitable animal model in the future.

Finally, appropriate methods need to be employed for conjugation of the therapeutic agent with the magnetic carrier. During recent years, the majority of preclinical investigations of magnetic drug targeting have used encapsulated formulations to investigate the efficacy of their carrier formulations[5,156,176]. As indicated in chapter 3, a larger net force can be applied on encapsulated carrier compared with unencapsulated particles used in this study. Therefore, using encapsulated carriers will increase the applied magnetic force and consequently the chances of a successful magnetic targeting within the target region. Future efforts should either set up collaborations with other groups who have successfully optimised and demonstrated the efficacy of their drug carrier formulation or develop novel drug carrier systems using Chemicell particles used in this study. The wide range of surface chemistry available with Chemicell particles will be beneficial if the latter option is chosen to be explored. In conclusion, *in vivo* magnetic targeting of breast tumours located within 7 cm depth inside the body needs to be explored using the optimised drug loaded carriers and the U-shaped magnetic design.

Chapters 5 and 6 focused on using the magnetic resonance imaging system to navigate millimetre-sized spherical particles (seeds) on a pre-determined path in tissue. Potential advantageous of such approach are: the spatial precision and controllability of the applied magnetic force, the ability to perform closed loop image guided propulsions due to the imaging capability of MRI, and the homogeneity of the magnetic force within the imaging volume.

Experiments carried out in chapters 5 and 6 demonstrated the ability of image guided movement of magnetic seeds in *ex vivo* tissue using MRI for the first time. The degree of control and precision of movement was illustrated in viscous media, however movement of the seed in biological tissue was observed to be more dependent on the structural properties of tissue. The results of the experiments carried out using a custom made gradient coil insert showed the improvement on controlled movement of the magnetic seed when continuous gradients are used as opposed to conventional pulsed gradients. Using the optimised duty cycle and seed size, I was able to demonstrate movement in *ex vivo* brain tissue using clinically reproducible magnetic gradient strengths. With relatively little modification to existing MRI gradient coils, it is anticipated that they could be transformed into a new class of theranostic device for image guided drug delivery or magnetic ablation surgeries. However, there are further steps which need to be taken before this strategy can be used in men.

Potential future work are: Hardware modifications to increase the gradient strength and duty cycle, safety of injection and removal of the seed, therapeutic effect of the magnetic seed, controlled navigation of the seed in different tissue structures.

The available gradient strength is one of the major variables determining the efficacy of treatment delivery using the image guided navigation strategy developed in this thesis. As indicated in chapter 2, the size of the gradient coil has a substantial influence on its ability to produce high amplitude gradients. Increasing the gradient strength on preclinical MRI systems is certainly feasible but it is questionable if such gradient strengths could be achieved for a clinical system. Additional consideration has to be given to the risk of peripheral nerve stimulation if high amplitude gradients are switched rapidly. Another limitation is the temperature management and power consumption constraints which may limit the ability to produce continuous gradients at high amplitude in a clinical setting. One possibility to avoid these problems is the use of dedicated magnetic targeting gradients which do not comply with the stringent criteria of MRI (see section 2.3.3) but are optimised for targeting and would hence not suffer from duty cycle limitations. This would be feasible but would create difficulties if imaging is used intermittently to guide seeds along.

One of the main limitations of our proposed MR guided navigation method is the insertion and removal of the magnetic seed to and from the body when the patient is outside the scanner. This is due to the strong gradients of the main magnetic field immediately outside the isocenter of the scanner. Our preliminary experiments in parallel studies have demonstrated the possibility of using a rampable preclinical MRI system which can be ramped down before insertion and removal of the sample into and from the MRI bore. However, the requirement for performing surgery using a rampable system limits this method to dedicated MRI facilities, which may reduce the ease-to-access and increase the surgery costs. Additionally, the feasibility of producing a rampable clinical MRI system has yet to be addressed. As such, a safe, feasible and cost efficient approach needs to be developed for seed insertion and removal in the future.

In separate studies, it has been demonstrated that magnetic seeds can be heated using an externally applied alternating magnetic field to cause well-controlled regions of cell death in cell phantom experiments and *in vivo* brain tissue ablation experiments. While an MRI compatible heating coil was developed capable of generating specific heating of the seed alone, this method is currently limited by the inability to image and move the seeds when the heating coil is positioned inside the scanner. Future efforts should go into adapting the heating coil to provide either an imaging window between the windings of the coil, or modify it so that RF can pass through without affecting image quality.

In addition to ablation capabilities, there is also potential to explore the efficacy of our proposed approach as a targeted drug delivery technique. In order to be able to deliver drugs, biocompatible formulations will need to be investigated for encapsulating the therapeutic moiety in or around the magnetic seed. Once the seed is inside the tumour, elevation of temperature or other control mechanisms can be used to release the drug into the tumour microenvironment. With the increasing interest in the field of biomaterials and tissue engineering, future efforts should focus on developing drug carrier systems using the magnetic seeds used in this study; utilising drug delivery systems such as hydrogels[228] appears to be a possible option. The advantage of this method over intravascular delivery is the ability to deliver drugs interstitially to tumour locations where there is lower blood supply and as a result lower delivery of drugs.

Although the 3 mm seed could be moved with reasonable control using continuous gradients of 300-400 mT/m strength, a considerable degree of variability was observed in different regions of brain tissue. If the brain tissues were completely homogeneous and isotropic, the penetration and drag forces that act on the seed would be evenly distributed throughout the brain and therefore a reliably predictable magnetic force strength would be required at all locations throughout the movement path. However, given the considerable variations encountered in the composition and density of the anatomical structures of the brain, correspondingly significant variations in penetration and drag force will be encountered, as seen in our data. Additionally, as indicated in section 2.3.5, compared with healthy brain tissue, brain tumours have a higher stiffness which further increases the resistive force applied on the seed. As such, future studies should aim to investigate the control and efficiency of movement in different regions of the brain, different tissues and tumours in separate studies. These information will give the surgeon the best indication of the length of time needed to navigate through a pre-planned path within the tissue.

The efficiency of movement observed in my experiments were several times lower than other magnetic tissue penetrating systems[2,169], which creates the need for a longer total surgery time. The solution to this problems is to insure that the seed navigation mechanism has adequate dynamic range to overcome the largest resistive force to be encountered, which can increase the control and speed of movement. This can be done either by increasing the steering magnetic force or by reducing the tissue resistive forces (e.g. introducing cutting faces or heating the tissue surrounding the seed).

In order to address the current limitations, future efforts should focus on increasing the dynamic range of magnetic propulsion force in a clinical scale both by producing high strength dedicated gradient coils and further optimising the seed size, material or shape. To address the gradient coil design, investigations are ongoing with tesla engineering company to design an optimised magnetic targeting gradient coil with highest possible gradient amplitude and duty cycle for human brain. Once the optimised gradient coil, heating coil and magnetic seeds are developed and implemented, future experiments will need to investigate the combination of seed movement and ablation in live animals using a clinical MRI scanner.

References

1. Price, P. M., Mahmoud, W. E., Al-Ghamdi, A. A. & Bronstein, L. M. Magnetic Drug Delivery: Where the Field Is Going. *Front. Chem.* **6,** (2018).
2. Grady, M. S. *et al.* Magnetic stereotaxis: a technique to deliver stereotactic hyperthermia. *Neurosurgery* **27,** 1010–1015; discussion 1015-1016 (1990).
3. Maeda, H., Wu, J., Sawa, T., Matsumura, Y. & Hori, K. Tumor vascular permeability and the EPR effect in macromolecular therapeutics: a review. *J. Controlled Release* **65,** 271–284 (2000).
4. Muhamad, N., Plengsuriyakarn, T. & Na-Bangchang, K. Application of active targeting nanoparticle delivery system for chemotherapeutic drugs and traditional/herbal medicines in cancer therapy: a systematic review. *Int. J. Nanomedicine* **Volume 13,** 3921–3935 (2018).
5. Al-Jamal, K. T. *et al.* Magnetic Drug Targeting: Preclinical in Vivo Studies, Mathematical Modeling, and Extrapolation to Humans. *Nano Lett.* **16,** 5652–5660 (2016).
6. Zimmermann, U. & Pilwat, G. [Organ specific application of drugs by means of cellular capsule systems (author’s transl)]. *Z. Naturforsch. [C]* **31,** 732–736 (1976).
7. Senyei, A. E., Reich, S. D., Gonczy, C. & Widder, K. J. In vivo kinetics of magnetically targeted low-dose doxorubicin. *J. Pharm. Sci.* **70,** 389–391 (1981).
8. Widder, K. J. *et al.* Selective targeting of magnetic albumin microspheres to the Yoshida sarcoma: ultrastructural evaluation of microsphere disposition. *Eur. J. Cancer Clin. Oncol.* **19,** 141–147 (1983).

9. Zhang, Z., He, P., Zhang, J., Li, Y. & Wang, Q. Recent advances in magnetic targeting based on high magnetic field and magnetic particles. *High Volt.* **2,** 220–232 (2017).

10. Danhier, F., Feron, O. & Préat, V. To exploit the tumor microenvironment: Passive and active tumor targeting of nanocarriers for anti-cancer drug delivery. *J. Controlled Release* **148,** 135–146 (2010).

11. Lübbe AS1, Bergemann C, Riess H, Schriever F, Reichardt P, Possinger K, Matthias M, Dörken B, Herrmann F, Gürtler R, Hohenberger P, Haas N, Sohr R, Sander B, Lemke AJ, Ohlendorf D, Huhnt W, Huhn D. Clinical experiences with magnetic drug targeting: a phase I study with 4’-epidoxorubicin in 14 patients with advanced solid tumors. *Cancer Res* **56,** 4686–93 (1996).

12. Cole, A. J. *et al.* Polyethylene glycol modified, cross-linked starch-coated iron oxide nanoparticles for enhanced magnetic tumor targeting. *Biomaterials* **32,** 2183–2193 (2011).

13. Kohler, N., Sun, C., Wang, J. & Zhang, M. Methotrexate-Modified Superparamagnetic Nanoparticles and Their Intracellular Uptake into Human Cancer Cells. *Langmuir* **21,** 8858–8864 (2005).

14. N’Guyen, T. T. T. *et al.* Functional Iron Oxide Magnetic Nanoparticles with Hyperthermia-Induced Drug Release Ability by Using a Combination of Orthogonal Click Reactions. *Angew. Chem. Int. Ed.* **52,** 14152–14156 (2013).

15. Ponta, A. & Bae, Y. Tumor-preferential sustained drug release enhances antitumor activity of block copolymer micelles. *J. Drug Target.* **22,** 619–628 (2014).

16. Hwu, J. R. *et al.* Targeted Paclitaxel by Conjugation to Iron Oxide and Gold Nanoparticles. *J. Am. Chem. Soc.* **131,** 66–68 (2009).

17. Lee, J.-H. *et al.* All-in-One Target-Cell-Specific Magnetic Nanoparticles for Simultaneous Molecular Imaging and siRNA Delivery. *Angew. Chem. Int. Ed.* **48,** 4174–4179 (2009).

18. Tietze, R. *et al.* Efficient drug-delivery using magnetic nanoparticles — biodistribution and therapeutic effects in tumour bearing rabbits. *Nanomedicine Nanotechnol. Biol. Med.* **9,** 961–971 (2013).

19. Yu, M. K. *et al.* Drug-Loaded Superparamagnetic Iron Oxide Nanoparticles for Combined Cancer Imaging and Therapy In Vivo. *Angew. Chem. Int. Ed.* **47,** 5362–5365 (2008).

20. Gautier, J., Allard-Vannier, E., Burlaud-Gaillard, J., Domenech, J. & Chourpa, I. Efficacy and Hemotoxicity of Stealth Doxorubicin-Loaded Magnetic Nanovectors on Breast Cancer Xenografts. *J. Biomed. Nanotechnol.* **11,** 177–189 (2015).

21. Lee, J. *et al.* A multifunctional mesoporous nanocontainer with an iron oxide core and a cyclodextrin gatekeeper for an efficient theranostic platform. *J. Mater. Chem.* **22,** 14061 (2012).

22. David, A. E., Cole, A. J., Chertok, B., Park, Y. S. & Yang, V. C. A combined theoretical and in vitro modeling approach for predicting the magnetic capture and retention of magnetic nanoparticles in vivo. *J. Controlled Release* **152,** 67–75 (2011).

23. Noguchi, Y. *et al.* Early Phase Tumor Accumulation of Macromolecules: A Great Difference in Clearance Rate between Tumor and Normal Tissues. *Jpn. J. Cancer Res.* **89,** 307–314 (1998).

24. Widder, K. J., Morris, R. M., Poore, G. A., Howard, D. P. & Senyei, A. E. Selective targeting of magnetic albumin microspheres containing low-dose

doxorubicin: total remission in Yoshida sarcoma-bearing rats. *Eur. J. Cancer Clin. Oncol.* **19,** 135–139 (1983).

25. Alexiou, C. *et al.* Locoregional cancer treatment with magnetic drug targeting. *Cancer Res.* **60,** 6641–6648 (2000).
26. Lübbe, A. S., Bergemann, C., Brock, J. & McClure, D. G. Physiological aspects in magnetic drug-targeting. *J. Magn. Magn. Mater.* **194,** 149–155 (1999).
27. Pulfer, S. K., Ciccotto, S. L. & Gallo, J. M. Distribution of small magnetic particles in brain tumor-bearing rats. *J. Neurooncol.* **41,** 99–105 (1999).
28. Shao, D. *et al.* Janus "nano-bullets" for magnetic targeting liver cancer chemotherapy. *Biomaterials* **100,** 118–133 (2016).
29. Goodwin, S., Peterson, C., Hoh, C. & Bittner, C. Targeting and retention of magnetic targeted carriers (MTCs) enhancing intra-arterial chemotherapy. *J. Magn. Magn. Mater.* **194,** 132–139 (1999).
30. Goodwin, S. C., Bittner, C. A., Peterson, C. L. & Wong, G. Single-Dose Toxicity Study of Hepatic Intra-arterial Infusion of Doxorubicin Coupled to a Novel Magnetically Targeted Drug Carrier. *Toxicol. Sci.* **60,** 177–183 (2001).
31. Muthana, M. *et al.* Directing cell therapy to anatomic target sites in vivo with magnetic resonance targeting. *Nat. Commun.* **6,** (2015).
32. Pankhurst, Q. A., Connolly, J., Jones, S. K. & Dobson, J. Applications of magnetic nanoparticles in biomedicine. *J. Phys. Appl. Phys.* **36,** R167–R181 (2003).
33. De Luca, M. *et al.* Advances in stem cell research and therapeutic development. *Nat. Cell Biol.* (2019). doi:10.1038/s41556-019-0344-z
34. P.Stephen Patrick QAP Christopher Payne, Tammy L Kalber, Mark F Lythgoe. Magnet-targeted delivery and imaging. in *Design and Applications of nanoparticles in Biomedical Imaging.* 123–49 (2016).

35. Riegler, J. *et al.* Superparamagnetic iron oxide nanoparticle targeting of MSCs in vascular injury. *Biomaterials* **34,** 1987–1994 (2013).

36. Kyrtatos, P. G. *et al.* Magnetic Tagging Increases Delivery of Circulating Progenitors in Vascular Injury. *JACC Cardiovasc. Interv.* **2,** 794–802 (2009).

37. Weissleder, R. *et al.* Superparamagnetic iron oxide: pharmacokinetics and toxicity. *Am. J. Roentgenol.* **152,** 167–173 (1989).

38. Jain, T. K., Reddy, M. K., Morales, M. A., Leslie-Pelecky, D. L. & Labhasetwar, V. Biodistribution, Clearance, and Biocompatibility of Iron Oxide Magnetic Nanoparticles in Rats. *Mol. Pharm.* **5,** 316–327 (2008).

39. Pouliquen, D., Le Jeune, J. J., Perdrisot, R., Ermias, A. & Jallet, P. Iron oxide nanoparticles for use as an MRI contrast agent: Pharmacokinetics and metabolism. *Magn. Reson. Imaging* **9,** 275–283 (1991).

40. Panizzo, R. *et al.* In vivo magnetic resonance imaging of endogenous neuroblasts labelled with a ferumoxide–polycation complex. *NeuroImage* **44,** 1239–1246 (2009).

41. Bulte, J. W. M. & Kraitchman, D. L. Iron oxide MR contrast agents for molecular and cellular imaging. *NMR Biomed.* **17,** 484–499 (2004).

42. de Vries, I. J. M. *et al.* Magnetic resonance tracking of dendritic cells in melanoma patients for monitoring of cellular therapy. *Nat. Biotechnol.* **23,** 1407–1413 (2005).

43. Karussis, D. *et al.* Safety and Immunological Effects of Mesenchymal Stem Cell Transplantation in Patients With Multiple Sclerosis and Amyotrophic Lateral Sclerosis. *Arch. Neurol.* **67,** (2010).

44. Arbab, A. S. *et al.* Labeling of cells with ferumoxides-protamine sulfate complexes does not inhibit function or differentiation capacity of hematopoietic or mesenchymal stem cells. *NMR Biomed.* **18,** 553–559 (2005).

45. Thorek, D. L. J. & Tsourkas, A. Size, charge and concentration dependent uptake of iron oxide particles by non-phagocytic cells. *Biomaterials* **29,** 3583–3590 (2008).

46. Rejman, J., Oberle, V., Zuhorn, I. S. & Hoekstra, D. Size-dependent internalization of particles via the pathways of clathrin- and caveolae-mediated endocytosis. *Biochem. J.* **377,** 159–169 (2004).

47. Frank, J. A. *et al.* Clinically Applicable Labeling of Mammalian and Stem Cells by Combining Superparamagnetic Iron Oxides and Transfection Agents. *Radiology* **228,** 480–487 (2003).

48. Zhu, J., Zhou, L. & XingWu, F. Tracking Neural Stem Cells in Patients with Brain Trauma. *N. Engl. J. Med.* **355,** 2376–2378 (2006).

49. Callera, F. & de Melo, C. M. T. P. Magnetic Resonance Tracking of Magnetically Labeled Autologous Bone Marrow CD34 $^+$ Cells Transplanted into the Spinal Cord via Lumbar Puncture Technique in Patients with Chronic Spinal Cord Injury: CD34 $^+$ Cells' Migration into the Injured Site. *Stem Cells Dev.* **16,** 461–466 (2007).

50. Theruvath, A. J. *et al.* Tracking Cell Transplants in Femoral Osteonecrosis with Magnetic Resonance Imaging: A Proof-of-Concept Study in Patients. *Clin. Cancer Res.* **24,** 6223–6229 (2018).

51. Barbosa da Fonseca, L. M. *et al.* Early Tissue Distribution of Bone Marrow Mononuclear Cells After Intra-Arterial Delivery in a Patient With Chronic Stroke. *Circulation* **120,** 539–541 (2009).

52. Hofmann, M. *et al.* Monitoring of Bone Marrow Cell Homing Into the Infarcted Human Myocardium. *Circulation* **111,** 2198–2202 (2005).

53. Freed, C. R. *et al.* Transplantation of Embryonic Dopamine Neurons for Severe Parkinson’s Disease. *N. Engl. J. Med.* **344,** 710–719 (2001).

54. Patrick, P. S. *et al.* Surface radio-mineralisation mediates chelate-free radiolabelling of iron oxide nanoparticles. *Chem. Sci.* **10,** 2592–2597 (2019).

55. Cao, F. *et al.* In Vivo Visualization of Embryonic Stem Cell Survival, Proliferation, and Migration After Cardiac Delivery. *Circulation* **113,** 1005–1014 (2006).

56. Contag, C. H. & Bachmann, M. H. Advances in In Vivo Bioluminescence Imaging of Gene Expression. *Annu. Rev. Biomed. Eng.* **4,** 235–260 (2002).

57. Dubey, P. Visualization of Immune Cell Reconstitution by Bioluminescent Imaging. in *Reporter Gene Imaging* (ed. Dubey, P.) **1790,** 127–136 (Springer New York, 2018).

58. Gorantla, S. *et al.* Quantitative magnetic resonance and SPECT imaging for macrophage tissue migration and nanoformulated drug delivery. *J. Leukoc. Biol.* **80,** 1165–1174 (2006).

59. Parashurama, N. *et al.* Multimodality Molecular Imaging of Cardiac Cell Transplantation: Part II. In Vivo Imaging of Bone Marrow Stromal Cells in Swine with PET/CT and MR Imaging. *Radiology* **280,** 826–836 (2016).

60. Riegler, J. *et al.* Magnetic cell delivery for peripheral arterial disease: A theoretical framework: Magnetic cell delivery to lower leg arteries. *Med. Phys.* **38,** 3932–3943 (2011).

61. Connell, J. J., Patrick, P. S., Yu, Y., Lythgoe, M. F. & Kalber, T. L. Advanced cell therapies: targeting, tracking and actuation of cells with magnetic particles. *Regen. Med.* **10,** 757–772 (2015).

62. Arbab, A. S. *et al. In Vivo* Trafficking and Targeted Delivery of Magnetically Labeled Stem Cells. *Hum. Gene Ther.* **15,** 351–360 (2004).
63. Riegler, J., Allain, B., Cook, R. J., Lythgoe, M. F. & Pankhurst, Q. A. Magnetically assisted delivery of cells using a magnetic resonance imaging system. *J. Phys. Appl. Phys.* **44,** 055001 (2011).
64. Busquets, M. A., Estelrich, J. & Sánchez-Martín, M. J. Nanoparticles in magnetic resonance imaging: from simple to dual contrast agents. *Int. J. Nanomedicine* 1727 (2015). doi:10.2147/IJN.S76501
65. G.W. Reimers, S.E. Khalafalla. *Preparing magnetic fluids by a peptizing method.* (1972).
66. Krishnan, K. M. Biomedical Nanomagnetics: A Spin Through Possibilities in Imaging, Diagnostics, and Therapy. *IEEE Trans. Magn.* **46,** 2523–2558 (2010).
67. Babincová, M., Babinec, P. & Bergemann, C. High-Gradient Magnetic Capture of Ferrofluids: Implications for Drug Targeting and Tumor Embolization. *Z. Für Naturforschung C* **56,** 909–911 (2001).
68. Wang, Y.-X. J., Hussain, S. M. & Krestin, G. P. Superparamagnetic iron oxide contrast agents: physicochemical characteristics and applications in MR imaging. *Eur. Radiol.* **11,** 2319–2331 (2001).
69. Sun, S. & Zeng, H. Size-Controlled Synthesis of Magnetite Nanoparticles. *J. Am. Chem. Soc.* **124,** 8204–8205 (2002).
70. Sun, S. *et al.* Monodisperse MFe_2O_4 (M = Fe, Co, Mn) Nanoparticles. *J. Am. Chem. Soc.* **126,** 273–279 (2004).
71. *Nanophase Materials*. (Springer Netherlands, 1994). doi:10.1007/978-94-011-1076-1

72. Sjøgren, C. E., Briley-Sæbø, K., Hanson, M. & Johansson, C. Magnetic characterization of iron oxides for magnetic resonance imaging. *Magn. Reson. Med.* **31,** 268–272 (1994).

73. Ho, D., Sun, X. & Sun, S. Monodisperse Magnetic Nanoparticles for Theranostic Applications. *Acc. Chem. Res.* **44,** 875–882 (2011).

74. Kudr, J. *et al.* Magnetic Nanoparticles: From Design and Synthesis to Real World Applications. *Nanomaterials* **7,** 243 (2017).

75. Tepper, T. *et al.* Magneto-optical properties of iron oxide films. *J. Appl. Phys.* **93,** 6948–6950 (2003).

76. Veiseh, O., Gunn, J. W. & Zhang, M. Design and fabrication of magnetic nanoparticles for targeted drug delivery and imaging. *Adv. Drug Deliv. Rev.* **62,** 284–304 (2010).

77. Wu, M. & Huang, S. Magnetic nanoparticles in cancer diagnosis, drug delivery and treatment (Review). *Mol. Clin. Oncol.* (2017). doi:10.3892/mco.2017.1399

78. Thomas, R., Park, I.-K. & Jeong, Y. Magnetic Iron Oxide Nanoparticles for Multimodal Imaging and Therapy of Cancer. *Int. J. Mol. Sci.* **14,** 15910–15930 (2013).

79. Srivastava, A. K. *et al.* Advances in using MRI probes and sensors for in vivo cell tracking as applied to regenerative medicine. *Dis. Model. Mech.* **8,** 323–336 (2015).

80. Cha, E.-J. *et al.* Development of MRI/NIRF ‘activatable’ multimodal imaging probe based on iron oxide nanoparticles. *J. Controlled Release* **155,** 152–158 (2011).

81. Kim, D. *et al.* Amphiphilic polymer-coated hybrid nanoparticles as CT/MRI dual contrast agents. *Nanotechnology* **22,** 155101 (2011).

82. Yang, X. *et al.* cRGD-functionalized, DOX-conjugated, and 64Cu-labeled superparamagnetic iron oxide nanoparticles for targeted anticancer drug delivery and PET/MR imaging. *Biomaterials* **32,** 4151–4160 (2011).

83. Misri, R., Meier, D., Yung, A. C., Kozlowski, P. & Häfeli, U. O. Development and evaluation of a dual-modality (MRI/SPECT) molecular imaging bioprobe. *Nanomedicine Nanotechnol. Biol. Med.* **8,** 1007–1016 (2012).

84. Zaw Thin, M. *et al.* Multi-modal Cell Labelling for Quantification and Optimization of Stem Cell Delivery to Orthotopic Breast Tumors. doi:10.26434/chemrxiv.7992239.v1

85. Kalber, T. *et al.* Hyperthermia treatment of tumors by mesenchymal stem cell-delivered superparamagnetic iron oxide nanoparticles. *Int. J. Nanomedicine* 1973 (2016). doi:10.2147/IJN.S94255

86. Chang, D. *et al.* Biologically Targeted Magnetic Hyperthermia: Potential and Limitations. *Front. Pharmacol.* **9,** (2018).

87. Xue, W. *et al.* AMF responsive DOX-loaded magnetic microspheres: transmembrane drug release mechanism and multimodality postsurgical treatment of breast cancer. *J. Mater. Chem. B* **6,** 2289–2303 (2018).

88. Rosensweig, R. E. Heating magnetic fluid with alternating magnetic field. *J. Magn. Magn. Mater.* **252,** 370–374 (2002).

89. Gilchrist, R. K. *et al.* Selective inductive heating of lymph nodes. *Ann. Surg.* **146,** 596–606 (1957).

90. Jordan, A., Scholz, R., Wust, P., Fähling, H. & Roland Felix. Magnetic fluid hyperthermia (MFH): Cancer treatment with AC magnetic field induced excitation of biocompatible superparamagnetic nanoparticles. *J. Magn. Magn. Mater.* **201,** 413–419 (1999).

91. Jordan, A. *et al.* Presentation of a new magnetic field therapy system for the treatment of human solid tumors with magnetic fluid hyperthermia. *J. Magn. Magn. Mater.* **225,** 118–126 (2001).

92. Maier-Hauff, K. *et al.* Efficacy and safety of intratumoral thermotherapy using magnetic iron-oxide nanoparticles combined with external beam radiotherapy on patients with recurrent glioblastoma multiforme. *J. Neurooncol.* **103,** 317–324 (2011).

93. Johannsen, M., Thiesen, B., Wust, P. & Jordan, A. Magnetic nanoparticle hyperthermia for prostate cancer. *Int. J. Hyperthermia* **26,** 790–795 (2010).

94. Motoyama, J. *et al.* Hyperthermic treatment of DMBA-induced rat mammary cancer using magnetic nanoparticles. *Biomagn. Res. Technol.* **6,** 2 (2008).

95. Balivada, S. *et al.* A/C magnetic hyperthermia of melanoma mediated by iron(0)/iron oxide core/shell magnetic nanoparticles: a mouse study. *BMC Cancer* **10,** (2010).

96. Béalle, G. *et al.* Ultra Magnetic Liposomes for MR Imaging, Targeting, and Hyperthermia. *Langmuir* **28,** 11834–11842 (2012).

97. Brezovich, I. A. *et al.* Hyperthermia of pet animal tumours with self-regulating ferromagnetic thermoseeds. *Int. J. Hyperth. Off. J. Eur. Soc. Hyperthermic Oncol. North Am. Hyperth. Group* **6,** 117–130 (1990).

98. Burton, C., Hill, M. & Walker, E. The RF thermoseed--a thermally self-regulating implant for the production of brain lesions. *IEEE Trans. Biomed. Eng.* **18,** 104–109 (1971).

99. Kida, Y., Mori, Y., Hattori, T. & Kobayashi, T. [Interstitial hyperthermia of malignant gliomas with implant heating system]. *No Shinkei Geka.* **18,** 1007–1014 (1990).

100. Kobayashi, T. *et al.* Interstitial hyperthermia of malignant brain tumors by implant heating system: Clinical experience. *J. Neurooncol.* **10,** 153–163 (1991).

101. Deger, S. *et al.* Thermoradiotherapy Using Interstitial Self-Regulating Thermoseeds: An Intermediate Analysis of a Phase II Trial. *Eur. Urol.* **45,** 574–580 (2004).

102. Stea, B. *et al.* Treatment of malignant gliomas with interstitial irradiation and hyperthermia. *Int. J. Radiat. Oncol.* **24,** 657–667 (1992).

103. Deger, S. *et al.* Interstitial Hyperthermia using Self-Regulating Thermoseeds Combined with Conformal Radiation Therapy. *Eur. Urol.* **42,** 147–153 (2002).

104. Peter R. WerpWalter M. BlumeFrancis M. Creighton, IVRogers C. Ritter. Methods and apparatus for magnetically controlling motion direction of a mechanically pushed cathete.

105. Myers, H. P. *Introductory solid state physics*. (Taylor & Francis, 1997).

106. Hofmann, A. *et al.* Combined targeting of lentiviral vectors and positioning of transduced cells by magnetic nanoparticles. *Proc. Natl. Acad. Sci.* **106,** 44–49 (2009).

107. Fortin-Ripoche, J.-P. *et al.* Magnetic Targeting of Magnetoliposomes to Solid Tumors with MR Imaging Monitoring in Mice: Feasibility. *Radiology* **239,** 415–424 (2006).

108. Wilson, M. W. *et al.* Hepatocellular Carcinoma: Regional Therapy with a Magnetic Targeted Carrier Bound to Doxorubicin in a Dual MR Imaging/ Conventional Angiography Suite—Initial Experience with Four Patients. *Radiology* **230,** 287–293 (2004).

109. Nacev, A. *et al.* A dynamic magnetic shift method to increase nanoparticle concentration in cancer metastases: a feasibility study using simulations on autopsy specimens. *Int. J. Nanomedicine* 2907 (2011). doi:10.2147/IJN.S23724

110. Halbach, K. Strong Rare Earth Cobalt Quadrupoles. *IEEE Trans. Nucl. Sci.* **26,** 3882–3884 (1979).

111. Liu, Y.-L., Chen, D., Shang, P. & Yin, D.-C. A review of magnet systems for targeted drug delivery. *J. Controlled Release* **302,** 90–104 (2019).

112. Shapiro, B. *et al.* A Two-Magnet System to Push Therapeutic Nanoparticles. in 77–88 (2010). doi:10.1063/1.3530064

113. Sarwar, A., Lee, R., Depireux, D. A. & Shapiro, B. Magnetic Injection of Nanoparticles Into Rat Inner Ears at a Human Head Working Distance. *IEEE Trans. Magn.* **49,** 440–452 (2013).

114. Häfeli, U. O., Gilmour, K., Zhou, A., Lee, S. & Hayden, M. E. Modeling of magnetic bandages for drug targeting: Button vs. Halbach arrays. *J. Magn. Magn. Mater.* **311,** 323–329 (2007).

115. Sarwar, A., Nemirovski, A. & Shapiro, B. Optimal Halbach permanent magnet designs for maximally pulling and pushing nanoparticles. *J. Magn. Magn. Mater.* **324,** 742–754 (2012).

116. Babincova, M. & Babinec, P. Magnetic drug delivery and targeting: principles and applications. *Biomed. Pap. Med. Fac. Univ. Palacky Olomouc Czechoslov.* **153,** 243–250 (2009).

117. Al Faraj, A., Shaik, A. S., Shaik, A. P. & Al Sayed, B. Enhanced magnetic delivery of superparamagnetic iron oxide nanoparticles to the lung monitored using noninvasive MR. *J. Nanoparticle Res.* **16,** (2014).

118. Barnsley, L. C., Carugo, D. & Stride, E. Optimized shapes of magnetic arrays for drug targeting applications. *J. Phys. Appl. Phys.* **49,** 225501 (2016).

119. Yellen, B. B. *et al.* Targeted drug delivery to magnetic implants for therapeutic applications. *J. Magn. Magn. Mater.* **293,** 647–654 (2005).

120. Polyak, B. *et al.* High field gradient targeting of magnetic nanoparticle-loaded endothelial cells to the surfaces of steel stents. *Proc. Natl. Acad. Sci.* **105,** 698–703 (2008).

121. Avilés, M. O., Ebner, A. D. & Ritter, J. A. Implant assisted-magnetic drug targeting: Comparison of in vitro experiments with theory. *J. Magn. Magn. Mater.* **320,** 2704–2713 (2008).

122. Hajiaghajani, A., Hashemi, S. & Abdolali, A. Adaptable setups for magnetic drug targeting in human muscular arteries: Design and implementation. *J. Magn. Magn. Mater.* **438,** 173–180 (2017).

123. Chertok, B. *et al.* Iron oxide nanoparticles as a drug delivery vehicle for MRI monitored magnetic targeting of brain tumors. *Biomaterials* **29,** 487–496 (2008).

124. Dames, P. *et al.* Targeted delivery of magnetic aerosol droplets to the lung. *Nat. Nanotechnol.* **2,** 495–499 (2007).

125. Voronin, D. V. *et al.* In Vitro and in Vivo Visualization and Trapping of Fluorescent Magnetic Microcapsules in a Bloodstream. *ACS Appl. Mater. Interfaces* **9,** 6885–6893 (2017).

126. Takeda, S., Mishima, F., Fujimoto, S., Izumi, Y. & Nishijima, S. Development of magnetically targeted drug delivery system using superconducting magnet. *J. Magn. Magn. Mater.* **311,** 367–371 (2007).

127. Mishima, F., Takeda, S., Izumi, Y. & Nishijima, S. Development of Magnetic Field Control for Magnetically Targeted Drug Delivery System Using a Superconducting Magnet. *IEEE Trans. Appl. Supercond.* **17,** 2303–2306 (2007).

128. Meeker, D. C., Maslen, E. H., Ritter, R. C. & Creighton, F. M. Optimal realization of arbitrary forces in a magnetic stereotaxis system. *IEEE Trans. Magn.* **32,** 320–328 (1996).

129. Grady, M. S. *et al.* Experimental study of the magnetic stereotaxis system for catheter manipulation within the brain. *J. Neurosurg.* **93,** 282–288 (2000).

130. Pouponneau, P., Leroux, J.-C. & Martel, S. Magnetic nanoparticles encapsulated into biodegradable microparticles steered with an upgraded magnetic resonance imaging system for tumor chemoembolization. *Biomaterials* **30,** 6327–6332 (2009).

131. Olamaei, N., Cheriet, F., Beaudoin, G. & Martel, S. MRI visualization of a single 15 um navigable imaging agent and future microrobot. in 4355–4358 (IEEE, 2010). doi:10.1109/IEMBS.2010.5626222

132. Martel, S. Microrobotic navigable entities for Magnetic Resonance Targeting. in 1942–1945 (IEEE, 2010). doi:10.1109/IEMBS.2010.5627768

133. Pouponneau, P., Bringout, G. & Martel, S. Therapeutic Magnetic Microcarriers Guided by Magnetic Resonance Navigation for Enhanced Liver Chemoembilization: A Design Review. *Ann. Biomed. Eng.* **42,** 929–939 (2014).

134. Folio, D. & Ferreira, A. Two-Dimensional Robust Magnetic Resonance Navigation of a Ferromagnetic Microrobot Using Pareto Optimality. *IEEE Trans. Robot.* **33,** 583–593 (2017).

135. Riegler, J. *et al.* Magnetic cell delivery for peripheral arterial disease: A theoretical framework: Magnetic cell delivery to lower leg arteries. *Med. Phys.* **38,** 3932–3943 (2011).

136. Martel, S., Mohammadi, M., Felfoul, O., Zhao Lu & Pouponneau, P. Flagellated Magnetotactic Bacteria as Controlled MRI-trackable Propulsion and Steering Systems for Medical Nanorobots Operating in the Human Microvasculature. *Int. J. Robot. Res.* **28,** 571–582 (2009).

137. Martel, S., Felfoul, O. & Mohammadi, M. Flagellated bacterial nanorobots for medical interventions in the human body. in 264–269 (IEEE, 2008). doi:10.1109/BIOROB.2008.4762777

138. Mathieu, J.-B., Beaudoin, G. & Martel, S. Method of Propulsion of a Ferromagnetic Core in the Cardiovascular System Through Magnetic Gradients Generated by an MRI System. *IEEE Trans. Biomed. Eng.* **53,** 292–299 (2006).

139. Schmitt, R. *Electromagnetics Explained a handbook for wireless/RF, EMC and high-speed electronics*. (Elsevier Science & Technology Books).

140. *Magnetic levitation*. (Springer Berlin Heidelberg, 2016).

141. Hurlbut, C. S., Sharp, W. E. & Dana, E. S. *Dana's minerals and how to study them*. (Wiley, 1998).

142. Klabunde, R. E. *Cardiovascular physiology concepts*. (Lippincott Williams & Wilkins/Wolters Kluwer, 2012).

143. Kyrtatos, P. Cell targeting and imaging using magnetic nanoparticles. (University College London, 2009).

144. MRI pulse sequences.

145. Riegler, J. Targeted delivery and MRI tracking of magnetically labelled cells. (University College London, 2011).

146. Hidalgo-Tobon, S. S. Theory of gradient coil design methods for magnetic resonance imaging. *Concepts Magn. Reson. Part A* **36A,** 223–242 (2010).

147. Wong, E. C., Jesmanowicz, A. & Hyde, J. S. Coil optimization for MRI by conjugate gradient descent. *Magn. Reson. Med.* **21,** 39–48 (1991).

148. Crozier, S., Forbes, L. K. & Doddrell, D. M. The Design of Transverse Gradient Coils of Restricted Length by Simulated Annealing. *J. Magn. Reson. A* **107,** 126–128 (1994).

149. Turner, R. A target field approach to optimal coil design. *J. Phys. Appl. Phys.* **19,** L147–L151 (1986).

150. Pan, H. *et al.* Design of small-scale gradient coils in magnetic resonance imaging by using the topology optimization method. *Chin. Phys. B* **27,** 050201 (2018).

151. Tomasi, D. Stream function optimization for gradient coil design. *Magn. Reson. Med.* **45,** 505–512 (2001).

152. Poole, M. & Bowtell, R. Novel gradient coils designed using a boundary element method. *Concepts Magn. Reson. Part B Magn. Reson. Eng.* **31B,** 162–175 (2007).

153. Bigot, A., Tremblay, C., Soulez, G. & Martel, S. Magnetic Resonance Navigation of a Bead Inside a Three-Bifurcation PMMA Phantom Using an Imaging Gradient Coil Insert. *IEEE Trans. Robot.* **30,** 719–727 (2014).

154. McNab, J. A. *et al.* The Human Connectome Project and beyond: Initial applications of 300mT/m gradients. *NeuroImage* **80,** 234–245 (2013).

155. Riegler, J. *et al.* Targeted magnetic delivery and tracking of cells using a magnetic resonance imaging system. *Biomaterials* **31,** 5366–5371 (2010).

156. Pouponneau, P., Leroux, J.-C., Soulez, G., Gaboury, L. & Martel, S. Co-encapsulation of magnetic nanoparticles and doxorubicin into biodegradable

microcarriers for deep tissue targeting by vascular MRI navigation. *Biomaterials* **32,** 3481–3486 (2011).

157. Martel, S. Combining Pulsed and DC Gradients in a Clinical MRI-Based Microrobotic Platform to Guide Therapeutic Magnetic Agents in the Vascular Network. *Int. J. Adv. Robot. Syst.* **10,** 30 (2013).
158. Price, R. R. The AAPM/RSNA Physics Tutorial for Residents: MR Imaging Safety Considerations. *RadioGraphics* **19,** 1641–1651 (1999).
159. Mathieu, J.-B. & Martel, S. Aggregation of magnetic microparticles in the context of targeted therapies actuated by a magnetic resonance imaging system. *J. Appl. Phys.* **106,** 044904 (2009).
160. Bigot, A., Tremblay, C., Soulez, G. & Martel, S. Temperature Response of a Magnetic Resonance Imaging Coil Insert for the Navigation of Theranostic Agents in Complex Vascular Networks. *IEEE Trans. Magn.* **50,** 1–7 (2014).
161. Becker, A. T., Felfoul, O. & Dupont, P. E. Toward tissue penetration by MRI-powered millirobots using a self-assembled Gauss gun. in 1184–1189 (IEEE, 2015). doi:10.1109/ICRA.2015.7139341
162. Park, B.-H., Koo, B. S., Kim, Y. K. & Kim, M. K. The Induction of Hyperthermia in Rabbit Liver by means of Duplex Stainless Steel Thermoseeds. *Korean J. Radiol.* **3,** 98 (2002).
163. Fung, Y.-C. *Biomechanics: Mechanical Properties of Living Tissues*. (1993).
164. Okamura, A. M., Simone, C. & O'Leary, M. D. Force Modeling for Needle Insertion Into Soft Tissue. *IEEE Trans. Biomed. Eng.* **51,** 1707–1716 (2004).
165. Barnes, J. M., Przybyla, L. & Weaver, V. M. Tissue mechanics regulate brain development, homeostasis and disease. *J. Cell Sci.* **130,** 71–82 (2017).

166. Howard, M. A. *et al.* Measurement of the force required to move a neurosurgical probe through in vivo human brain tissue. *IEEE Trans. Biomed. Eng.* **46,** 891–894 (1999).

167. Sharp, A. A., Ortega, A. M., Restrepo, D., Curran-Everett, D. & Gall, K. *In Vivo* Penetration Mechanics and Mechanical Properties of Mouse Brain Tissue at Micrometer Scales. *IEEE Trans. Biomed. Eng.* **56,** 45–53 (2009).

168. Molloy, J. A. *et al.* Experimental determination of the force required for insertion of a thermoseed into deep brain tissues. *Ann. Biomed. Eng.* **18,** 299–313 (1990).

169. Leclerc, J., Ramakrishnan, A., Tsekos, N. & Becker, A. Magnetic Hammer Actuation for Tissue Penetration using a Millirobot. *IEEE Robot. Autom. Lett.* 1–1 (2017). doi:10.1109/LRA.2017.2739805

170. Estelrich, J., Escribano, E., Queralt, J. & Busquets, M. Iron Oxide Nanoparticles for Magnetically-Guided and Magnetically-Responsive Drug Delivery. *Int. J. Mol. Sci.* **16,** 8070–8101 (2015).

171. Derfus, A. M. *et al.* Remotely Triggered Release from Magnetic Nanoparticles. *Adv. Mater.* **19,** 3932–3936 (2007).

172. Thirunavukkarasu, G. K. *et al.* Magnetic field-inducible drug-eluting nanoparticles for image-guided thermo-chemotherapy. *Biomaterials* **180,** 240–252 (2018).

173. Zhang, E. *et al.* Dynamic Magnetic Fields Remote-Control Apoptosis *via* Nanoparticle Rotation. *ACS Nano* **8,** 3192–3201 (2014).

174. Kandasamy, G. & Maity, D. Recent advances in superparamagnetic iron oxide nanoparticles (SPIONs) for in vitro and in vivo cancer nanotheranostics. *Int. J. Pharm.* **496,** 191–218 (2015).

175. Shapiro, B. *et al.* Open challenges in magnetic drug targeting: Open challenges in magnetic drug targeting. *Wiley Interdiscip. Rev. Nanomed. Nanobiotechnol.* **7,** 446–457 (2015).

176. Marie, H. *et al.* Superparamagnetic Liposomes for MRI Monitoring and External Magnetic Field-Induced Selective Targeting of Malignant Brain Tumors. *Adv. Funct. Mater.* **25,** 1258–1269 (2015).

177. Nacev, A. *et al.* Dynamic Inversion Enables External Magnets To Concentrate Ferromagnetic Rods to a Central Target. *Nano Lett.* **15,** 359–364 (2015).

178. Cherry, E. M., Maxim, P. G. & Eaton, J. K. Particle size, magnetic field, and blood velocity effects on particle retention in magnetic drug targeting: Particle retention in magnetic drug targeting. *Med. Phys.* **37,** 175–182 (2009).

179. Chertok, B., David, A. E., Huang, Y. & Yang, V. C. Glioma selectivity of magnetically targeted nanoparticles: A role of abnormal tumor hydrodynamics. *J. Controlled Release* **122,** 315–323 (2007).

180. Nacev, A., Beni, C., Bruno, O. & Shapiro, B. The behaviors of ferromagnetic nano-particles in and around blood vessels under applied magnetic fields. *J. Magn. Magn. Mater.* **323,** 651–668 (2011).

181. Lunnoo, T. & Puangmali, T. Capture Efficiency of Biocompatible Magnetic Nanoparticles in Arterial Flow: A Computer Simulation for Magnetic Drug Targeting. *Nanoscale Res. Lett.* **10,** (2015).

182. Manshadi, M. K. D. *et al.* Magnetic aerosol drug targeting in lung cancer therapy using permanent magnet. *Drug Deliv.* **26,** 120–128 (2019).

183. Ludwig, R. *et al.* Structural properties of magnetic nanoparticles determine their heating behavior - an estimation of the in vivo heating potential. *Nanoscale Res. Lett.* **9,** 602 (2014).

184. Chertok, B., David, A. E. & Yang, V. C. Brain tumor targeting of magnetic nanoparticles for potential drug delivery: Effect of administration route and magnetic field topography. *J. Controlled Release* **155,** 393–399 (2011).

185. Silva, A. C., Kim, S.-G. & Garwood, M. Imaging blood flow in brain tumors using arterial spin labeling. *Magn. Reson. Med.* **44,** 169–173 (2000).

186. d'Esposito, A. *et al.* Computational fluid dynamics with imaging of cleared tissue and of in vivo perfusion predicts drug uptake and treatment responses in tumours. *Nat. Biomed. Eng.* **2,** 773–787 (2018).

187. Lübbe, A. S., Alexiou, C. & Bergemann, C. Clinical Applications of Magnetic Drug Targeting. *J. Surg. Res.* **95,** 200–206 (2001).

188. Jurgons, R. *et al.* Drug loaded magnetic nanoparticles for cancer therapy. *J. Phys. Condens. Matter* **18,** S2893–S2902 (2006).

189. Kempe, H. & Kempe, M. The use of magnetite nanoparticles for implant-assisted magnetic drug targeting in thrombolytic therapy. *Biomaterials* **31,** 9499–9510 (2010).

190. Taylor, E. N. & Webster, T. J. Multifunctional magnetic nanoparticles for orthopedic and biofilm infections. *Int. J. Nanotechnol.* **8,** 21 (2011).

191. Allen, J. C. Complications of Chemotherapy in Patients with Brain and Spinal Cord Tumors. *Pediatr. Neurosurg.* **17,** 218–224 (1991).

192. Schuell, B. *et al.* Side effects during chemotherapy predict tumour response in advanced colorectal cancer. *Br. J. Cancer* **93,** 744–748 (2005).

193. Arruebo, M., Fernández-Pacheco, R., Ibarra, M. R. & Santamaría, J. Magnetic nanoparticles for drug delivery. *Nano Today* **2,** 22–32 (2007).

194. Alexiou, C. *et al.* Delivery of superparamagnetic nanoparticles for local chemotherapy after intraarterial infusion and magnetic drug targeting. *Anticancer Res.* **27,** 2019–2022 (2007).

195. Holligan, D. L., Gillies, G. T. & Dailey, J. P. Magnetic guidance of ferrofluidic nanoparticles in an *in vitro* model of intraocular retinal repair. *Nanotechnology* **14,** 661–666 (2003).

196. Alexiou, C. *et al.* A High Field Gradient Magnet for Magnetic Drug Targeting. *IEEE Trans. Appl. Supercond.* **16,** 1527–1530 (2006).

197. Ally, J., Martin, B., Behrad Khamesee, M., Roa, W. & Amirfazli, A. Magnetic targeting of aerosol particles for cancer therapy. *J. Magn. Magn. Mater.* **293,** 442–449 (2005).

198. Lübbe, A. S. *et al.* Preclinical experiences with magnetic drug targeting: tolerance and efficacy. *Cancer Res.* **56,** 4694–4701 (1996).

199. Skjeltorp, A. T., Dommersnes, P. & Høyer, H. New Forceful Magnetic Bioseparation using GIAMAG Magnet Systems. *MRS Adv.* **2,** 1297–1301 (2017).

200. Udrea, L. E., Strachan, N. J. C., Bădescu, V. & Rotariu, O. An *in vitro* study of magnetic particle targeting in small blood vessels. *Phys. Med. Biol.* **51,** 4869–4881 (2006).

201. Takeda, S., Mishima, F., Fujimoto, S., Izumi, Y. & Nishijima, S. Development of magnetically targeted drug delivery system using superconducting magnet. *J. Magn. Magn. Mater.* **311,** 367–371 (2007).

202. Shakil, S., Hasan, A. & Sarker, S. R. Iron oxide nanoparticles for breast cancer theranostics. *Curr. Drug Metab.* **20,** (2018).

203. Chen, J. *et al.* Reducible polyamidoamine-magnetic iron oxide self-assembled nanoparticles for doxorubicin delivery. *Biomaterials* **35,** 1240–1248 (2014).

204. Ergeneman, O., Dogangil, G., Abbott, J. J., Nazeeruddin, M. K. & Nelson, B. J. A Magnetically Controlled Wireless Intraocular Oxygen Sensor: Concept, Prototype, and In Vitro Experiments. in 4189–4193 (IEEE, 2007). doi:10.1109/IEMBS.2007.4353260

205. Alivisatos, A. P. *et al.* Nanotools for Neuroscience and Brain Activity Mapping. *ACS Nano* **7,** 1850–1866 (2013).

206. Vonthron, M., Lalande, V., Bringout, G., Tremblay, C. & Martel, S. A MRI-based integrated platform for the navigation of microdevices and microrobots. in 1285–1290 (IEEE, 2011). doi:10.1109/IROS.2011.6048274

207. Martel, S. *et al.* Automatic navigation of an untethered device in the artery of a living animal using a conventional clinical magnetic resonance imaging system. *Appl. Phys. Lett.* **90,** 114105 (2007).

208. Mathieu, J.-B. & Martel, S. In vivo validation of a propulsion method for untethered medical microrobots using a clinical magnetic resonance imaging system. in 502–508 (IEEE, 2007). doi:10.1109/IROS.2007.4399160

209. Folio, D. & Ferreira, A. Two-Dimensional Robust Magnetic Resonance Navigation of a Ferromagnetic Microrobot Using Pareto Optimality. *IEEE Trans. Robot.* **33,** 583–593 (2017).

210. Hovet, S. *et al.* MRI-powered biomedical devices. *Minim. Invasive Ther. Allied Technol.* **27,** 191–202 (2018).

211. *Electrical engineer's reference book.* (Newnes, 2003).

212. Felfoul, O., Mathieu, J.-B., Beaudoin, G. & Martel, S. In Vivo MR-Tracking Based on Magnetic Signature Selective Excitation. *IEEE Trans. Med. Imaging* **27,** 28–35 (2008).

213. Llewellin, E. W., Mader, H. M. & Wilson, S. D. R. The rheology of a bubbly liquid. *Proc. R. Soc. Lond. Ser. Math. Phys. Eng. Sci.* **458,** 987–1016 (2002).

214. Aboussouan, E. & Martel, S. High-Precision Absolute Positioning of Medical Instruments in MRI Systems. in 743–746 (IEEE, 2006). doi:10.1109/IEMBS.2006.259265

215. Chung, H.-T., Park, W.-Y., Kim, T. H., Kim, Y. K. & Chun, K. J. Assessment of the accuracy and stability of frameless gamma knife radiosurgery. *J. Appl. Clin. Med. Phys.* **19,** 148–154 (2018).

216. Hinojosa, F. A. & Martel, S. Suggested Shape for a First Generation Endovascular Untethered Microdevice Prototype. in 1286–1288 (IEEE, 2005). doi:10.1109/IEMBS.2005.1616661

217. Liu, T., Lombard Poirot, N., Greigarn, T. & Cenk Çavuşoğlu, M. Design of a Magnetic Resonance Imaging Guided Magnetically Actuated Steerable Catheter. *J. Med. Devices* **11,** (2017).

218. Aksel, B. *et al.* Local planar gradients with order-of-magnitude strength and speed advantage. *Magn. Reson. Med.* **58,** 134–143 (2007).

219. Mayer, D. *et al.* In vivo fiber tracking in the rat brain on a clinical 3T MRI system using a high strength insert gradient coil. *NeuroImage* **35,** 1077–1085 (2007).

220. Vithanage, C. R., Grimson, M. J. & Smith, B. G. THE EFFECT OF TEMPERATURE ON THE RHEOLOGY OF BUTTER, A SPREADABLE BLEND AND SPREADS. *J. Texture Stud.* **40,** 346–369 (2009).

221. Diamante, L. M. & Lan, T. Absolute Viscosities of Vegetable Oils at Different Temperatures and Shear Rate Range of 64.5 to 4835 s $^{-1}$. *J. Food Process.* **2014,** 1–6 (2014).

222. Kim-Tiu, T., Nesaretnam, K. & Kanagaratnam, S. Trans Fats Replacement Solutions in Malaysia. in *Trans Fats Replacement Solutions* 385–398 (Elsevier, 2014). doi:10.1016/B978-0-9830791-5-6.50023-X

223. Borwankar, R. P., Frye, L. A., Blaurock, A. E. & Sasevich, F. J. Rheological Characterization of Melting of Margarines and Tablespreads. in *Rheology of Foods* 55–74 (Elsevier, 1992). doi:10.1016/B978-1-85166-877-9.50009-2

224. Budday, S. *et al.* Mechanical properties of gray and white matter brain tissue by indentation. *J. Mech. Behav. Biomed. Mater.* **46,** 318–330 (2015).

225. Master, V. A., Shinohara, K. & Carroll, P. R. FERROMAGNETIC THERMAL ABLATION OF LOCALLY RECURRENT PROSTATE CANCER: PROSTATE SPECIFIC ANTIGEN RESULTS AND IMMEDIATE/INTERMEDIATE MORBIDITIES. *J. Urol.* **172,** 2197–2202 (2004).

226. Meredith, R. F. *et al.* Ferromagnetic thermoseeds: Suitable for an afterloading interstitial implant. *Int. J. Radiat. Oncol.* **17,** 1341–1346 (1989).

227. Choe, R. *et al.* Optically Measured Microvascular Blood Flow Contrast of Malignant Breast Tumors. *PLoS ONE* **9,** e99683 (2014).

228. Li, J. & Mooney, D. J. Designing hydrogels for controlled drug delivery. *Nat. Rev. Mater.* **1,** (2016).